Further Development and Application of a Mobile Multiple-Reflection Time-of-Flight Mass Spectrometer for Analytical High-Resolution Tandem Mass Spectrometry

Inauguraldissertation zur Erlangung des Doktorgrades der Naturwissenschaftlichen Fakultät der Justus-Liebig-Universität Gießen

vorgelegt von

Wayne Lippert
geboren in Wetzlar

Fachbereich 07 - Mathematik und Informatik, Physik, Geographie

II. Physikalisches Institut Justus-Liebig-Universität Gießen

Gießen, Juli 2016

Contents

Zusammenfassung

Im Rahmen dieser Arbeit wurde ein mobiles Multireflexions-Flugzeitmassenspektrometer (MR-TOF-MS) für analytische Massenspektrometrie in vielen wichtigen Aspekten weiterentwickelt. Es wurden technische als auch software-basierte Verbesserungen vorgenommen, welche die Leistungsfähigkeit und den Anwendungsbereich des Massenspektrometers stark erweitern. Es wurden Änderungen am gesamten Strahlvorbereitungs-System des MR-TOF-MS durchgeführt. Der elektronische Aufbau wurde in diesem Zusammenhang komplett überarbeitet und ein Quadrupol-Massenfilter in Betrieb genommen. Sowohl stoßinduzierte Dissoziation als auch ein neues Zeitablauf-System wurden implementiert, wodurch anspruchsvolle Messungen im Bereich der Tandem-Massenspektrometrie ermöglicht werden. Weiterhin wurden Modifikationen am ionenoptischen System und am Detektor des Analysators durchgeführt, um das Auflösungsvermögen und die Empfindlichkeit des Instruments zu erhöhen.

In Messungen mit verschiedenen Isotopen von Coffein und Hexamethoxyphosphazen wurde eine durchschnittliche Massengenauigkeit von 0,3 ppm erzielt. Mit einer Flugzeit von etwa 6 ms konnte ein Massenauflösungsvermögen von 200.000 erreicht werden. Die Aminosäure Arginin wurde zur Bestimmung des Dynamikbereichs des Instruments verwendet, welcher insgesamt 5 Größenordnungen an Analyt-Konzentration umfasst.

Ferner wurden umfangreiche Untersuchungen zu Raumladungseffekten im Analysator durchgeführt. Entsprechende Simulationen und Messungen stimmen in hervorragender Weise überein. Verschiedene Lösungsansätze, wie das Ändern der Position des intermediären Zeit-Fokus oder das Verwenden höherer Extraktions-Feldstärken, sind sehr vielversprechend und können Raumladungseffekte in zukünftigen Messungen reduzieren.

Es wurde gezeigt, dass sich der massenselektive Wiedereinfang ("Re-Trapping") ideal zur Durchführung hochauflösender Massenmessungen in jeder Stufe der Massenseparation eignet. Auflösungsvermögen und Effizienzen dieser Methode wurden im Detail untersucht und Separationsvermögen von bis zu 70.000 gemessen. Um das MS/MS und MS^n Potential des Instruments zu illustrieren, wurden Messungen mit den Aminosäuren Glutamin und Lysin (Massendifferenz $\Delta m = 36.4$ mu) durchgeführt. Desweiteren wurde eine Rohöl-Probe in einer ersten Machbarkeitsmessung analysiert. In dieser wurde eine spezielle Verbindung von ihren isobaren Kontaminanten isoliert und das dazugehörige Fragmentspektrum aufgezeichnet.

4

Abstract

In this work, a mobile multiple-reflection time-of-flight mass spectrometer (MR-TOF-MS) for analytical mass spectrometry was enhanced in many important aspects. Technical as well as software-based improvements have been added to the instrument, thus greatly increasing its performance and applicability. Changes have been applied to the whole beam preparation system of the MR-TOF-MS. In this context, the electronic setup was completely overhauled and a quadrupole mass filter was commissioned. Collision-induced dissociation and a new trigger system have been implemented, enabling the possibility to perform sophisticated tandem mass measurements. Additional modifications have been done to the ion-optics and detector system of the time-of-flight analyzer to improve the instrument's resolving power and sensitivity.

An average mass accuracy of 0.3 ppm was achieved in measurements with several isotopes of the molecules hexamethoxyphosphazene and caffeine. With a flight time of about 6 ms, mass resolving powers of 200,000 could be obtained. The amino acid arginine was utilized to probe the instrument's linear dynamic range, which was found to cover 5 orders of magnitude in analyte concentration.

Space charge effects in the analyzer were extensively investigated. Corresponding simulations and measurements are in excellent agreement with each other. Several approaches such as the change of the position of intermediate time-focus and the use of high extraction field strengths seem to be very promising solutions and will be able to reduce space charge effects in future measurements.

It was shown that the method of mass-selective re-trapping is ideally suited to perform tandem mass measurements with high-resolution mass separation in every stage of the measurement. Resolving powers as well as efficiencies of re-trapping were studied in detail and separation powers of up to 70,000 have been obtained. Measurements with the two amino acids glutamine and lysine (mass difference $\Delta m = 36.4$ mu) were conducted to illustrate the MS/MS and MS^n capabilities of the instrument. Additionally, a crude oil sample has been analyzed in a first proof-of-principle application. There, a specific compound could be successfully isolated from its isobaric contaminants and the corresponding fragment spectrum has been recorded.

1 Introduction

1.1 Analytical Mass Spectrometry

Since the first groundbreaking mass spectrometric experiments by Goldstein and Wien [Goldstein, 1886, Wien, 1898] at the end of the 19th and by Thomson, Dempster and Aston [Thomson, 1913, Dempster, 1918, F.W. Aston M.A. D.Sc., 1919] at the beginning of the 20th century, mass spectrometry, as the analytical technique of measuring atomic and molecular masses, has made great progress. A vast amount of new mass spectrometric methods and instruments has been developed, rendering experiments for many different fields of application possible.

Today, mass spectrometry is an integral part of sciences like physics, chemistry, biology, medicine and archeology - only to name a few. For instance, mass spectrometry is used to identify and quantify unknown chemical compounds, to provide understanding of the structure of molecules and to determine the age of objects containing organic material (radiocarbon dating). Other examples are the study of proteins (de novo peptide sequencing) [Taylor and Johnson, 1997], and the analysis of organic substances in different biological mixtures [de Leenheer and Thienpont, 1992].

With all these various fields of research and applications, it becomes clear that many different types of mass spectrometers are needed to cope with the specific requirements of each application; requirements such as sensitivity, speed and accuracy. Many mass spectrometers utilize the advantage of combining different types of mass analyzers or are coupled to distinctive analytical techniques like chromatography (gas chromatography MS (GC/MS) and liquid chromatography MS (LC/MS)) to further enhance the sensitivity of an experimental setup, for example. Modern mass spectrometers come in various sizes, use a large amount of different ionization methods and mass analyzing techniques and are applied in laboratories as well as in-situ.

The use of mass spectrometers outside of the laboratory is becoming increasingly important. Portable instruments are applied for gas monitoring, detection of environmental toxins, explosives, and chemical warfare agents, and point-of-care applications [Snyder et al., 2016]. Contemporary devices provide resolving powers from one mass unit [Hendricks et al., 2014] up to 30,000 [Jeol Ltd., 2016] (portable instrument), and may have such low power requirements that they can run on battery [908 Devices, 2016] (handheld device).

1.2 Tandem Mass Spectrometry

One technique that plays a crucial role in the investigation of complex samples is the technique of tandem mass spectrometry. The term "tandem mass spectrometer" refers to an experimental setup where at least two consecutive steps of mass separation with an intermediate step of molecular fragmentation are performed. Tandem mass spectrometry is also known as "MS/MS" if the number of mass separation steps is two, or "MS^n" for $n = 2$ or more steps of mass separation. In the first mass separation step, an ion of interest (i.e. an ion of a certain mass-to-charge ratio) is selected. Then, this so-called precursor ion undergoes a dissociation process and its fragments (also known as product ions) are finally recorded in a mass spectrum. This step-wise mass separation procedure can either be performed in two locally separated mass analyzers (tandem-in-space) or within the same analyzer (tandem-in-time). The fragmentation of precursor ions can be achieved in several ways. One of the most prominent techniques is collision-induced dissociation, which utilizes collisions of ions with a buffer gas to break up the ion of interest (see section 2.3.2 for more information). In fig. 1.1 the MS/MS process is illustrated.
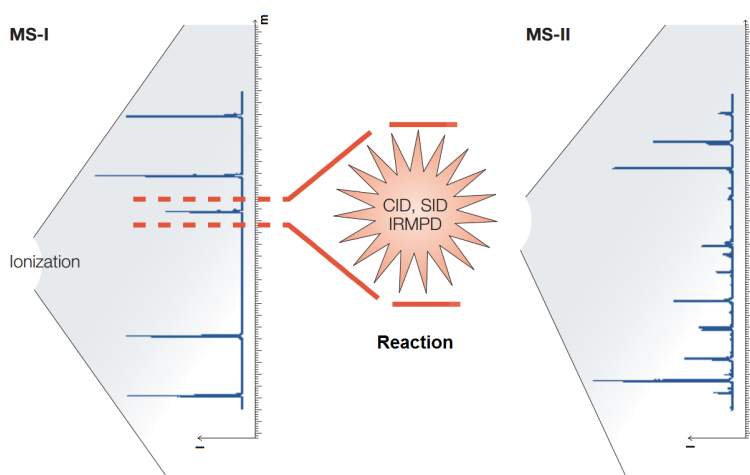
Figure 1.1: Illustration of tandem MS. An ion of interest is selected from the mass spectrum (MS-I) and its product ions are measured (MS-II). The product ions can be generated by various different dissociation processes [Glish and Vachet, 2003].

Tandem mass spectrometry is ideally suited to investigate the structure, bond energies and fragmentation pathways of molecules. Depending on the type of activation technique applied, large molecule will only break up at certain molecular bonds. The inner structure of the precursor molecule is thus revealed by the occurrence of a specific fragmentation pattern in the mass spectrum. Furthermore, product ion spectra can provide additional information about the composition of the precursor ion and may therefore help to unambiguously identify the ions of interest.

In figure 1.2 a comparison of different mass analyzers for MS/MS measurements with respect to key performance attributes is shown [Glish and Burinsky, 2008].

	Resolving power		Mass accuracy		
Analyzer type	MS-1	MS-2	MS-1	MS-2	Measurement time[a] (seconds)
Magnetic (B) sector	Medium	Medium	ppt	ppt	10^{-5}
Electric (E) sector	na[b]	Low	na[b]	ppt	10^{-5}
Electric and magnetic sector[c]	High	Medium	ppm	ppt	10^{-5}
Time-of-flight (TOF)	Low	Medium[d]	ppm	ppm	10^{-5}
Quadrupole mass filter (Q)	Low	Low	ppt	ppt	10^{-4}
Quadrupole ion trap (QIT)	Low	Low	ppt	ppt	10^{-2}
FTICR	High	High	ppm	ppm	10^{-1}
Orbitrap	na[b]	High	na[b]	ppm	10^{-1}

[a]The time, after activation, for the ions to react prior to the second stage of analysis.
[b]na: not applicable; this analyzer has not been used for the first stage of an MS/MS experiment. There is currently no mode of operation in which a parent ion can be mass selected for a subsequent stage of analysis.
[c]When electric and magnetic sectors are used as a double focusing mass spectrometer for one stage of analysis, either prior to (MS-1) the reaction, or subsequent to (MS-2) the reaction.
[d]The resolving power is medium if the TOF ion axis is orthogonal to the first stage of MS; if the axes are coaxial, the resolving power is low.

Figure 1.2: Comparison of different mass analyzers for MS/MS measurements with respect to key performance attributes [Glish and Burinsky, 2008]. In this context: "low", less than 1000; "medium", 1000 to 10,000; "high", greater than 10,000.

Typically, low-resolution analyzers such as quadrupole mass filters (Q) and linear quadrupole ion traps (LTQ) are used for precursor ion selection and combined with analyzers capable of high-resolution product ion measurements (e.g. Q-TOF, LTQ-FTICR or LTQ-Orbitrap devices). Mass spectrometers like the multiple-reflection-based ELIT [Hilger et al., 2013] or Thermo Scientific's triple quadrupole [Thermo Scientific, 2016] offer low- to medium-resolution mass separation in the first stage of the MS/MS measurement. Medium- to high-resolution precursor selection can so far only be achieved in stationary and costly sector [Fenselau, 1992] and FTICR [Guan and Marshall, 1996, Heck and Derrick, 1997] instruments, respectively.

1.3 Mass Spectrometry in Nuclear Physics

Mass spectrometry is also an essential part in the field of nuclear physics, as it allows to probe and verify our understanding of nuclear structure.

The mass $m(A, Z)$ of an atomic nucleus $^A_Z X$ can be written as sum of the masses of its constituents (i.e. the mass of protons m_p and neutrons m_n) and its binding energy $E_B(A, Z)$:

$$m(A, Z) = Z \cdot m_p + (A - Z) \cdot m_n - E_B(A, Z)/c^2 \qquad (1.1)$$

The contribution of the binding energy to the mass $m(A, Z)$ depends of the internal structure of the nucleus and the interaction between its nucleons. Accurate mass measurements in connection with today's mass models do not only provide insights into the structure of the nucleus, but also allow for the deduction of more characteristic properties, like the nucleus' half-life, separation energies and radius. These quantities play an important role in our understanding of the abundance of the chemical elements and the nucleosynthesis process, i.e. the formation of elements in stars.

To cope with the challenging requirements of today's nuclear physics experiments in terms of e.g. short measurement times and low production rates, an increasing number of multiple-reflection time-of-flight mass spectrometers is operated at rare isotope facilities all around the world [Plaß et al., 2013b, Jesch et al., 2015, Schury et al., 2009, Wolf et al., 2011]. MR-TOF-MS provide high-resolution mass measurements on short time scales ($\sim$ ms), and are also used as efficient diagnostics devices due to their sensitivity and broadband measurement capability [Plaß et al., 2015].

1.4 The Mobile MR-TOF-MS for Analytical Tandem MS

Since the large potential of MR-TOF-MS can also be applied outside the field of nuclear physics, a mobile high-performance MR-TOF-MS for analytical mass spectrometry has been developed for the first time [Lang, 2016]. It comprises an atmospheric pressure interface to couple various ionization sources to the instrument, an RFQ beam preparation system to guide the ions to the analyzer and to prepare them for injection, and a multiple-reflection time-of-flight analyzer with a detector. The instrument was designed to achieve mass resolving powers of $R > 100,000$ and mass accuracies below 1 ppm in a mobile format with low infrastructural needs, and thus to combine the performance characteristics of stationary mass spectrometers with the possibility to perform analytical experiments in-situ.

The goal of this work was to substantially extend the capabilities of the mobile MR-TOF-MS and to investigate its performance characteristics in detail. Furthermore, the option to operate the device as a multi-stage tandem mass spectrometer (MS^n, [Plaß et al., 2013a]) with high-resolution in every stage was implemented with the technique of mass-selective ion re-trapping, which is ideally suited for ion precursor selection. For ion dissociation, the method of resonance excitation was realized in the RF ion trap and tandem mass spectrometry experiments with analytical samples have been conducted with the MR-TOF-MS for the first time.

2 Basic Principles

2.1 Terms and Concepts

This section deals with the explanation and definition of frequently occurring basic terms of mass spectrometry used in this work. In general and if not stated otherwise, the IUPAC recommendations of 2013 are followed [Murray et al., 2013].

Mass

The mass of a body is an inherent property. Its SI unit is the kilogram, which is defined as follows: "The kilogram is the unit of mass; it is equal to the mass of the international prototype of the kilogram." [de la Convention du Mètre, 2014]. The kilogram is the only SI unit which is (still) defined by reference and today's scientific community strives to provide a definition based on physical constants instead in the near future [Davis, 2003].

At microscopic scales masses are usually specified in units of the atomic mass unit u, which is "equal to 1/12 times the mass of a free carbon 12 atom, at rest and in its ground state"; i.e. $1\ \mathrm{u} = 1.66053886(28) \cdot 10^{-27}$ kg [de la Convention du Mètre, 2014].

Labeling of Mass Spectra

As customary in analytical mass spectrometry, the abscissae of mass spectra in this work are labeled with "m/z", an "abbreviation representing the dimensionless quantity formed by dividing the ratio of the mass of an *ion* to the *unified atomic mass unit*, by its *charge number* (regardless of sign)" [Murray et al., 2013].

The abbreviation "m/z" is not to be confused with the variables m and z. The variable m is used for the ion's mass (in kg), whereas z is referred to as the coordinate of the optical axis (i.e. z-coordinate) otherwise.

Mass Range

The range of masses that can be simultaneously measured by a mass spectrometer is called mass range. It is normally specified by the interval $[m_{min}, m_{max}]$ or by the ratio m_{max}/m_{min} of the largest (m_{max}) to the smallest (m_{min}) measurable mass. Latter definition will be utilized to describe the mass range of the MR-TOF-MS.

Mass Resolving Power

Mass resolving power expresses the ability of a mass spectrometer to resolve two ion species of mass m that are only separated by a small mass difference $\Delta m = m_2 - m_1$, and can be calculated by:

$$R = \frac{m}{\Delta m} \qquad (2.1)$$

In this context, Δm is typically defined as "the separation between two adjacent equal magnitude peaks such that the valley between them is a specified fraction of the peak height" [Murray et al., 2013]. Practically, the mass resolving power R can often be determined with a single peak. In this case, m is the mass and Δm the full width at half maximum (FWHM) of the peak in the mass spectrum.

Mass Accuracy

Mass accuracy can be defined as the relative difference between the experimentally determined mass value m_{exp} and the calculated exact mass m_{theo} [Brenton and Godfrey, 2010]:

$$\frac{\delta m}{m} = \frac{m_{exp} - m_{theo}}{m_{theo}} \qquad (2.2)$$

It is usually expressed in parts per million (ppm).

Linear Dynamic Range

The range of e.g. analyte concentration over which the instrument's response signal is proportional to the input signal is called linear dynamic range. Its limits can be caused by chemical and/or electrical noise, by saturation effects of the detector or space charge, for example.

Detection Limit

The limit of detection indicates the smallest amount of an analyte in solution relative to the amount of material analyzed that can be detected to a reasonable extent. Since there exist several dissenting definitions of what "detectable" means in this context (e.g. a certain signal-to-noise ratio), it is indispensable to specify the criterion that is applied when quantifying the detection limit of an instrument.

2.2 Electrospray Ionization

Electrospray ionization (ESI) is an atmospheric ionization method that uses strong electric fields to vaporize and ionize liquid samples. It is known to be a soft ionization method, i.e. it usually keeps even large ionized molecules intact [Dole et al., 1968, Fenn et al., 1989].

The liquid sample is pumped by a syringe into the ESI capillary and a high voltage of a few kV is applied between the capillary and the inlet of the mass spectrometer. This leads to the formation of the so-called Taylor cone [Taylor, 1964]. Due to the electric field, small droplets of the sample solution leave the Taylor cone and the solvent starts to evaporate gradually from the droplets [Bruins, 1998]. Highly charged droplets form and analyte ions are ejected into the surrounding gas (see 2.1) after reaching the Rayleigh limit, which describes the maximum amount of charge the droplets can carry [Lord Rayleigh F.R.S., 1882]. The emitted ions are of the same polarity as the ESI capillary and are usually separated from neutrals by a skimmer, before they are guided into the mass spectrometer by electric fields for subsequent analysis. Since ESI also allows for the formation of multiply charged ions, mass measurements of large molecules of up to 10^8 u are rendered possible [Chen et al., 1995].
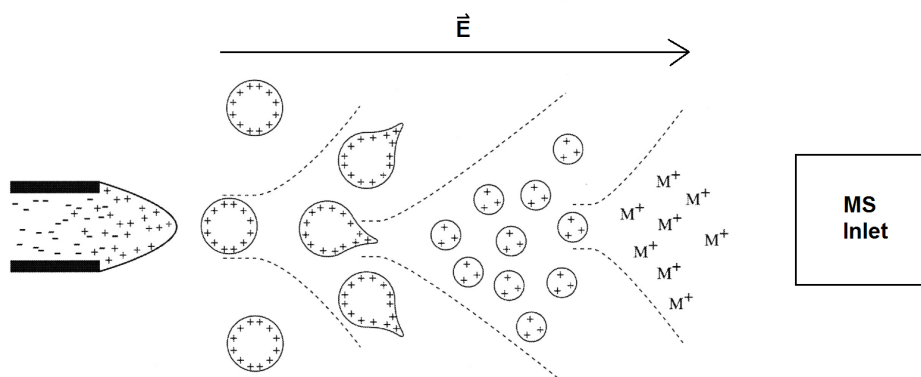

Figure 2.1: A schematic figure of the ESI process from droplet dispersal to analyte emission [Ho et al., 2003].

2.2.1 Nanoelectrospray Ionization

Nanoelectrospray ionization (nano-ESI) is a form of electrospray and was first introduced by Wilm and Mann [Wilm and Mann, 1994]. The term nanoelectrospray refers to the sample flow rate of this ionization technique, which is in the nl/min regime, in contrast to the typical flow rate of up to several tens of μl/min for ESI [Banerjee and Mazumdar, 2012]. For nano-ESI a glass or quartz emitter covered with an electrically conductive layer is used, containing a sample volume of a few microliters only. Nanoelectrospray ionization does not rely on the use of a mechanical syringe pump, as a combination of electric and capillary forces is able to establish a steady sample flow on its own. Furthermore, nano-ESI affects the ion formation itself positively, leading to an enhancement of sensitivity and enlarges the area of possible ESI-MS applications [Karas et al., 2000].

2.3 Radio Frequency Quadrupoles

Radio frequency quadrupoles (RFQs) are used for the purpose of transporting, storing and manipulating ions [Paul and Steinwedel, 1956]. They ideally consist of four hyperbolic rods in parallel arrangement. RFQs are able to store ions in the x-y-plane perpendicular to their orientation. This confinement is achieved by using radio frequency fields with opposite sign on neighboring electrodes, which generate an effective potential minimum on the beam axis for a specific range of mass-to-charge ratios [Major and Dehmelt, 1968].

2.3.1 Ion Motion in RFQs

The ion motion in a radio frequency quadrupole field can be described by Mathieu's differential equations [Mathieu, 1868]. If the time-dependent electric potential on the electrodes is of the form

$$\Phi(t) = \pm(U + V\cos(\Omega t)) \tag{2.3}$$

where U is a direct, V an alternating voltage and Ω the corresponding angular frequency, Newton's equation of motion reads:

$$\frac{d^2u}{d\xi^2} + (a_u - 2q_u\cos(2\xi))\,u = 0 \qquad u \in \{x, y\} \tag{2.4}$$

The dimensionless parameter ξ is defined as:

$$\xi = \frac{\Omega t}{2} \tag{2.5}$$

The parameters a_u and q_u are the so-called Mathieu parameters. Their definition with respect to the ion's mass m and the ion's charge Q is:

$$a_x = -a_y = \frac{8QU}{m\Omega^2 r_0^2} \tag{2.6}$$

$$q_x = -q_y = \frac{4QV}{m\Omega^2 r_0^2} \tag{2.7}$$

In this context the parameter r_0 describes the distance from the electrodes' surface to the beam axis. Stable solutions to the Mathieu equation (2.4) can be written as a superposition of periodical functions with low and high angular frequencies [March and Todd, 2005]:

$$u(\xi) = A \sum_{n=-\infty}^{\infty} C_{2n} \cos((2n + \beta_u)\xi) + B \sum_{n=-\infty}^{\infty} C_{2n} \sin((2n + \beta_u)\xi) \qquad u \in \{x, y\} \tag{2.8}$$

Here, A and B comprise constants of integration which depend upon the initial conditions, and C_{2n} are coefficients depending on a_u and q_u. In the simplified case that β_u, which can be approximated by

$$\beta_u \approx \sqrt{a_u + \frac{1}{2}q_u^2} \qquad u \in \{x, y\} \tag{2.9}$$

if $q_u < 0.4$ (Dehmelt approximation), is sufficiently small, the ion's motion in a quadrupole field can be treated like a harmonic oscillation of angular frequency ω_u in a parabolic potential well $V_{pseudo}(u)$ [Major and Dehmelt, 1968, March and Todd, 2005]:

$$V_{pseudo}(u) = \frac{Vq_u}{4} \frac{u^2}{u_0^2} \qquad u \in \{x, y\} \tag{2.10}$$

The frequency of this macromotion can be calculated as follows:

$$\omega_u = \left(\frac{\beta_u}{2}\Omega\right) \qquad u \in \{x, y\} \tag{2.11}$$

In general, stable ion motion is only achieved for certain pairs (a_u, q_u) of the Mathieu parameters. These sets of solutions are represented by areas in the parameter space (stability diagram) and are called regions of stability.

If an RFQ is operated at the apex of the stability region, only a small band of mass-to-charge ratios will be transmitted. RFQs operated in this mode are referred to as quadrupole mass filters. They are typically enclosed by two Brubaker lenses [Brubaker, 1968] to improve ion transmission into and out of the mass filter quadrupole.

Furthermore, RFQs can be used for collisional cooling. The temperature of ions with several eV of kinetic energy can be reduced by collisions with neutral gas atoms or molecules of lower temperature. This is for example utilized in the RF cooler and RF ion trap of the MR-TOF-MS, where collisional cooling with a buffer gas leads to reduction of the ions' phase space. A compact phase space decreases the negative impact of aberrations on the peak width in the time-of-flight spectrum and thus improves the mass resolution of the mass spectrometer.

2.3.2 Collision-Induced Dissociation

To perform tandem mass spectrometry (see section 1.2), an intermediate step of molecule dissociation between precursor isolation and product ion measurement is required. Several well-established, diverse methods of molecule fragmentation exist, like surface induced dissociation [Wysocki et al., 2008] or electron-capture/electron-transfer dissociation [Zhurov et al., 2013], for example. This section will solely focus on (trapping) collision-induced dissociation (CID), which can be performed inside an RF ion trap.

Trapping CID utilizes an auxiliary electric field to excite the ion's macromotion inside of the RFQ's pseudo-potential. The gain of additional energy associated with this motion is then transferred into the ion's internal degrees of freedom via collisions with a neutral buffer gas like He or N_2. The center-of-mass energy E_{cm} available for conversion into internal energy in a collision between the ion and a neutral gas atom/molecule reads (assuming the neutral is at rest):

$$E_{cm} = E_{lab} \left(\frac{m_n}{m_n + m} \right) \tag{2.12}$$

E_{lab} is the energy of the ion with mass m in the laboratory frame, m_n represents the mass of the neutral. During the process of resonant excitation, the ion will undergo tens to hundreds of collisions and gain internal energy, which is usually distributed over the whole molecule in the form of vibrational energy (ion activation) [Wells and McLuckey, 2005]. After a time span of a few milliseconds, the

molecule will have built up enough energy to undergo fragmentation (unimolecular dissociation). Those fragments that still meet the requirements of performing a stable motion in the ion trap will be trapped and cooled again. Due to the time scale of the dissociation process, very high dissociation efficiencies of up to 100% can be reached [Wells and McLuckey, 2005].

2.4 Multiple-Reflection Time-of-Flight Mass Spectrometry

2.4.1 Principles of TOF-MS

The technique of time-of-flight mass spectrometry is based on the non-relativistic relation between the mass m of an ion with the electric charge Q and the time t it needs to travel a certain flight path Z in the electric potential $U(z)$ of a mass analyzer:

$$QU(z) = \frac{1}{2}mv(z)^2 \quad \Rightarrow \quad t = \int_Z \frac{dz}{\sqrt{\frac{2Q}{m}U(z)}} \quad \Rightarrow \quad \frac{m}{Q} = at^2 \qquad (2.13)$$

After determining the calibration factor a with a time-of-flight measurement of one or more references masses m of known m/Q, one can calculate the unknown mass value of an ion by measuring its time-of-flight within the same experimental setup. The flight time is defined as the difference between the time of pulsed ion injection into the mass analyzer and the time at which the ions impinge on the ion detector.
Consequently, with equation (2.13) the mass resolving power R of a time-of-flight mass spectrometer can be calculated by

$$\frac{dm}{dt} = 2t \quad \Rightarrow \quad R = \frac{m}{\Delta m} = \frac{t}{2\Delta t},\qquad (2.14)$$

with Δt being the width of the peak in the time-of-flight spectrum (see section 2.1). In a simplified manner Δt can be written as square root of the quadratic sum of two independent terms, namely the initial time spread Δt_i of the ion cloud and the time spread Δt_{io} caused by ion-optical aberrations:

$$\Delta t = \sqrt{\Delta t_i^2 + \Delta t_{io}^2}\qquad (2.15)$$

When ions are injected into the analyzer, a pulsed electric field E is applied. The ions' isotropic distribution of thermal velocities v is causing a fraction of the ions

to fly in the direction opposite to the direction of ion extraction. The time these ions need to reverse their direction of flight is called turn-around time Δt_{ta}:

$$\Delta t_{ta} = \frac{2mv}{QE} \tag{2.16}$$

By expressing the velocity in terms of ion temperature, the FWHM of the time spread $\Delta t_{ta,FWHM}$ generated by this effect can be calculated [Plaß, 1997]:

$$\Delta t_{ta,FWHM} = \sqrt{\frac{8\ln(2)mk_BT}{QE}} \tag{2.17}$$

This time spread $\Delta t_{ta,FWHM}$ accounts for the largest part of the initial time spread Δt_i. However, other effects may also contribute.

Ion-optical aberrations originate from deviations of ion-optical parameters such as energy, position, angle etc. from the parameters of an ion propagating through the time-of-flight analyzer on a reference path. Every deviation in one of these parameters results in a difference in time-of-flight, thus leading to a time spread Δt_{io} on the detector and to a decrease of the mass resolving power. Hence, for the design of a time-of-flight analyzer it is very important to keep the influence of these parameters on the time-of-flight as low as possible. The position of detector is chosen in the same manner, i.e. such that ions with the same mass-to-charge ratio impinge on it at the same time, regardless of their initial phase-space. This position is called position of time-focus.

2.4.2 Multiple-Reflection Time-of-Flight Analyzer

Since the introduction of the first concept of "A Pulsed Mass Spectrometer with Time Dispersion" in 1946 [Stephens, 1946] and the first operation of such an instrument in 1948 [Cameron and D. F. Eggers, 1948], a lot of technical progress in the field of time-of-flight mass spectrometry has been made, such that the separation of isobars or even nuclear isomers became possible [Dickel et al., 2015].

One important factor for the vast increase of the dispersive power of TOF mass spectrometers is the extension of the particles' time-of-flight by "folding" their flight path. This is done by trapping the ions between electrostatic mirrors in so-called multiple-reflection or multiple-turn instruments. A schematic overview of different types of analyzers for time-of-flight mass spectrometers can be found in figure 2.2. At the top, the operating principles of linear and reflector time-of-flight analyzers are shown. The middle and bottom part comprise different kinds of multiple-reflection and multiple-turn analyzers in closed and open path design.
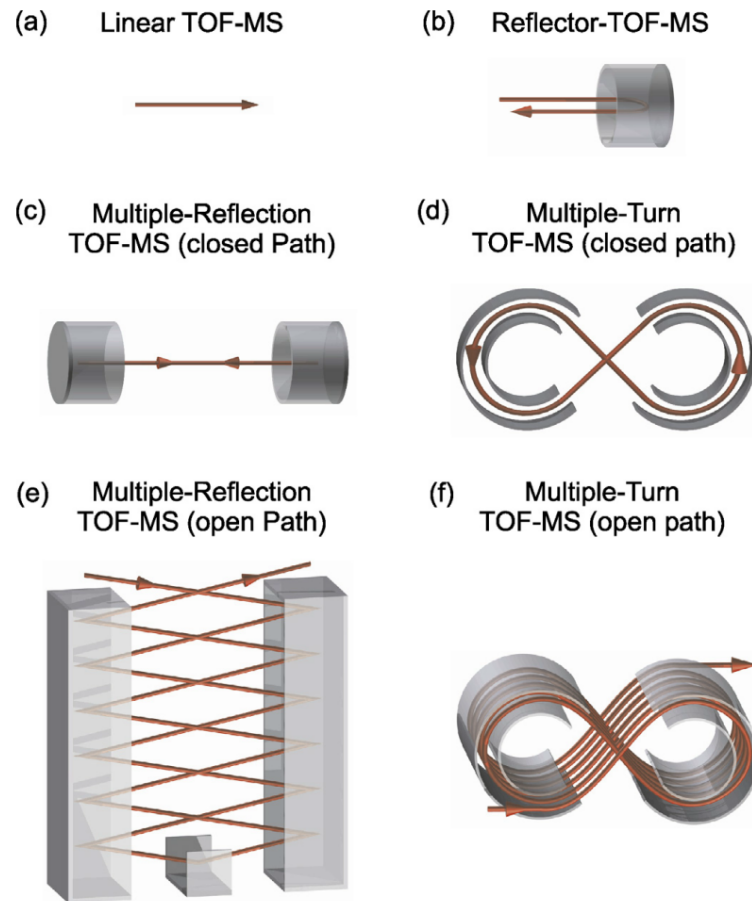
Figure 2.2: Schematic view of different types of analyzers for time-of-flight mass spectrometers [Plaß et al., 2013b]. The analyzer of the MR-TOF-MS uses the concept of closed path ion trajectories (compare with (c)).

Multiple-reflection time-of-flight mass spectrometers allow the ions to traverse the analyzer several thousand times, up to a flight path of a few kilometers, which corresponds to a flight time of several tens of milliseconds. As one can easily see, with time spreads in the sub 100 ns regime, mass resolving powers of a few hundred thousand become possible [Dickel, 2010, Wolf et al., 2012]. Thereby, in modern MR-TOF mass spectrometers masses can be measured with sub-ppm accuracy.

2.4.3 Ion Optical Description

For the ion optical description of ion trajectories in electrostatic fields, so-called aberration expansions can be used [Wollnik, 1987, Yavor, 2009]. Assume a particle with mass m^{ref}, charge Q^{ref} and kinetic energy $K(z)^{ref}$ is moving on a reference path z (i.e. the optic axis of the system) through an electrostatic field. If one defines a plane perpendicular to the direction of movement at each coordinate point z (with its origin coinciding with the optic axis, see fig. 2.3), the trajectory

of an arbitrary ion can be completely described by the position vector $\mathbf{X}(z) = (x(z), a(z), y(z), b(z), T(z), \delta(z), \gamma)$, where:

x, y = x- and y-coordinate in the plane

a, b = angular coordinates; $a = \frac{dx}{dz}$, $b = \frac{dy}{dz}$

T = time-of-flight difference between considered particle
and reference particle; $T = t - t^{ref}$

δ = relative deviation of energy-to-charge ratio of considered particle
and reference particle; $\delta = \frac{K/Q - K^{ref}/Q^{ref}}{K^{ref}/Q^{ref}}$

γ = relative deviation of mass-to-charge ratio of considered particle
and reference particle; $\gamma = \frac{m/Q - m^{ref}/Q^{ref}}{m^{ref}/Q^{ref}}$

If the deviations from the optic axis are small at a particular initial position $\mathbf{X}(z_0)$, one can express the coordinates of the position vector at a certain position z along the reference path by power series. These series are called aberration expansions. For the coordinate x, the series reads

$$x(z) = (x|x)x_0 + (x|a)a_0 + (x|y)y_0 + (x|b)b_0 +$$
$$(x|T)T_0 + (x|\delta)\delta_0 + (x|\gamma)\gamma_0 + (x|xx)x_0^2 + ...$$

$$(2.18)$$

The coefficients of the first-order terms are called paraxial (linear) coefficients, the higher-order terms are called aberration coefficients.
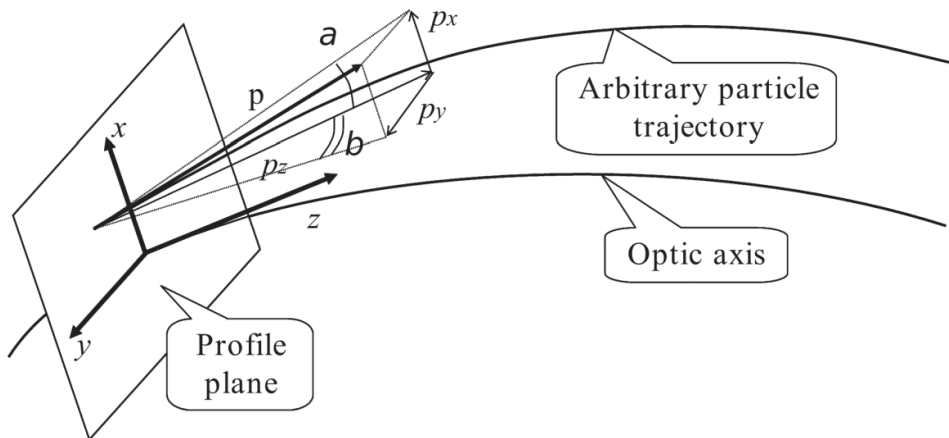

Figure 2.3: Coordinate system as defined relative to the optic axis [Yavor, 2009].

2.4.4 Mass Range

The mass range of a closed path MR-TOF-MS is limited. For the instrument treated in this work, the reflector electrodes are switched between various sets of voltages, for instance during ion injection into and ion ejection out of the analyzer. Ions affected by this change of electric fields experience a distortion in flight time and therefore do not produce any meaningful signals in the time-of-flight spectrum. In addition, it is required that the ions of interest undergo the same total number of turns N (one turn $\hat{=}$ two reflections) in the analyzer to generate an unambiguous time-of-flight spectrum. Although it is in general possible to calibrate a spectrum consisting of ion signals with different turn numbers [Ebert, 2016], this is not an easy task, especially in case of complex sample compositions. The maximum unambiguous mass-to-charge range for this instrument can be calculated as stated in [Yavor et al., 2015]:

$$\frac{(m/Q)_{max}}{(m/Q)_{min}} = \left(\frac{N + \lambda_{inj}}{N + \lambda_{inj} - (1 - \lambda_{mir})} \right)^2 \tag{2.19}$$

where:

$$\lambda_{inj} = \frac{t_{inj}}{t_a} \quad \wedge \quad \lambda_{mir} = \frac{t_{mir}}{t_a} \tag{2.20}$$

As can be seen in fig. 2.4, t_{inj} is the ions' time-of-flight from the ion trap to the region that is affected by switching the mirror potentials, whereas t_{mir} is the time the ions spent in this mirror region. λ_{inj} and λ_{mir} are defined by the ratio of these values to the time-of-flight t_a that is needed to complete a single turn. In general, λ_{mir} is to be kept as small as possible to provide a large unambiguous mass range.
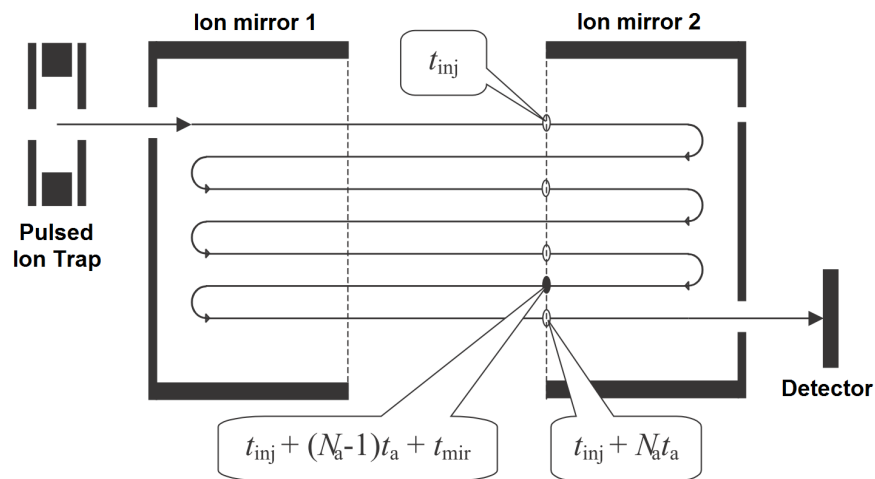

Figure 2.4: Illustration of the different parameters introduced above. The ions' flight path from the ion trap to the detector as well as the mirror electrodes are shown [Yavor et al., 2015].

2.4.5 Time-Focus Shifting

The voltages applied to the analyzer electrodes of MR-TOF mass spectrometers are chosen such that the ions perform a stable motion in the analyzer for a large number of turns. Additionally, the ions' time-focus has to be placed on the detector, which can be done by gradually shifting the focus position by a small amount with every turn. This leads to the consequence that every set of voltages is only valid for a narrow range of turn numbers. Therefore, for a different number of turns, a retuning of the analyzer voltages is required. Nevertheless, this scheme is applied to some of today's closed-path MR-TOF instruments [Wolf et al., 2012, Schury et al., 2014].

To avoid time-consuming and error-prone retuning of voltages every time a different number of turns is chosen, the position of time-focus can be made independent of the ions' turn number by using an additional ion mirror (reflector). If the time-of-flight analyzer is tuned in a way that the intermediate time-foci always occur on the same position regardless of turn number, an additional reflector placed at the entrance or the exit of the analyzer will be able to shift these intermediate time-foci to the detector plane [Plaß et al., 2008, Dickel, 2010].
Another approach is to directly place the time-focus on the detector by utilizing very low extraction voltages for the ion trap. But since low extraction field strengths lead to high turn-around times and therefore to a large initial time spread, the use of a reflector is more favorable.

Alternatively, and instead of using an additional ion mirror, one can also use an extra set of voltages to accomplish the task of shifting the intermediate time-foci to the detector plane. This principle is realized in the MR-TOF-MS of this work and is called "time-focus-shifting" (TFS) [Dickel et al., 2016, Lang, 2016].
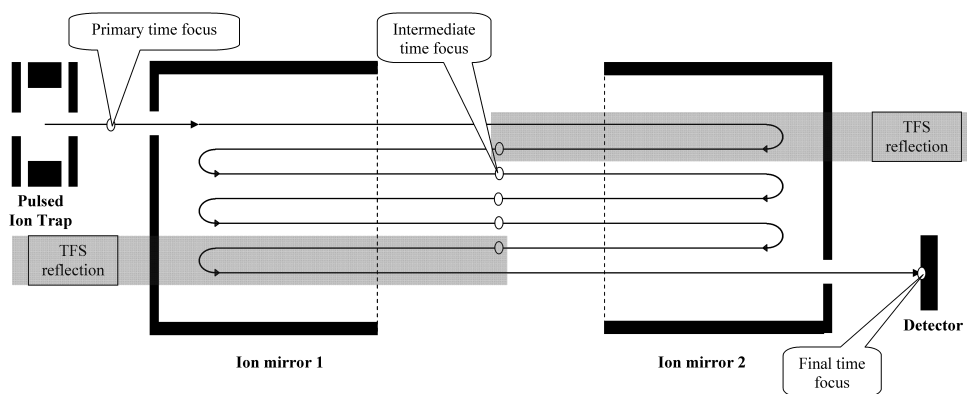

Figure 2.5: Illustration of time-focus shifting in the analyzer. The primary time-focus is shifted to the middle of the analyzer by one reflection in TFS mode. After a certain number of turns in NT mode, the position of time-focus is then transferred onto the detector by another reflection in TFS mode [Yavor, 2014b].

After one turn in TFS mode, the analyzer voltages are switched to the "normal turn" (NT) mode. Thus, the position of time-focus is transferred to the detector after the first turn already and not changed during the number of turns subsequently performed in NT mode. In principle, it does not matter for the position of the final time-focus at which turn number the TFS turn is applied. The two TFS reflections can be even split up, as depicted in figure 2.5. The impact of the order of TFS and NT mode is discussed in more detail in section 6.3, where space charge effects in the analyzer are investigated. In experiments, the optimal analyzer voltage settings are obtained by first tuning the voltages for one turn (i.e. the TFS turn); the NT mode voltages are then tuned for a high number of turns with fixed TFS settings. This allows for high-resolution measurements with varying number of turns in NT mode without the need to re-adjust any of the analyzer voltages.

2.4.6 Mass-Selective Ion Re-Trapping

Mass-selective "ion re-trapping" is a novel technique for the separation of charged particles [Dickel, 2010, Jesch et al., 2015, Plaß et al., 2015]. Instead of impinging on the detector after a number of turns, the ions are guided back to the extraction region and are finally recaptured in the RF ion trap they were originally extracted from. This is done by converting the ions' time dispersion into an energy dispersion. When re-entering the ion trap region, the ions are exposed to a strong retarding field E_r (e.g. the same electric field that was used during ion extraction from the trap into the analyzer). There, the ions will have a remaining kinetic energy K according to their position in this field, which is depending on their respective time-of-flight. By switching the ion trap's voltages back to a storing potential again, only those ions with an energy less than the energy of the electric re-trapping potential QU_r will be re-trapped. In fig. 2.6 this process is illustrated along the beam-axis z.
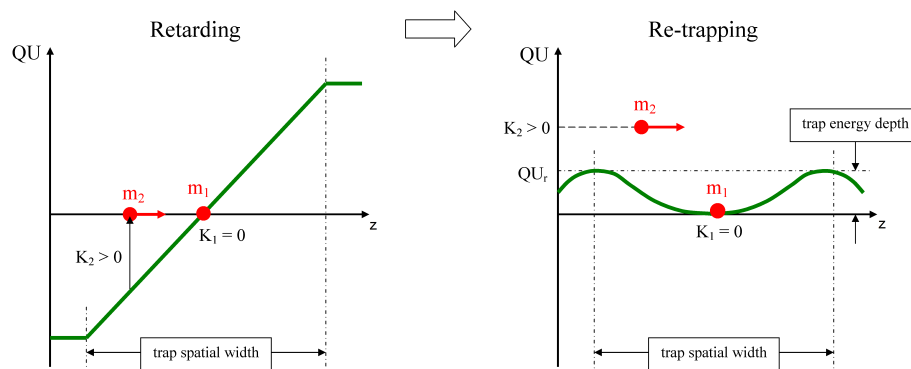

Figure 2.6: Left panel: depending on their position in the RF ion trap's electric field, the ions will have a remaining kinetic energy K at the moment the electric potential is switched. Right panel: the re-trapping potential will only be able to recapture those ions with an energy $K < QU_r$ and reject those with higher energies [Yavor, 2014a].

The mass resolving power (which will be called separation power in this context) of re-trapping can be expressed by the following expression [Yavor, 2014a]:

$$R = \frac{m}{\Delta m} = \frac{t}{2\Delta t + \frac{2}{E_r}\sqrt{\frac{2mU_r}{Q}}} \tag{2.21}$$

Here, U_r is the re-trapping potential and E_r the retarding electric field, respectively. In case of $U_r \to 0$, the separation power coincides with the analyzer's mass resolving power.

First proof-of-principle re-trapping measurements have been successfully performed [Lang, 2016]. There, separation corresponding to a mass resolving power of up to 60,000 (FWHM) could be achieved. Ion re-trapping is a highly mass-selective process and ideally suited to suppress isobaric contamination in nuclear physics experiments [Jesch et al., 2015, Jesch, 2016]. It is also an important pre-requisite for tandem-in-time experiments with unmatched high-resolution precursor selection, which was for the first time implemented and used in the present work (see chapter 7).

2.4.7 Mass Calibration

The mass calibration for time-of-flight spectra of the MR-TOF-MS is based on a modified version of equation (2.13), which reads as follows [Ebert, 2016]:

$$m(t) = a\frac{(t - t_0)^2}{(1 + N_a b)^2} \tag{2.22}$$

Here, m and t are the ion's mass and time-of-flight, N_a the number of turns in normal mode, and a, t_0 and b calibration parameters. With this calibration formula a so-called time-resolved calibration (TRC) can be performed [Bergmann, 2015]. The constants a and t_0 are first determined with at least two calibrants in a calibration of a time-of-flight spectrum recorded in a 1 TFS only measurement ($N_a = 0$). The calibration factor b is then utilized to correct for time-dependent drifts of a calibrant in a spectrum recorded after a certain number of turns in NT mode. For this, the measurement is divided into several consecutive time intervals and b is calculated separately for each of them, while a and t_0 are fixed. As a consequence, the position of the calibrant's mass remains unchanged throughout all intervals and drifts caused by thermal expansion of mechanical components, and instabilities of electrical power supplies are compensated.

2.5 Ion Detectors

Ion detectors used in the field of time-of-flight mass spectrometry should have a fast time-response with excellent resolution and high single ion detection efficiency. During commissioning and operation of the MR-TOF-MS, a microchannel plate detector as well as a MagnetTOF electron multiplier were used. Their modes of operation will be briefly explained below.

2.5.1 Microchannel Plate Detector

Microchannel plate (MCP) detectors consist of millions of thin tubes in parallel arrangement (see [Wiza, 1979, Hamamatsu Photonics K.K., 2013], for example). Those tubes have a diameter of a few micrometers each and are made of highly resistive material, such as lead glass for example. The MCP itself is a few tenth of a millimeter in thickness and often covered with a conductive layer of a nickel alloy. If a high voltage difference of about one kV is applied between both surfaces of the MCP, each of the microchannels will serve as an electron multiplier and amplify the signal of an incident electromagnetically interacting particle (compare with fig. 2.7). Thereby, a signal amplification of up to 10^4 can be reached for a single MCP and the signal becomes detectable.

To increase the order of magnitude of the amplification further, one can stack two or three MCPs on top each other. These arrangements are called chevron (v-like) configuration in case of two MCPs or z configuration in case of three MCPs. These names refer to the mutual $180°$ orientation of the plates, since their microchannels are typically inclined with a small angle to the MCP's surface, generating a v or z shape when stacked.
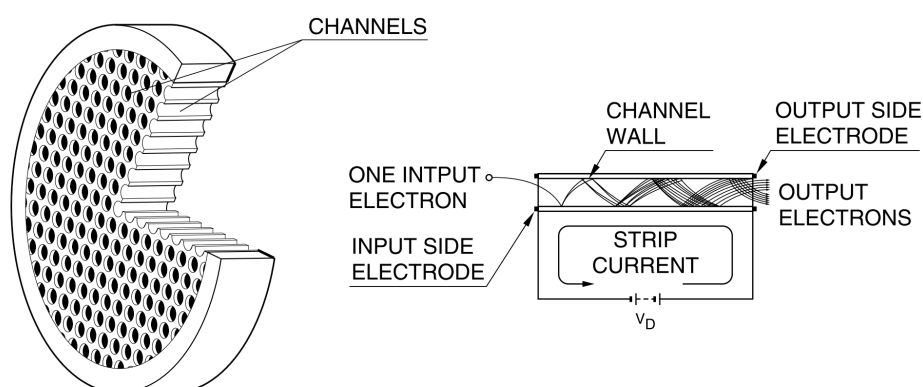

Figure 2.7: Schematic figure of an MCP. The general layout of the MCP as well as the cross section of a single channel is illustrated [Hamamatsu Photonics K.K., 2013].

2.5.2 MagneTOF Electron Multiplier

The MagneTOF electron multiplier is based on the idea of isochronous inter-dynode transfer of electrons through the detector unit [Stresau et al., 2006]. In addition to the electric field, a magnetic field is utilized to generate a time-of-flight focus of the electron cascade (that is created by the incident particles) on the ion impact dynode, thereby creating sharp ions signals with widths of less than one nanosecond. Furthermore, the MagneTOF has a linear response for ion bursts of up to 300,000 ions and a low mass detection efficiency of 80%. The detector is typically operated with a voltage between -2500 V and -4000 V.

3 Experimental Setup

In this chapter, the design aspects of the mobile MR-TOF-MS and its instrumental setup are discussed.

3.1 Conceptual Design

The overall ion-optical design of the MR-TOF-MS can be divided into three parts. It consists of an atmospheric pressure interface (API) to couple various ionization sources to the instrument, a beam preparation system to guide the ions to the mass analyzer and prepare them for injection, and the mass analyzer together with a detector for mass separation and detection. This general layout is illustrated in figure 3.1. Each of the three sub-systems will be discussed in more detail in the following sections.

The instrument was designed to be robust as well as compact and to enable the possibility of transport to investigation sites (and thus to perform mass measurements in-situ) [Lang, 2016]. The ion-optical components of the MR-TOF-MS are placed into three standard vacuum crosses with an additional atmospheric pressure interface of small size on top of it. The whole setup including all support electronics and vacuum pumps has a volume of 0.8 m^3 only (see fig. 3.5).

To achieve high mass resolving powers of $R > 100,000$ in such a compact arrangement, the mass analyzer was designed to be of multiple-reflection type. Several stages of differential pumping in combination with co-axially aligned radio-frequency quadrupoles provide ion transport and the desired high vacuum pressure in the analyzer.

Capillary

Lens

Skimmer

RFQ Ion Guide

RFQ Mass Filter

RFQ Cooler

RF Pre-Trap

RF Ion Trap

Injection Lens

Mass Range Selector

Atmospheric Pressure Interface (API)
[1 bar … 10^{-2} mbar]

Beam Preparation System
[10^{-2} mbar … 10^{-4} mbar]
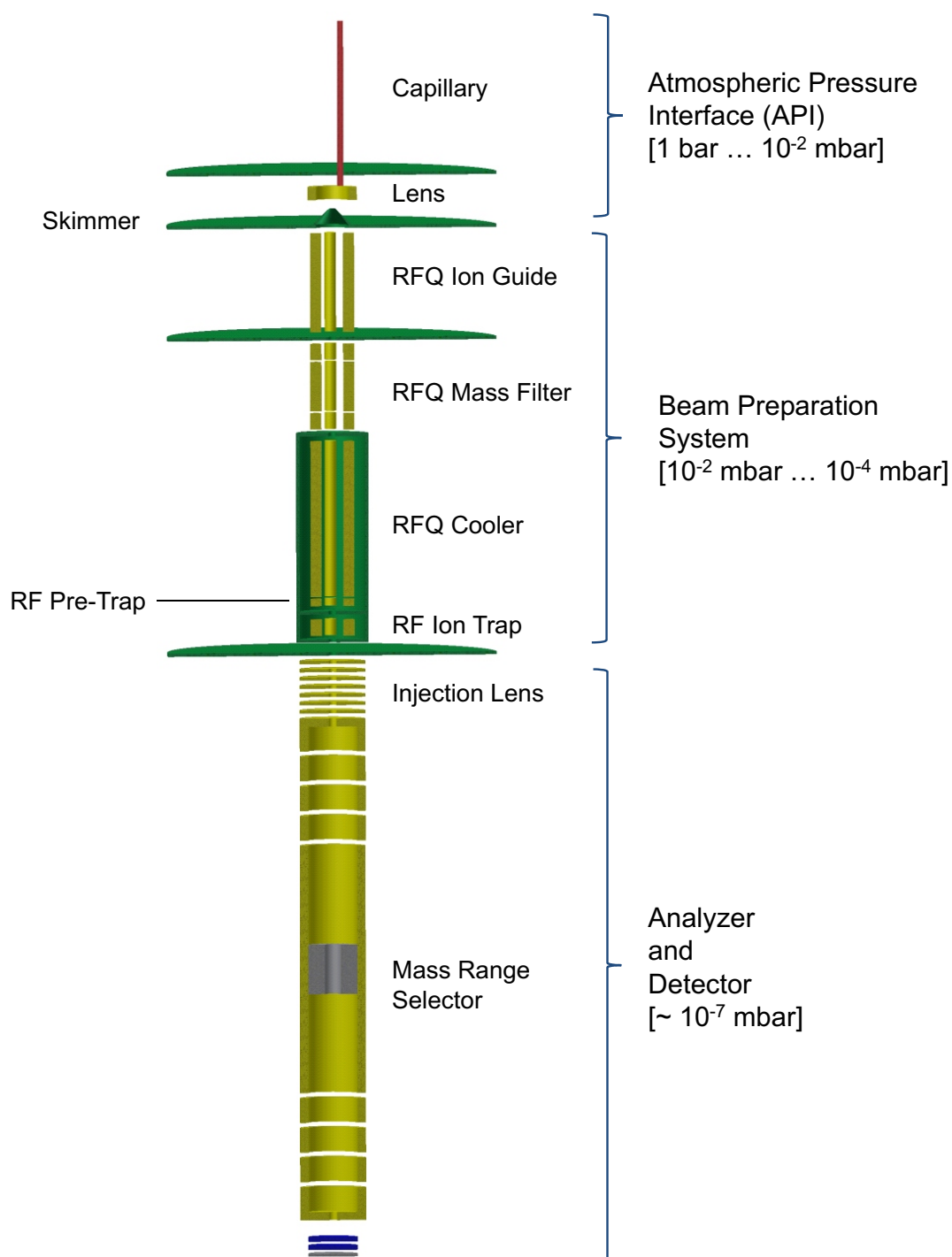
Analyzer and Detector
[~ 10^{-7} mbar]

Figure 3.1: Schematic layout of the MR-TOF-MS. The ion optical part of the instrument can be divided into three different stages: (i) an atmospheric pressure interface, (ii) a beam preparation system and (iii) the mass analyzer with detector. The ion optical system is enclosed by three conventional vacuum crosses (not shown); the green segments indicate stages of differential pumping.

3.1.1 Atmospheric Pressure Interface

The atmospheric pressure interface on top of the instrument is designed to couple various atmospheric ion sources to the mass spectrometer. Its purpose is to allow for highly efficient transport of the ionized analyte into the beam preparation system.

After sample ionization at atmospheric pressure, ions will be guided into the system by a heated capillary of about 12 cm length and an inner diameter of less than a millimeter. Temperatures around 70 °C prevent ions from adsorbing on the inner walls of the capillary and accelerate solvent evaporation. An ion-optical lens focuses the ion beam into the next vacuum stage, which contains an RFQ ion guide. A cone-shaped skimmer is used to separate these first two vacuum stages. This skimmer is placed slightly off-axis in regard to the inlet capillary. Thereby, the gas flow is not directly headed into the ion guide's vacuum stage and the ion current is automatically separated from the remaining neutrals. The RFQ ion guide confines the ions radially and guides them into the beam preparation system with an electrostatic field that is created along its resistive RFQ rods. The ion guide is operated at a pressure of roughly 10^{-2} mbar, and thus takes advantage of collisional cooling.
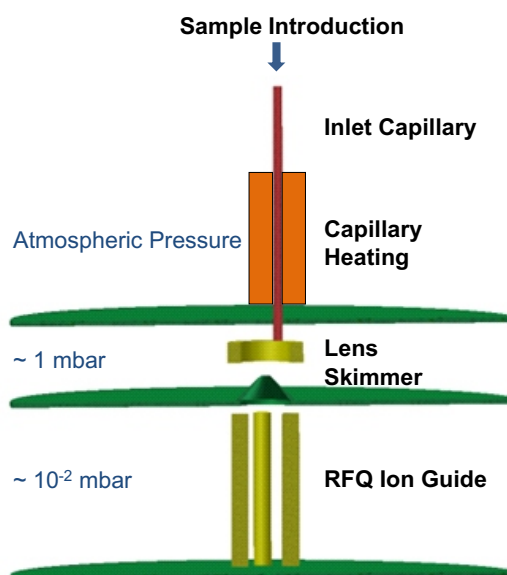
Figure 3.2: A detailed schematic view of the atmospheric pressure interface. The API ensures highly efficient transmission of the ionized sample from the ion source to the beam preparation system. Its layout is based on an electrospray interface for liquid chromatographs and mass spectrometers [Whitehouse et al., 1985].

3.1.2 Beam Preparation System

The beam preparation system prepares the ions provided by the API for ion injection into the analyzer (see fig. 3.3). It consists of a mass filter, a cooler together with the so-called pre-trap, and the ion trap. All four of these ion-optical elements are radiofrequency quadrupoles.
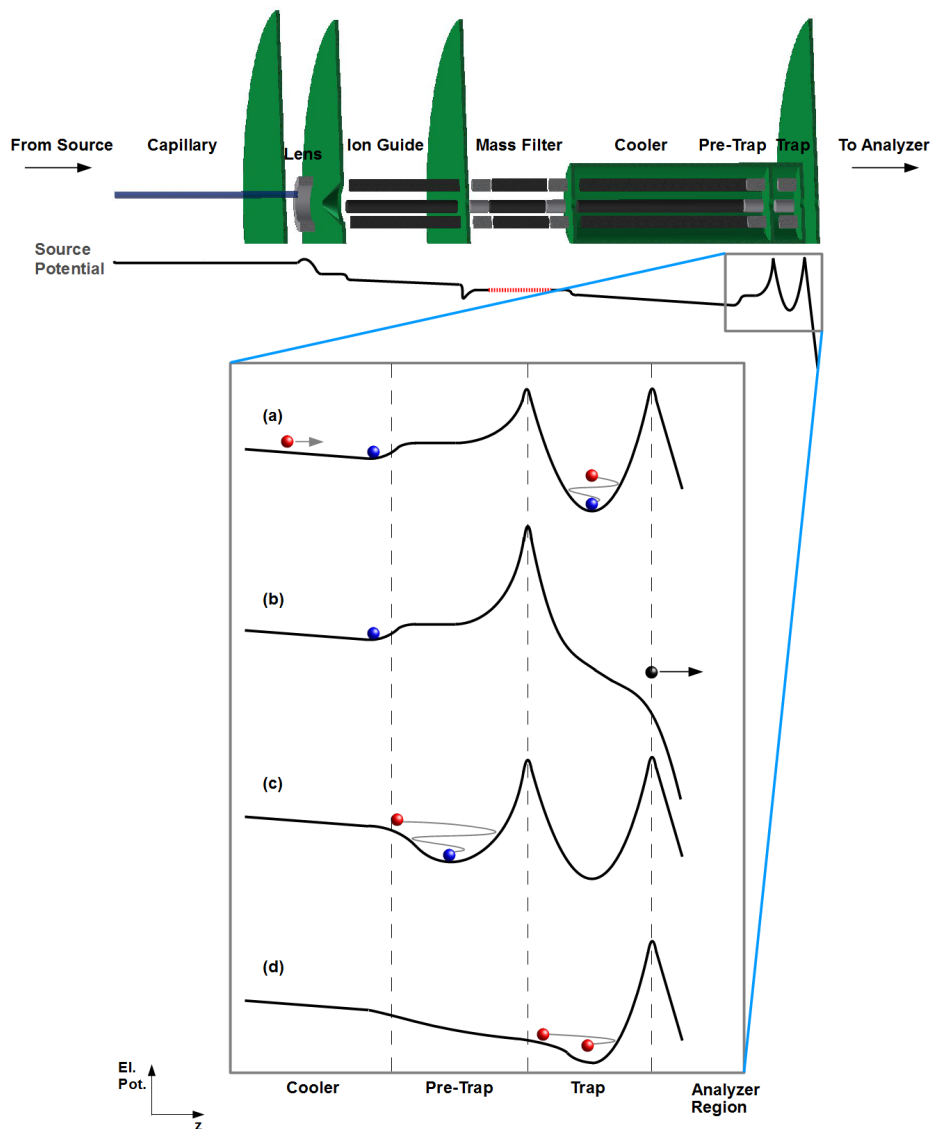

Figure 3.3: Illustration of ion transport and cooling in the last segment of the beam preparation system; the black line indicates the course of the electric potential along the ion-optical axis, the colors of the ions indicate their kinetic energy (red: "high", blue: "low"). The ions are cooled in the RF ion trap (a), before they are injected into the mass analyzer while the pre-trap prevents the remaining ions from getting distorted by the pulsed field (b). During this process, further ions are accumulated in the cooler and pre-trap (a-c), and then transferred to the ion trap (d) [Lang, 2016].

A mass filter positioned behind the API of the MR-TOF-MS has two advantages: the ion load for the subsequent parts of the instruments is reduced and the mass spectrum is cleaned from unwanted ion species. The mass filter consists of two additional Brubaker lenses [Brubaker, 1968] which are operated without a DC quadrupole field to improve ion transmission into and out of the mass filter quadrupole. Apertures placed in front and behind the mass filter separate the different pressure regimes of the beam preparation system. Two (instead of just one) apertures are placed between the ion guide and the mass filter. Since the second aperture is on a lower electric potential, these two apertures in combination with the mass filter quadrupole act as an electrostatic lens to provide for additional focusing of the ion beam [Lippert, 2012b].

The mass filter region is evacuated with a turbomolecular pump down to a pressure of 10^{-4} mbar, whereas the cooler and traps are operated with an external buffer gas (typically He or N_2) with a pressure of about 10^{-2} mbar. Both regions are physically separated by an encapsulation that solely contains the cooler and ion traps. Ions coming from the mass filter are cooled and stored in the cooler/pre-trap and are then transferred to the ion trap. As for the ion guide, an axial electric field is used to transport the ions along the RFQ cooler. The final cooling process takes place in the ion trap, and reduces the ions' phase space significantly. In the trap, the ions are stored by an RF field in radial direction and by an electric field generated by two apertures in axial direction. Figure 3.3 shows the process of ion accumulation and ion cooling in more detail.

The ion transport process from the pre-trap into the ion trap restricts the mass range of the MR-TOF-MS to about $m_{max}/m_{min} \approx 4$, due to the fact that the masses need to be simultaneously stopped in the ion trap as shown in simulations by [Wohlfahrt, 2011]. Since further ions delivered by the API are accumulated in the cooler/pre-trap during ion injection and time-of-flight analysis, the duty-cycle of the instrument in terms of ion processing can amount to almost 100%.

3.1.3 Time-of-Flight Analyzer

The time-of-flight mass analyzer is the key device of the instrument. Its design is based on a larger analyzer [Yavor et al., 2015], which was scaled down to fit into the compact instrumental setup of the MR-TOF-MS.

Before the ions enter the mirrors of the analyzer, they pass an electrostatic steerer quadrupole and the injection lens. The quadrupole is used to steer the ions' direction of flight to compensate for possible misalignments of the setup. These misalignments can be caused by small deviations in the construction or assembly of the ion-optical parts and may have a negative impact on the time-of-flight behavior of the ions.

Each of the four quadrupole electrodes can be put on a separate electric potential

to steer the ion beam in any direction in the x-y-plane. In addition, it can be used as an ion-optical lens. An injection lens is placed directly behind the steerer and focuses the ions into the analyzer. The combination of these two lenses allows to adjust the width and the angle of the beam at the focal plane independently.
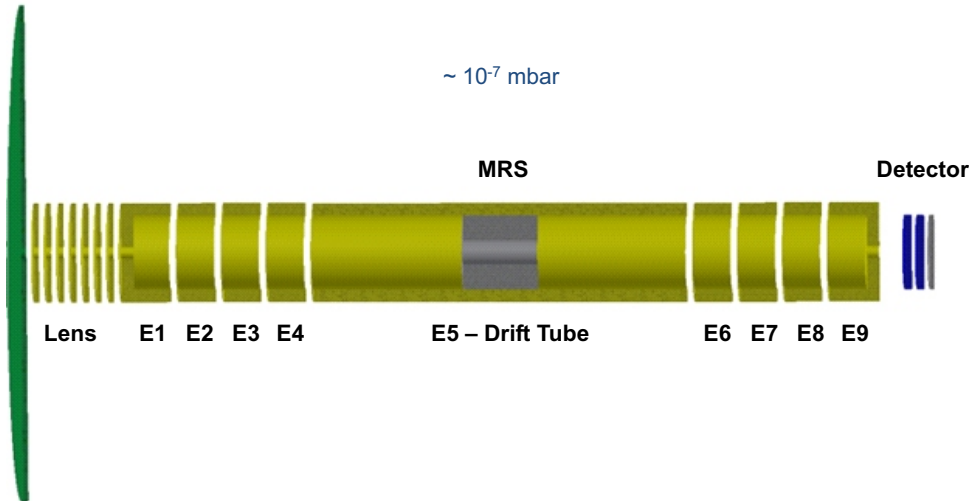

Figure 3.4: A schematic view of the MR-TOF-MS mass analyzer with detector. It consists of 9 electrodes (E1 to E9) and a mass range selector (situated in the drift tube). The steerer placed in front of the injection lens is not shown in this figure. A detector is placed at the end of the ion-optical system.

The 9 cylindrical analyzer electrodes are co-axially aligned and symmetric with respect to the drift tube (E5) of the system. The drift tube is the largest element of the analyzer and provided with an electric potential of -1300 V (also called "drift potential"). Depending on the ion-optical mode of the analyzer, the electrodes are supplied with a high voltage of up to 6 kV. For ion injection and ion ejection, the voltages of the electrodes E1 and E2, as well as those of E8 and E9 are pulsed to a lower values, allowing the ions to pass through the electrostatic mirrors. All voltages - except for the drift tube and E2/E8 voltages - are switched when the analyzer mode of operation is changed from TFS to normal mode (see section 2.4.5). The geometry and voltages of the analyzer electrodes are chosen such that the following ion-optical conditions are fulfilled after one reflection in NT mode [Yavor et al., 2015]:

$$(x|x) = (T|xx) = (T|\delta) = (T|\delta\delta) = 0 \tag{3.1}$$

As one can see, the linear and 2nd order aberration coefficients in position and energy vanish. Since the analyzer is of cylindrical symmetry and several coefficients are interdependent (i.e. fulfill symplectic relations, see [Wollnik, 1987]), many

other aberration coefficients vanish, too [Yavor et al., 2015]. Hence, the time-of-flight of the ions becomes independent of small deviations of the ion-optical parameters from the reference values.

The so-called mass range selector (MRS) is a quadrupole element placed in the middle of the analyzer. Together with the steerer, it can be used to correct the ions' flight path by adjusting the beam angle and the position at the focal plane. However, its main task is to filter out those ions that are not of interest for the particular mass measurement. A periodically switched electric dipole field deflects the unwanted ion species to the walls of the analyzer. In this way an unambiguous mass spectrum is generated.

A detector with excellent timing characteristics is placed at the exit of the analyzer. A thin grid in front of the detector is utilized to post-accelerate the ions and compensates the detector's reduced detection efficiency with respect to heavy masses. This grid has to be operated at a much higher electric potential than the detector to avoid unwanted signals generated by electrons which can be emitted upon ion impact on the grid.

3.2 Instrumental Setup
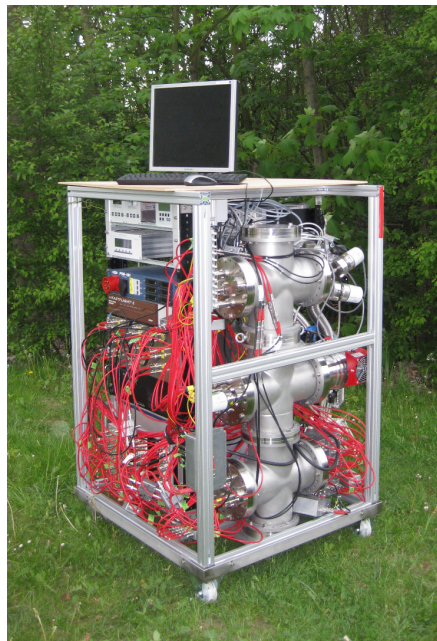
Figure 3.5: Photograph of the MR-TOF-MS illustrating the instrument's mobility. The MR-TOF-MS is of 0.8 m^3 volume only and has no other infrastructural requirements than a 220 V power connection. The frame comprises the whole instrument, including all power supplies and support electronics (left), and the vacuum housing of the ion-optics (right).

Figure 3.5 is a photograph of the MR-TOF-MS. The whole setup fits into one aluminum frame. The mechanical, electronic and vacuum components of the instrument as well as the software that is used during operation is discussed in the following sections.

3.2.1 Mechanical Setup

3.2.1.1 API

The design and construction of the API is described in the work of [Ebert, 2011, Lang, 2016]. Its vacuum chamber is divided into three aluminum components and can be connected to the overall system via a DN 160 CF flange (see fig. 3.6). The stainless steel capillary that is used to transport the ions from the ion source into the mass spectrometer is enclosed by a cased seal made of polyether ether ketone (PEEK). PEEK is an organic thermoplastic polymer that serves as electrical and thermal insulator. The inlet capillary is heated by a block of copper, which, in contrast, is an excellent thermal conductor. Four safe high voltage (SHV) connectors are attached to the side of the API and supply the electrodes with the desired voltages. The position of the capillary in vacuum can be adjusted by placing it into one of four holes that are drilled into a stainless steel element that is put on top of the API lens. A turbomolecular pump is connected to one side of the API via a DN 63 CF connection and evacuates the chamber, which also contains the RFQ ion guide.
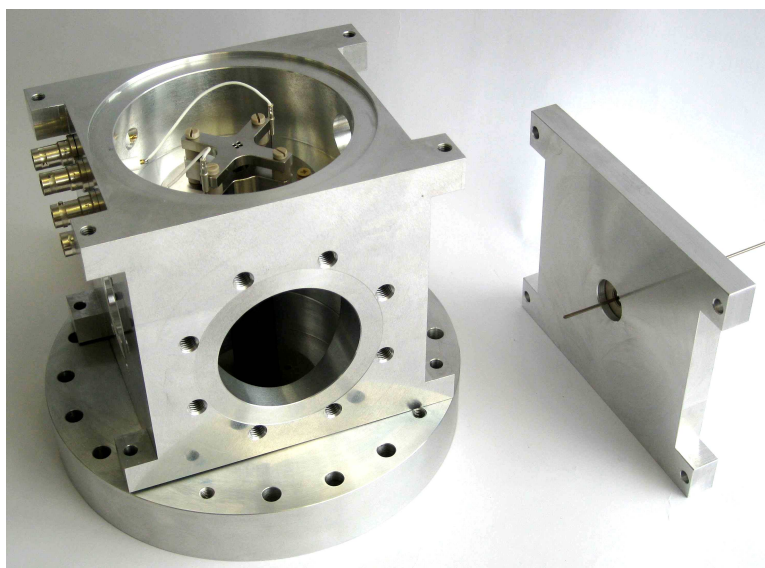
Figure 3.6: Photograph of the atmospheric pressure interface. The API is unitized into three aluminum components and can be attached to a DN 160 CF vacuum cross.

3.2.1.2 Beam Preparation System

The radiofrequency quadrupoles of the MR-TOF-MS are either made of stainless steel (mass filter, ion traps) or a resistive material composed of PEEK and carbon (ion guide, cooler). The latter type of RFQ is used whenever an additional axial electric field is needed to guide the ions through regions of pressure of the order of 10^{-2} mbar. Due to easier manufacturing, the quadrupoles consist of four cylindrical instead of hyperbolically shaped rods. Deviations from a perfect electric quadrupole field can be minimized by choosing the rod radius R and r_0 (distance between the electrodes' surface to the beam axis) such that $\eta = \frac{R}{r_0} \approx$ 1.14511 [Reuben et al., 1996]. For the quadrupoles of the MR-TOF-MS, R was chosen to be 4 mm and $r_0 = 3.5$ mm, resulting in an η of about 1.14286. The rods are mounted into PEEK holders. Stainless steel pins fix them in place and provide for electrical contact. The various RFQ stages are separated by stainless steel apertures with hole diameters between one and three millimeters, which serve as separators for the differential pumping of the system.

3.2.1.3 Analyzer

The electrodes of the time-of-flight analyzer are made of the nickel-iron alloy Invar. Invar has a very low thermal expansion coefficient and renders the electrode arrangement therefore very robust against changes in temperature. Alignment as well as spacing of the lens electrodes is done with ceramic pins and rings. Small holes in the drift tube allow for efficient pumping of the lower part of the instrument. The detector holding is mounted to the bottom of the analyzer and provides enough space for an MCP detector or an MagneTOF electron multiplier. The whole analyzer is attached freely suspended to a flange above the analyzer via three long rods (compare with fig. 3.4). Thus, its alignment is done with respect to the trap system and minimizes misalignments of the analyzer as much as possible.
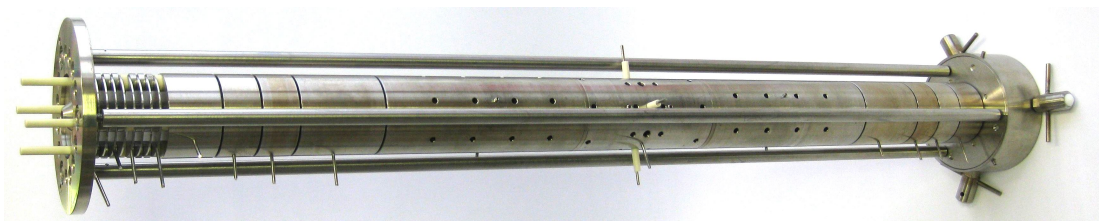

Figure 3.7: Photograph of the time-of-flight analyzer. The ions enter the analyzer from the left by passing the injection lens and are finally focused on the ion detector at the exit of the analyzer. Stainless steel pins provide for electrical contacts, and small holes in the drift tube allow for efficient pumping.

3.2.2 Vacuum Setup

The vacuum setup is illustrated in figure 3.8. One roughing pump and three turbomolecular vacuum pumps evacuate the system to the desired pressures. Pressure region (4) has a gas inlet for buffer gas that is used to cool the ions inside the RFQ cooler and ion traps. The roughing pump can be placed inside of the instrument's frame. It takes less than an hour to achieve the analyzer pressure that is needed to start mass measurements, which is typically of the order of 10^{-7} mbar.
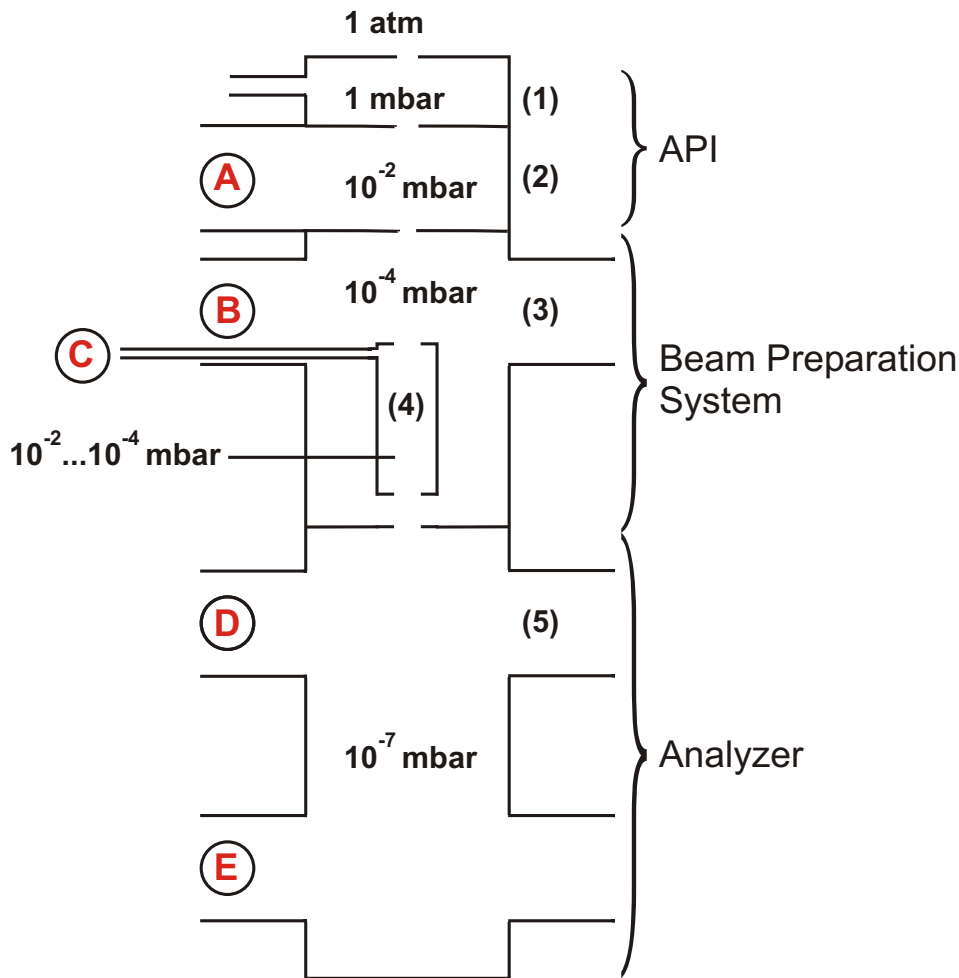
Figure 3.8: Illustration of the vacuum setup of the MR-TOF-MS with its approximate pressure values. The vacuum flanges are equipped as follows: (A) Turbomolecular pump Pfeiffer HiPace 80, gauge Peiffer PKR 251. (B) Turbomolecular pump Pfeiffer TMU 071 YP, gauge Pfeiffer PKR 251. (C) Gas inlet for RFQ cooler. (D) Turbomolecular pump Pfeiffer HiPace 300. In addition, the flanges (A), (B), (D) and (E) are equipped with electrical feedthroughs. The roughing pump is of type Ebara PDV500 (and additionally evacuates region (1)) [Lippert, 2012a].

3.2.3 Electronics

3.2.3.1 Generation of Radiofrequency Signals

The radiofrequency signal that is applied to the quadrupoles has typically a frequency of one to two MHz and a peak-to-peak amplitude of several hundred volts. This signal is generated by resonant excitation of an LC circuit [Kondradi and Ayet San Andrés, 2015]. To provide signals of the same amplitude but 180° shifted phases, two toroidal inductor coils with inductance L are resonantly driven by a rectangular low voltage signal. The circuit amplifies the input signal by a factor of up to 100 and provides a sinusoidal output signal. Since the capacitance of the quadrupole electrodes is negligible, the SHV cables outside the vacuum and the electrical feedthroughs represent the main contribution to the total capacitance C of the circuit. For a fixed angular frequency $\omega = \frac{1}{\sqrt{LC}}$, the required values for the Mathieu parameter q_u can be adjusted by tuning the amplitude of the signals. To minimize cross-talk, wires of opposite phase are twisted inside the vacuum. SHV cables of equal lengths are important to ensure equal amplitudes for both phases.

3.2.3.2 High Voltage Switching

The electric potentials of the ion trap and most of the analyzer electrodes have to be changed periodically. This switching of voltages is performed, for example, when ions are injected into the analyzer or when the mode of operation of the analyzer needs to be changed (from TFS mode to NT mode for instance). The task of switching between different sets of voltages is realized by custom-made high voltage switches [Petrick, 2010, Ayet San Andrés, 2015]. A transistor-transistor logic (TTL) signal sets the time at which the change of voltages occurs. The different voltages are applied to the inputs of the voltage switch and the desired voltage is then put on the output accordingly. It is very important that the switching of voltages is performed on the sub-microsecond time scale, so that the ions of interest experience only static electric fields. The switches can be connected in series in order to allow for more complex timing schemes. To assure fast switching, the capacitive load on the output of the switches has to be minimized. Hence, short SHV cable lengths are essential.

3.2.3.3 Passive Voltage Stabilization

High-resolution mass measurements with the MR-TOF-MS are only possible if the voltages applied to the analyzer electrodes are very stable and are affected as little as possible by electrical noise. This is especially important for the voltages applied during normal turn mode, since the analyzer remains in that mode of operation during the major part of the ions' flight time.

Thus, custom-built electronics is used to passively stabilize the voltages of commercially available high voltage supplies [Ayet San Andrés, 2014]. The voltage stabilization for electrodes E1 to E3 consists of a 4th order low-pass filter with a cut-off frequency $f_C = 1.6$ Hz. The low-pass filter for E4 utilizes a slightly different design, because a higher voltage is used. Its RC filter is of first-order with a cut-off frequency $f_C = 5.3$ Hz. For the opposite reflector (electrodes E6 to E9), the same electrical design is used.

Due to the load of the RC circuit, the output voltages of the stabilization box will always differ from the voltages that are delivered by the outputs of the voltage supplies. Furthermore, a change in timings of the analyzer's pulsing scheme will affect the output voltage as well. Hence, to allow for easy monitoring, an additional output channel is mounted to the front of the box for each of the NT mode voltages. Thereby the NT voltages can be easily checked without changing the setup in terms of either cabling or load.

3.2.4 Software

3.2.4.1 Voltage Control Software

A dedicated program was developed to control the low and high voltage power supplies of the MR-TOF-MS [Lotze, 2014]. Channels can be named, color-coded and grouped, and are arranged in a well-structured user interface. The target voltage and ramping speed can be individually set for each voltage channel. Furthermore, the maximum current that is delivered by the power supplies can be limited to prevent any damage to the electronics. Target voltages can either be directly entered or calculated in dependence of other channels by formulas. The actual voltage, which is provided by the power supplies, is read out and displayed. Network access to the software can be granted and allows for remote control and voltage modification by other programs. For convenience, voltage settings can be saved and loaded.

3.2.4.2 MAc Software

MAc is a powerful multi-purpose software that undergoes continuous development to meet the accreting needs and increasing performance of the MR-TOF-MS [Pikhtelev, 2014, Bergmann, 2015, Bergmann, 2016]. It comprises acquisition, processing and analysis of data, as well as voltage optimization algorithms and time sequencer control.

Figure 3.9 illustrates the amount of different tasks that are fulfilled by MAc. It can communicate with the voltage control software to optimize the voltages of the beam preparation system and the analyzer via dedicated algorithms, like the

nelder-mead method for instance [Nelder and Mead, 1965]. The system's time
sequencer control (see section 4.1.5) is also directly integrated into the software.
MAc supports various data acquisition hardwares, ADCs (analog-to-digital con-
verters) like the Signal Recovery FastFlight2, as well as TDCs (time-to-digital
converters) like the Fast ComTec MC6SA. Data processing, such as mass cali-
bration and peak identification, can be handled on-line and off-line. With the
so-called "time-resolved calibration" (TRC) it is possible to compensate for time-
dependent voltage drifts and further enhance the mass resolving power of the
instrument. The implementation of combinatorial algorithms in combination
with atomic mass evaluation data allows for accurate mass determination and
peak identification, a feature that is especially helpful to identify unknown com-
pounds.
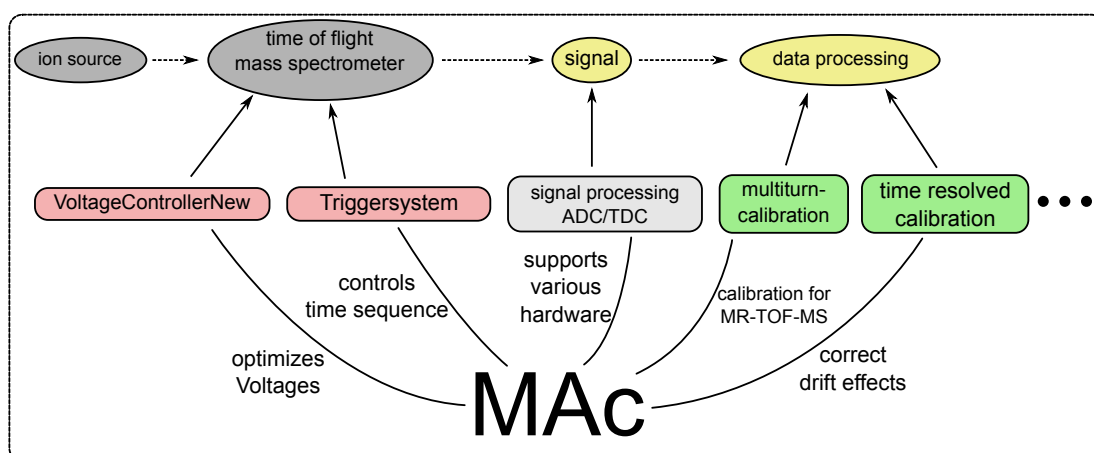
Figure 3.9: Scheme of the MAc software. MAc is an integral part of the MR-
TOF-MS and is involved in the whole measurement process, from
voltage control to data processing [Bergmann, 2015].

4 Instrumental Developments and Measurement Settings

4.1 Technical Improvements

In the following, the most important technical improvements that have been applied to the MR-TOF-MS to prepare for the measurements in the framework of this thesis are presented. First, the transport efficiency and robustness of the ion guide and beam preparation system have been increased. Furthermore, electronics necessary for the operation of the mass filter was installed. Essential upgrades have been performed to the ion trap and the TTL trigger system to improve high-resolution mass measurements and mass-selective ion re-trapping. These upgrades in combination with the implementation of collision-induced dissociation for the fragmentation of molecules enable new and outstanding tandem mass spectrometry experiments. In addition, the MCP detector was replaced by a MagneTOF detector, rendering the investigation of space charge effects in the time-of-flight analyzer possible.

4.1.1 Resistive RFQs

For quantitative analysis as well as for stable and easy operation, an efficient inlet/beam preparation system is essential. Therefore, the resistive RFQs of the MR-TOF-MS have been overhauled, and the circuit board used for mixing of RF and DC signals has been completely revised (see section 4.1.2).

Radiofrequency quadrupoles that are operated at vacuum pressures of 10^{-2} mbar to 10^{-3} mbar need an additional axial field to transport ions efficiently through the residual gas. This field can be provided by segmented RFQs [Dodonov et al., 1997, Javahery and Thomson, 1997] or quadrupoles with linearly inclined electrodes [Mansoori et al., 1998]. A relatively new approach is to use resistive RFQs [Takamine et al., 2007, Simon, 2008] (compare with fig. 4.1).

The electrodes of these quadrupoles consist of a resistive material that creates a continuous gradient when different voltages are applied to both ends of the rods. This technique is utilized in the MR-TOF-MS, where the resistive RFQs are made of carbon and PEEK. The correct mixing ratio of both materials is

crucial for proper functioning of the quadrupoles. On the one hand, the rods have to be sufficiently conductive over their entire length to provide the desired electric field. On the other hand, the rods' resistance has to be high enough so the low voltage power supplies can operate within their given current limitations.
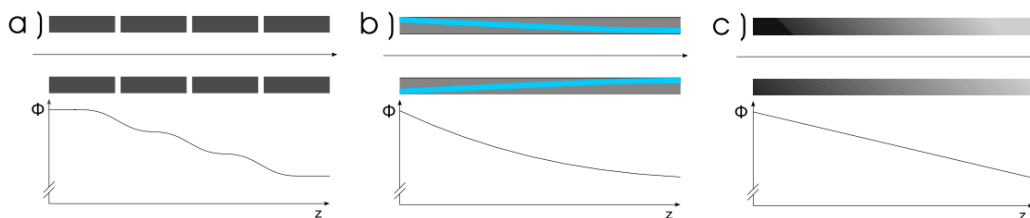

Figure 4.1: Three types of radiofrequency quadrupoles and their electric potential on the symmetry axis. A) segmented RFQ, b) RFQ with inclined electrodes, c) resistive RFQ [Becker et al., 2009].

In this work, the composition of the MR-TOF-MS' resistive RFQs has thus been optimized. The operation of the improved RFQ ion guide and RFQ cooler has proven to be reliable during all measurements of this work and guarantees an increased overall transport efficiency of the system.

4.1.2 Mixing of RF and DC Signals

A custom-built circuit board consisting of capacitors, inductors and resistors is used to mix RF and DC signals designated for the RFQs of the beam preparation system. The components of this board have a capacitance $C = 10$ nF, a resistance $R = 100$ kΩ and an inductance $L = 800$ μH. The voltage tap for the electrodes is situated between these elements (see fig. 4.2 for the layout of the circuit), and the board is placed inside the vacuum setup to reduce the amount of cables and SHV feedthroughs needed. Consequently, additional care has to be taken with respect to the components to be used.

Since the inductors installed in a previous version of the mixing board were not able to withstand long operations due to the generation of heat, they had to be replaced. The new inductors are made of two large ferrite cores and are well suited for high voltage and in-vacuum operation.
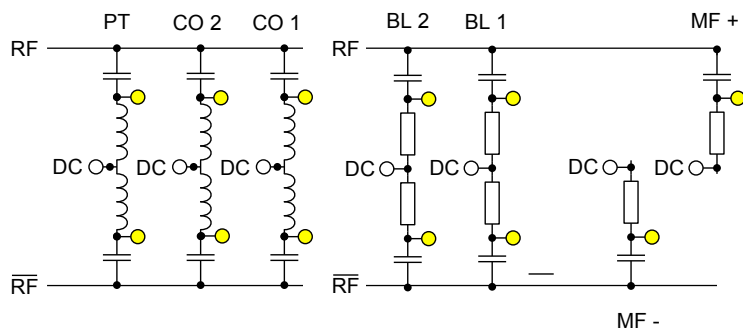
Figure 4.2: Schematic layout of the new RF/DC mixing board. Yellow circles indicate points of voltage tap. The RFQ cooler is provided with two separate DC voltages, which create the declining electric potential along the beam axis. Also, different potentials are applied to both RF phases of the mass filter to establish the DC quadrupole field. PT: pre-trap, CO: cooler, BL: Brubaker lens, MF: mass filter.

Furthermore, the new RF/DC mixing board was designed in a way that each mass filter component can now be separately supplied with its designated voltage (compare with fig. 4.2). Both of the Brubaker lenses can be supplied with different DC voltages to improve ion transmission by creating steps in the electric potential. The actual filter is connected to two DC voltages that create the time-independent quadrupole field, which is then superimposed on the radiofrequency signal.

To ensure independent optimization, the cooler RF signal was separated from the mass filter RF signal. This improvement was realized to all the instrument's quadrupole stages, meaning that ion guide, mass filter, cooler and ion trap have been connected to individual RF circuits. The operational parameters of the mass filter (i.e. the Mathieu parameters) can be adjusted by variation of the RF amplitudes and DC voltages.

4.1.3 Resonance Excitation for CID

The MR-TOF-MS has been developed to combine the ability to process and identify analytes in complex samples with the possibility to measure these samples in the field. For the unambiguous identification and structural elucidation of molecules, tandem MS is an essential prerequisite. Consequently, collision-induced dissociation, a standard dissociation technique in analytical mass spectrometry, has been implemented in the instrument.

For the application of CID as fragmentation method, resonance excitation in the RF ion trap has been implemented. For this, the electric circuit of the RF ion trap had to be revised. Instead of pairwise supply of voltages to the opposite electrodes of the quadrupole, each of the four electrodes is now separately connected to the

voltage supplies. Since dissociation of the molecules can be achieved by exciting the ions' macromotion in the ion trap (see section 2.3.2), a sinusoidal low voltage signal is added to the radiofrequency signal of one of the quadrupole segments. Therefore, the resulting field superimposed onto the RF field consists of dipolar and quadrupolar parts (instead of being of pure dipolar nature), which is shown in figure 4.3. This choice was made to simplify the CID circuit.
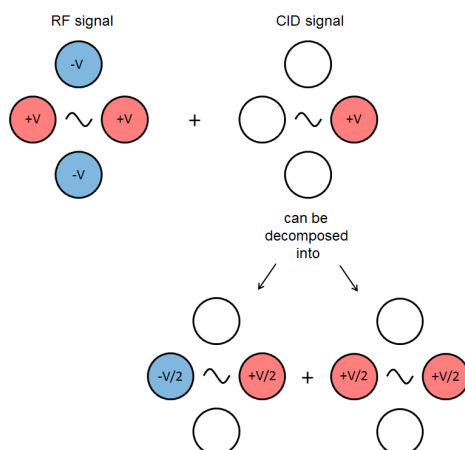

Figure 4.3: Illustration of the superposition of RF and CID signal for the ion trap. A signal with an amplitude of a few volts is applied to one of the quadrupole segments in addition to the RF signal. The AC dipole (bottom left) will excite the ions' macromotion in the pseudo-potential of the trap.

The electric setup of the ion trap can be found below in figure 4.4.
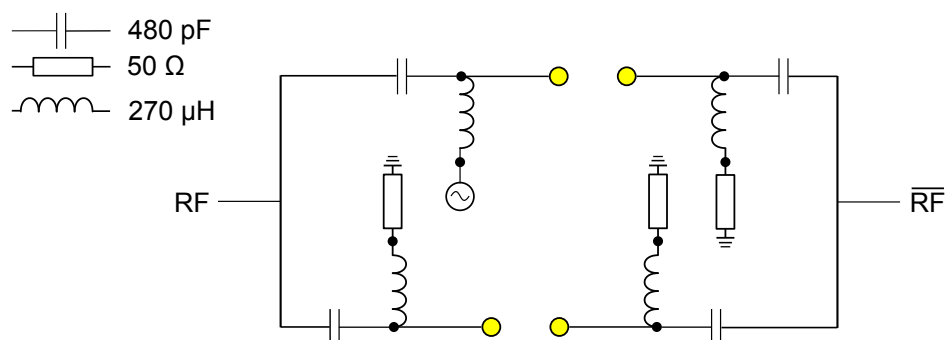
Figure 4.4: The electric circuit of the ion trap. Yellow circles indicate connections to the quadrupole segments. One of the segments is connected to a signal generator with an internal termination of $50\ \Omega$. This generator signal provides the auxiliary electric potential that is used to perform collision-induced dissociation in the ion trap.

The electric circuit was designed and tested with a dedicated software [DesignSoft, 2012]. The frequency of the RF signal is typically between 1 MHz and 2 MHz, whereas the frequency of the macromotion is an order of magnitude smaller. The exact value of the resonance frequency depends on the Mathieu parameters of the particular ion of interest (see eq. (2.11)). It has to be considered that the signals do not only differ largely in frequency, but also about two orders of magnitude in amplitude. Hence, damaging of the function generator by the RF signal has to be avoided. The values for the impedances used have been determined accordingly. Figure 4.5 shows the mixing of two signals (simulated with [DesignSoft, 2012]).
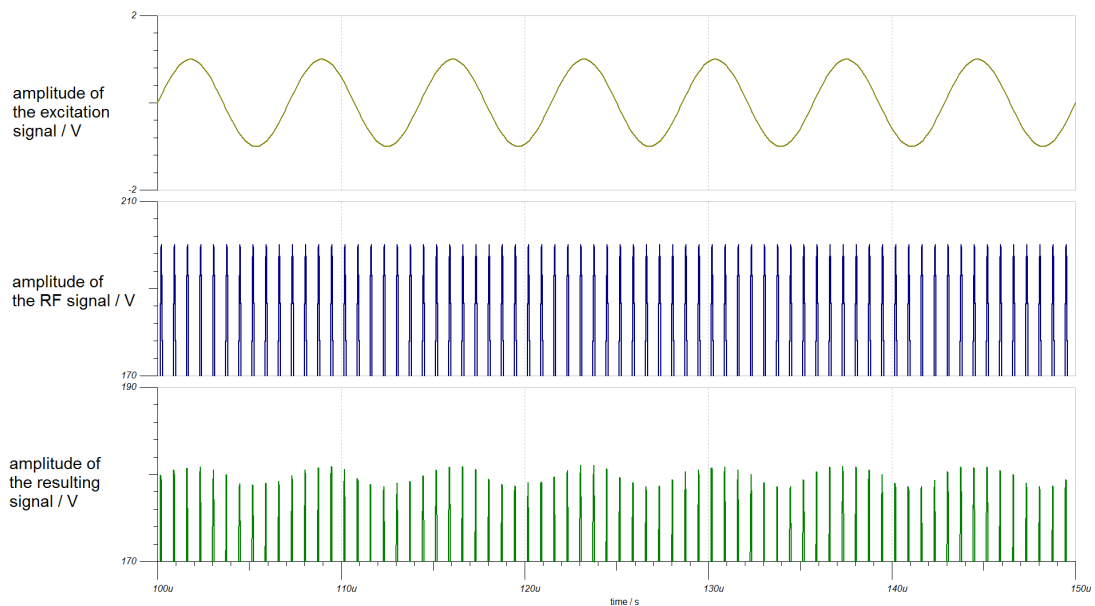
Figure 4.5: Mixing of an RF signal (middle, $V = 200$ V, $f = 1.4$ MHz) with an excitation signal (top, $V = 1$ V, $f = 140$ kHz). The result (bottom) is a slightly attenuated RF signal with an additional ripple caused by the low voltage signal.

4.1.4 Ion Trap Shielding Aperture

An additional aperture has been placed between the ion trap and the steerer. This aperture is positioned 4 mm behind the second trap aperture and shields the trap region against electric fields originating from the steerer (compare with fig. 4.6). The shielding aperture is hardwired with the second aperture of the trap inside the vacuum. Hence, each of the electric potentials (namely trapping and re-trapping potentials as well as the injection/retarding potentials) is simultaneously applied to both apertures.
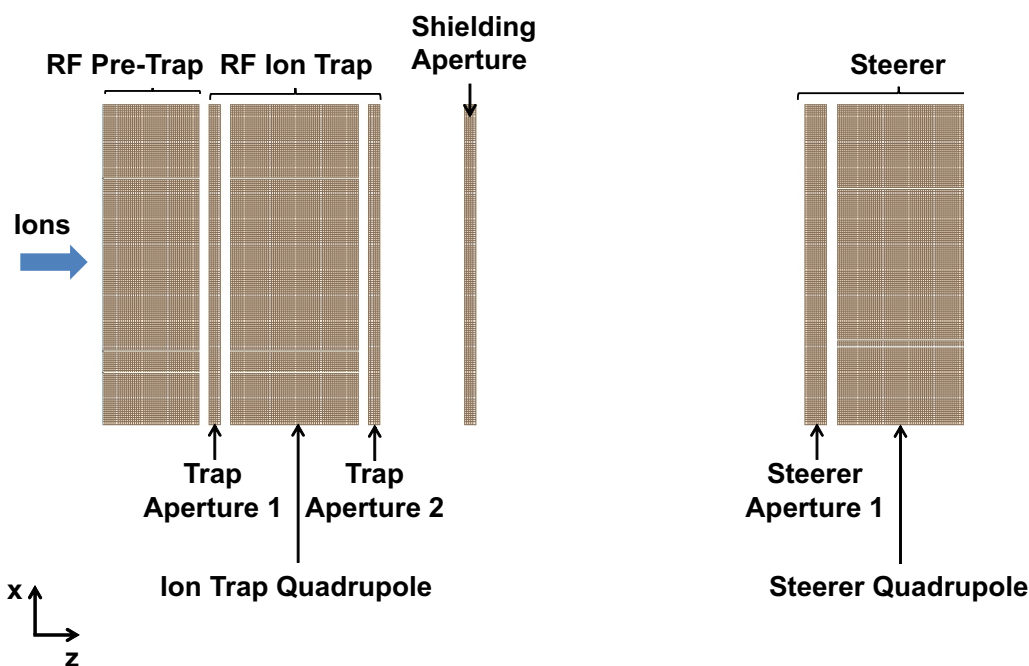
Figure 4.6: A cross-section through a SIMION model of the MR-TOF-MS ion-optics. The shielding aperture is placed between the ion trap and the steerer and prevents the steerer from penetrating the electric fields of the ion trap. The voltage difference that is applied between trap aperture 2 and steerer aperture 1 is about 1.3 kV.
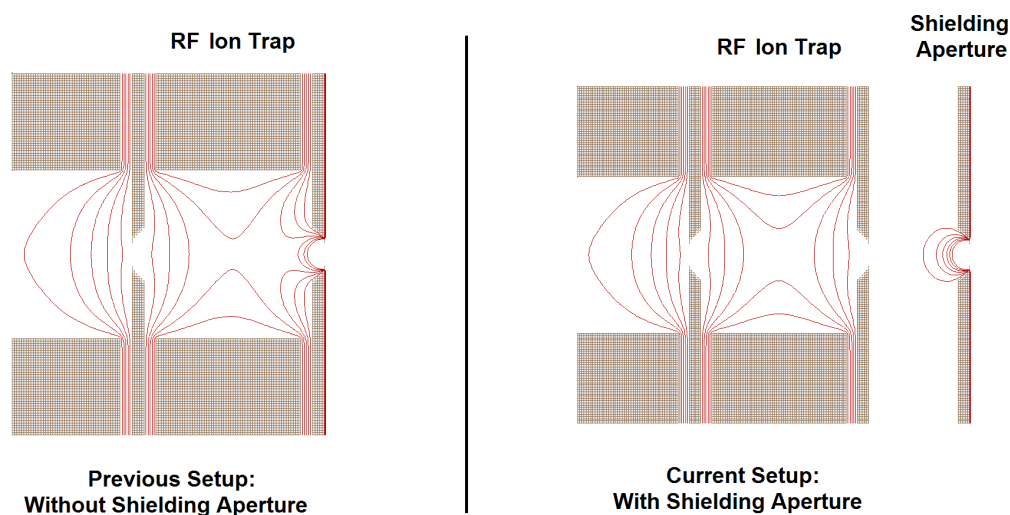
Figure 4.7: Electric potential lines in the ion trap region without and with shielding aperture. The voltage applied to the trap apertures in this simulation is 3 V. In the previous setup, the electric field of the steerer, which is operated at a voltage of -1.3 kV, was able to reach into the the ion trap (left side). With the new shielding aperture, a distortion of the trap's electric field is strongly suppressed (right side).

If the shielding aperture was absent, the steerer's electric field would penetrate into the trap region and therefore result in an asymmetric trap potential. This behavior is depicted in figure 4.7, where one can clearly see the difference in the trap's field symmetry between the previous and the current ion-optical setup of the MR-TOF-MS. Thus, the absence of a shielding aperture would cause losses in terms of re-trapping performance [Yavor and Lippert, 2014]. The axial potential would already disappear at a re-trapping voltage of around 3 V on the trap apertures (the DC potential of the RFQ is at ground potential). Also, the ions' stopping position would deviate from their initial position whenever the re-trapping and trapping potential were different. In this case, the ions would never be completely stopped by the retarding field of the ion trap. Reduction of separation power and re-trapping efficiency would be inevitable.

4.1.5 TTL Trigger System

During operation of the MR-TOF-MS, the electrodes' voltages are switched up to several thousand times per second. This involves the beam preparations system in the form of the ion traps (transfer, storage, injection and re-trapping of ions) as well as the time-of-flight analyzer (different analyzer modes). The overall time scheme of the MR-TOF-MS operation is composed of many different time signals that have to be synchronized with each other. The time intervals of the signals are typically between a few μs and several ms long. A dedicated time sequencer is needed to produce this timing procedure.

For this reason, an FPGA-based (field-programmable gate array) time sequencer has been built [Jesch, 2016]. This trigger system produces TTL signals that are passed to the voltage switches via LEMO push-pull connectors. As can be seen in figure 4.8, the interface of the system consists of 64 TTL outputs (32 individual channels) and a monitor output that can be connected to a logic analyzer.

Figure 4.8: Picture of the TTL trigger system. Its interface consists of 64 TTL outputs (32 individual channels) and a monitor output [Jesch, 2016].

16 logic channels (XOR, OR and AND operations) can be used to link up to 4 of the 32 channels amongst each other. The counter system is capable of counter frequencies up to 250 MHz and provides the desired timings. The control of the time sequencer is part of the MAc software and allows for dynamic adaption of timings with respect to the ion's mass, turn number and measurement mode for instance. With this trigger system, even very complex requirements in terms of timing structure and flexibility can be fulfilled.

The TTL trigger system was integrated into the existing electronics of the MR-TOF-MS and has been successfully commissioned. All measurements of this work have thus been performed with the new system.

4.1.6 MagneTOF Electron Multiplier

The MCP detectors in chevron configuration that were formerly used have been replaced by a MagneTOF DM167 electron multiplier. This modification has been done to allow for measurements with improved and well-known detection efficiency, which was especially important for the conduction of space charge measurements (see section 6).

Furthermore, the electromagnetic interference (EMI) of the electronics in the time-of-flight spectrum could be reduced by more than one order of magnitude, which can be seen in figures 4.9 and 4.10. Here, the same settings were used during both measurements, except for the change of the ion detector. One can clearly see that the noise induced by pulsed analyzer electrodes at $t = 60$ μs is strongly decreased with the use of the MagneTOF detector. The reason for this improvement is probably a change in the cable configuration (e.g. a better ground connection) that has been induced concurrently with the change of detectors.
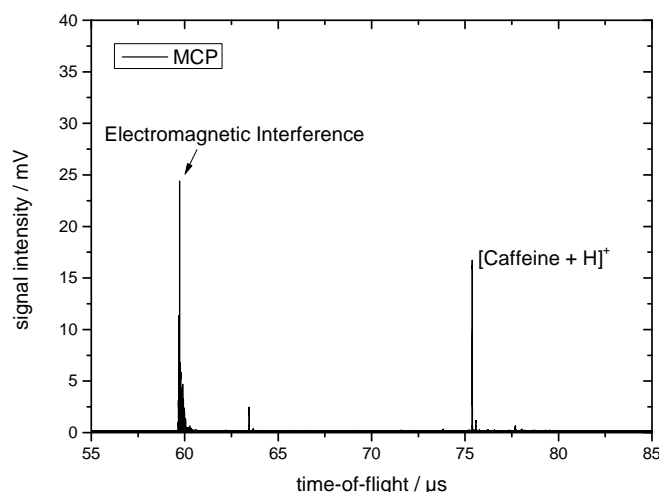
Figure 4.9: Time-of-flight spectrum recorded with the MCP detector. The peak at $t = 60$ μs is not a real ion signal, but caused by the pulsing of the analyzer electrodes.
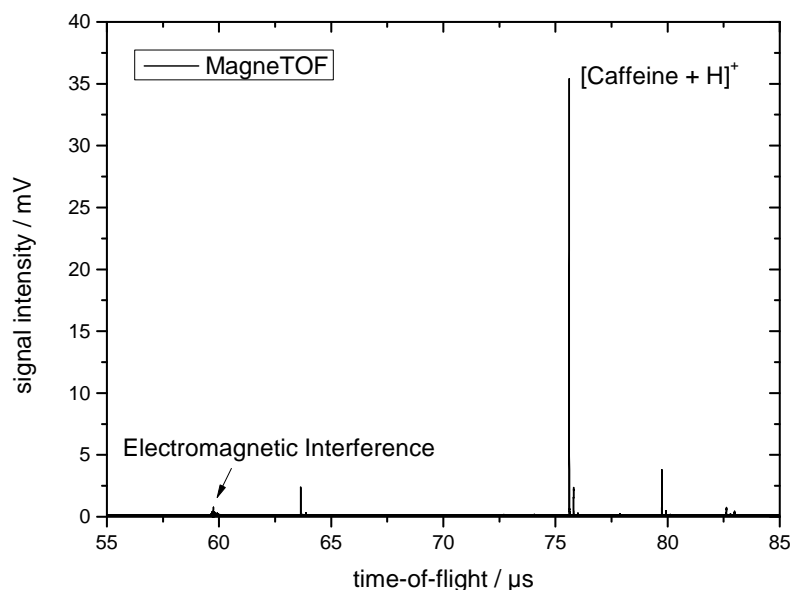
Figure 4.10: Time-of-flight spectrum recorded with the MagneTOF electron mul-
tiplier after detector exchange. The electromagnetic interferences of
pulsed electronics are vastly decreased, which strongly increases the
sensitivity of the system. The analyte's signal at $t = 75$ μs is the
most prominent peak in the spectrum.

4.2 Measurement Setup and Settings

4.2.1 Ion Source

A nano-electrospray ion source was operated during the measurements of this
work. As electrospray emitter a gold-coated glass tube with an outer diameter
of 1.2 mm and an inner diameter of 5 μm at its tip was used. The tube has a
volume of about 20 μl and was manufactured by DNU-MS GbR.

After the sample was funneled into the emitter with an Eppendorf Microloader
tip, the emitter was placed a few millimeters away from the inlet capillary of the
API and a high voltage of about 1.5 kV was applied (see figure 4.11). Under
these conditions, the ion source provided a quite constant ion current for up to
an hour before the emitter had to be refilled.
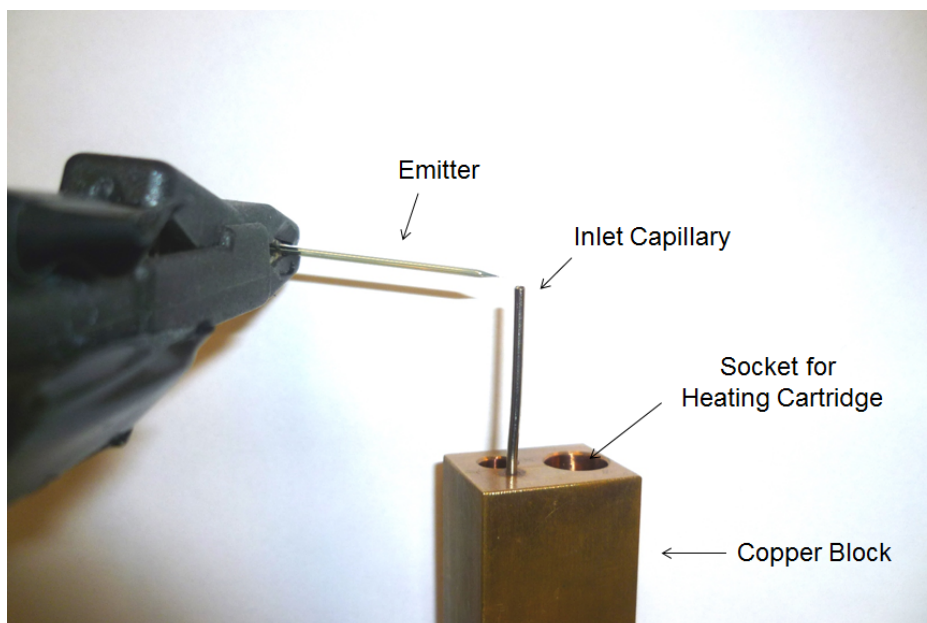
Figure 4.11: Picture of the nESI setup. The emitter is placed a few millimeters away from the capillary and a high voltage of about 1.5 kV is applied. A heated copper block encloses the capillary and supplies the desired temperatures (typically around 70 °C). The emitter is aligned orthogonally to the inlet capillary of the system to reduce the gas flow of neutrals into the API.

4.2.2 Timing Sequence

Ions that have been guided through the beam preparation system are accumulated in the cooler/pre-trap region, before they are transferred into the ion trap. For this transfer, the first aperture of the trap is pulsed to a lower voltage and then back to the storage potential again. This process takes a few microseconds, depending on the ions' mass-to-charge ratio. The ions are then cooled in the RF ion trap over a time span of a few up to several milliseconds. After reaching thermal equilibrium, the ions can be injected into the analyzer by applying an extraction potential to both trap apertures.

The electrodes E1 and E2 are in open mode to allow the ions to enter the analyzer. The timing scheme that is used for the reflector electrodes of the analyzer can be found in figure 4.12. In general, the state of all reflector electrodes is changed from open to TFS mode after ion injection and then changed to normal turn mode after one turn. The state of normal turn mode is kept for an arbitrary number of turns and only changed to open mode at the very end of the ions' time-of-flight.
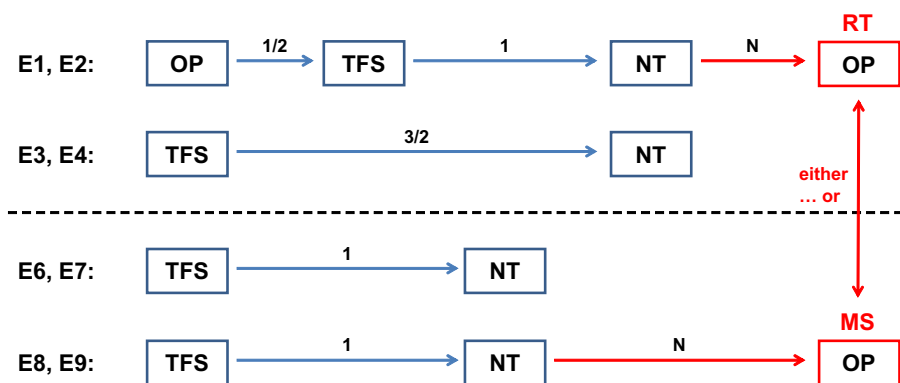
Figure 4.12: Timing scheme of the analyzer electrodes. The electrodes are switched between TFS, NT and open (OP) mode. The numbers above the arrows indicate the number of turns after which the switching is performed. The ions will either impinge on the detector by pulsing E8 and E9 to open mode (MS), or be guided back to the ion trap by switching the potentials of E1 and E2 if the analyzer is operated in re-trapping mode (RT).

The voltages of the ion trap and the time-of-flight analyzer can be switched such that either a mass measurement or ion re-trapping can be performed. Hence, the last switching to open mode is either applied to E8 and E9 to detect the ions on the detector or to E1 and E2 to recapture the ions in the trap. In the latter case, the ions are only re-trapped if the retarding electric field is pulsed back to storage potential at the right time. Both modes of operation are illustrated in figure 4.13. They can easily be switched on a cycle to cycle basis with the timing scheme that controls the voltage switches.
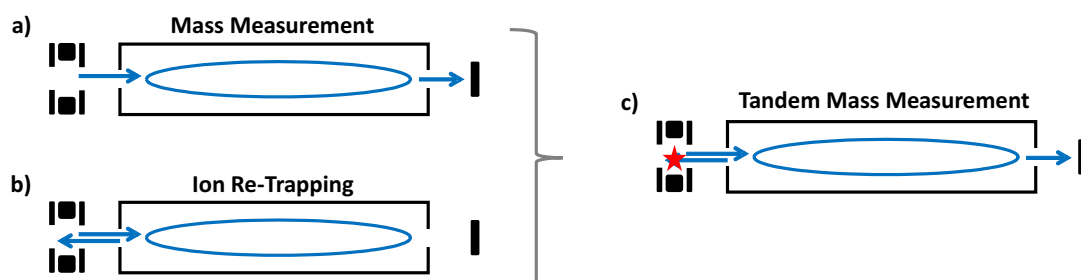
Figure 4.13: An illustration of the different operational modes of the MR-TOF-MS. The ion trap, analyzer and detector electrodes are represented by black, the ion trajectories by blue color. If one combines the mass measurement mode (a) with ion re-trapping (b) and CID, tandem mass measurements (c) can be performed.

Due to the fact that the pulsed fields may distort the trajectories of the ions, pulsing of a reflector is either performed when the ions of interest are located in the drift tube or in the opposite reflector. The same applies to the operation of the mass range selector. The dipole field of the MRS that is utilized to deflect unwanted ion species is only applied as long as the ions of interest are flying in the reflector region.

Overall, the time-of-flight for mass measurements or ion re-trapping can vary between a few tens of microseconds up to several tens of milliseconds if very high resolving or separation powers are to be achieved. The repetition rate for this whole cycle lies thus between a few tens of Hz and one kHz. Re-trapping as well as mass measurement mode have been operated at 50 Hz for the measurements of this work.

4.2.3 Electrode Potentials

In the tables 4.1 and 4.2 below, the operational voltages of the API and beam preparation system can be found. These are typical values optimized for maximum ion transmission. Of course, the AC voltages of the RFQs had to be adjusted specifically according to the ion of interest and are exemplarily denoted for the case of mass 195 u, which is the nominal mass of protonated caffeine and was widely used throughout this work. During ion extraction, the trap apertures are supplied with ±367 V.

Table 4.3 shows values that have been simulated for the analyzer's TFS and NT mode. Those values were utilized as starting points for the operation of the MR-TOF-MS and have been manually optimized for each particular timing scheme. ISEG high voltage power supplies have been used to provide these electrodes with their respective target voltages. For the measurement of the mass resolving power and mass accuracy, dedicated highly stabilized power supplies were operated for the analyzer's cap electrodes and drift tube. The MagneTOF electron multiplier was operated at -2500 V throughout all measurements of this work.

Electrode Name	Voltage / V	Frequency / MHz
Ion Guide RF	190	1.38
Mass Filter RF	240	1.18
Cooler RF	195	1.37
Ion Trap RF	220	1.46

Table 4.1: RF voltages (peak amplitudes) and frequencies used for transmission and storage of mass 195 u. The mass filter is operated at a Mathieu parameter of $q_u = 0.7$, the other RFQs at about $q_u = 0.4$.

Electrode Name	Voltage / V
Capillary	15
Lens	150
Skimmer	14
Ion Guide 1	14
Ion Guide 2	13
Aperture	12
Aperture	9
Brubaker Lens 1	10
Mass Filter	10
Brubaker Lens 2	10
Aperture	11
Cooler 1	8
Cooler 2	6
Pre-Trap	1
Trap Aperture 1	25
Ion Trap	0
Trap Aperture 2	25

Table 4.2: Experimental API and beam preparation system voltages. Here, the voltages applied to the trap apertures during ion storage are listed. For ion injection into the analyzer, the trap apertures were supplied with ±367 V, resulting in an electric field strength of about 78 V/mm on the optical-axis of the ion trap. The relative energy spread of the ions $\delta = \Delta K / K$ amounts to 0.014.

Electrode Name	TFS Voltage / V	NT Voltage / V
Steerer	-2500	-2500
Injection Lens	-4776	-4776
E1	232.3	414.7
E2	-85	-85
E3	-445	-869.1
E4	-3221.1	-4554.4
E5	-1300	-1300
E6	-3221.1	-4554.4
E7	-445	-869.1
E8	-85	-85
E9	232.3	414.7

Table 4.3: Analyzer voltages optimized in simulations. These values were used as starting points for optimization of the instrument's voltages.

4.2.4 Data Acquisition

For exact time-of-flight determination an analog-to-digital converter (ADC) as well as a time-to-digital converter (TDC) were used.

Notably, the ADC and TDC were operated at the same time for data acquisition (DAQ) of the MR-TOF-MS. The signals provided by the MagneTOF were split and delivered to both signal converters. The data acquisition of the ADC as well as of the TDC was handled by the MAc software simultaneously, giving the important advantage of processing signals of high and low intensity within the same spectrum.

Since high ion rates lead to dead time effects in the data acquisition of the TDC, a Signal Recovery FastFlight2 ADC was utilized for high intensities. During the first few minutes after a new nESI sample had been prepared, high ion currents were often used to identify peaks of interest and to adjust the analyzer timings accordingly.

Upon need, the ion rate could then be manually reduced by tuning the API's skimmer voltage. This was for example done whenever space charge effects had to be avoided during the measurement. In this case, the time-of-flight spectra recorded by a Fast ComTec MC6SA TDC have been used for data evaluation.

5 Performance Characterization

The instrument was enhanced, and its performance and capabilities were extended in many aspects (see section 4.1). Hence, characterization measurements have been carried out, and the results are presented in this chapter.

5.1 Mass Range

The mass range is an important performance figure for practical application of the MR-TOF-MS. It is especially interesting, since the MR-TOF-MS can be used in broadband mode with medium mass resolving powers as well as in high-resolution mode with a limited mass range.

The theoretical description of the mass range of the MR-TOF-MS can be found in section 2.4.4. The unambiguous mass range is limited by the premise that all ions recorded in the mass spectrum undergo the same number of turns in the time-of-flight analyzer. An additional restriction is imposed by the pulsing of the exit mirror electrodes that is performed during the switching of modes of operation (OP, TFS, NT). Ions that experience a change of electric fields gain or lose energy and thus their original flight path and time-of-flight will be distorted.

For the MR-TOF-MS two different cases have to be discussed. If the ions' mass-to-charge ratio is measured after one turn only, the second mirror electrodes are pulsed directly from TFS to OP mode. For higher number of turns, the second mirror will always be switched from TFS to NT mode after one turn at first and then from NT to OP mode after an additional number of turns N_a in NT mode.

To calculate the mass range for both cases, the ratios λ_{inj} and λ_{mir} have been obtained by time-of-flight determination in simulations for all three voltage switching scenarios. The transition from injection to mirror region was considered to be at the position where switching the voltages from one mode to another lead to a change of one volt in the electric potential. The simulations have been carried out with the ion and electron optics simulator SIMION [Scientific Instrument Services, Inc., 2012]. The results of the simulations can be found in table 5.1.

Voltage Transition	λ_{inj}	λ_{mir}
(i): TFS $\rightarrow$ OP	0.465	0.195
(ii): TFS $\rightarrow$ NT	0.414	0.295
(iii): NT $\rightarrow$ OP	0.506	0.165

Table 5.1: Calculated values for λ_{inj} and λ_{mir} for the three different scenarios of switching the second mirror's voltages.

For one turn in TFS mode, the theoretical mass range $(m/Q)_{max}/(m/Q)_{min}$ can thus be calculated to be 4.9. As discussed in section 3.1.2 and also shown in measurements [Lippert, 2012a], the mass range is limited to about 4 by the ion transport from the pre-trap to the RF ion trap, but this limit can be quite simply extended to cover the mass range of one turn in TFS mode (i.e. $(m/Q)_{max}/(m/Q)_{min}$ = 4.9) by adjusting the voltages of the trap system.

For higher number of turns, the switching from NT to OP mode (case (iii)) is the restricting factor when it comes to the mass range of the analyzer, and the voltage transition from TFS to NT mode after the first turn can be neglected for the calculation in this case. Figure 5.1 shows the mass range in dependence of the number of turns the ions travel in the time-of-flight analyzer.
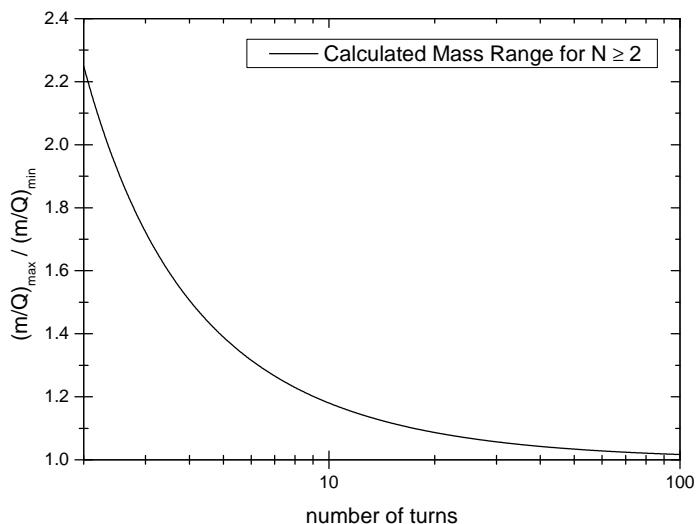
Figure 5.1: The calculated mass range from 2 to 100 number of turns. The mass range will be restricted to isobaric ions in the limit of very high turn numbers. For 1 turn, the mass range $(m/Q)_{max}/(m/Q)_{min}$ of the analyzer is 4.9.

Although the unambiguous mass range which can be simultaneously measured is limited, one can extend the mass range by operating the analyzer in a so-

called scan mode. In this mode, the mass of interest is automatically changed by a small amount every time a certain number of spectra has been recorded. Thereby, a much larger range of masses can be measured quasi-simultaneously. If the particular mass spectrum is not too complex, it is possible to mitigate the restriction of having all ions fly the same number of turns, and perform a mass calibration with different turn numbers [Ebert, 2016].

5.2 Mass Filter Operation

The RFQ mass filter of the MR-TOF-MS reduces the total ion load in the beam preparation system and mass analyzer, and can serve as the first stage of mass separation in MS^n experiments. In the following, caffeine and crude oil samples have been used to illustrate its working principle.

Figures 5.2 and 5.3 show mass spectra of a caffeine sample without and with the operation of the RFQ as a mass filter. For the measurement a sample of caffeine with 10^{-6} mol/l concentration in a H_2O/MeOH (1/1) solution with 0.1% formic acid was used, and the analyzer was operated in 1 turn TFS and 1 turn NT mode. The RFQ mass filter was set to $(a_u, q_u) = (0, 0.7)$ for the spectrum in figure 5.2, and to $(a_u, q_u) = (0.22, 0.7)$ for the mass spectrum in figure 5.3; both pairs of Mathieu parameters were calculated with respect to the mass of protonated caffeine at around 195 u. For the mass spectrum in figure 5.3, the mass filter was operated at a mass resolving power of about 20 with full transmission. The mass lines that can be seen in addition to the mass line of the main peak are either caused by dissociation or charge-exchange in the RF ion trap.
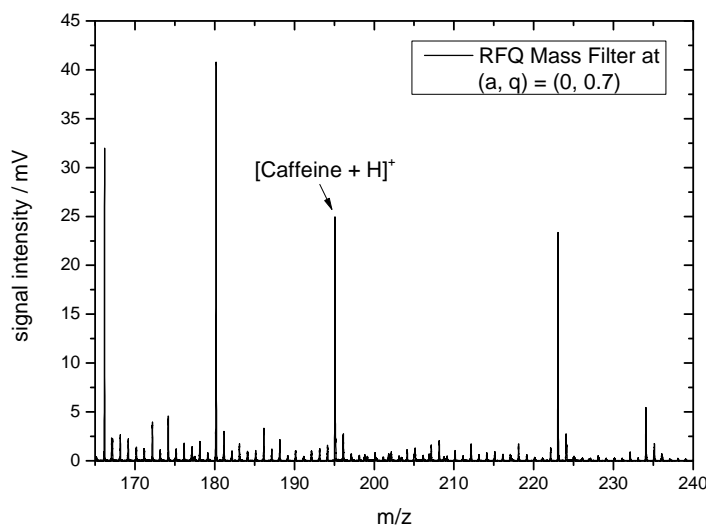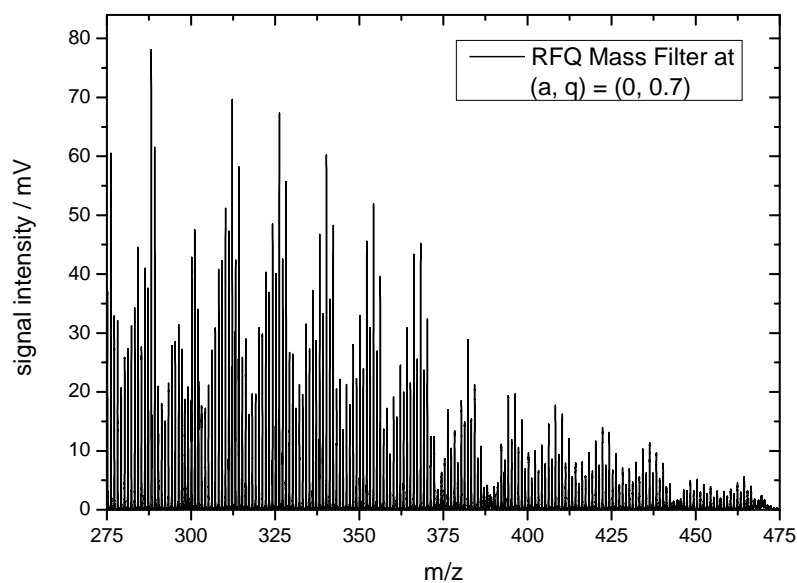

Figure 5.2: Spectrum of a caffeine sample with the RFQ mass filter operated at $(a_u, q_u) = (0, 0.7)$ for mass 195 u.
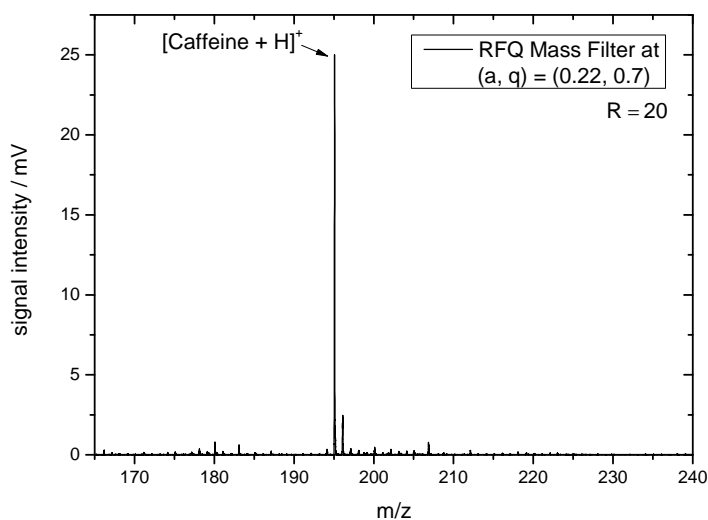
Figure 5.3: Spectrum of a caffeine sample with the RFQ mass filter operated at $(a_u, q_u) = (0.22, 0.7)$ for mass 195 u, i.e. near the apex of the stability diagram.

As another example, crude oil mass spectra are presented in figures 5.4 and 5.5. The sample contained 250 ppm crude oil in a toluene/MeOH (1/1) solution [Schrader, 2015]. In spectrum 5.5, the mass filter was operated at $(a_u, q_u) = (0.2, 0.7)$ for mass 337 u, which resulted in the transmission of a mass window of about 50 u around mass 350 u. As for the caffeine spectra, the analyzer was set to 1 turn in TFS and 1 turn in NT mode.

With the mass filter, the range of masses can be specifically selected such that only ions that are in the mass range of the analyzer (compare with fig. 5.1) are transmitted to the subsequent stages of the MR-TOF-MS. This reduces the ion load and thus decreases possible space charge effects in the ion trap and analyzer. More importantly, ambiguities in the mass spectrum caused by ions with different turn numbers can be avoided, which is crucial for the measurement of samples that provide complex spectra and if high turn numbers are applied.

Although ion storage in the RF ion trap may lead to the creation of additional ions due to dissociation or charge-exchange processes, remaining unwanted ion species can be removed from the mass spectrum by utilizing the mass range selector, which is located in the drift tube of the analyzer. Hence, the operation of both, mass filter and mass range selector, is highly required for the unambiguous identification of ions of interest in high-resolution mass measurements.

58

Figure 5.4: Spectrum of a crude oil sample with the RFQ mass filter operated at $(a_u,\, q_u) = (0,\, 0.7)$ for mass 337 u.
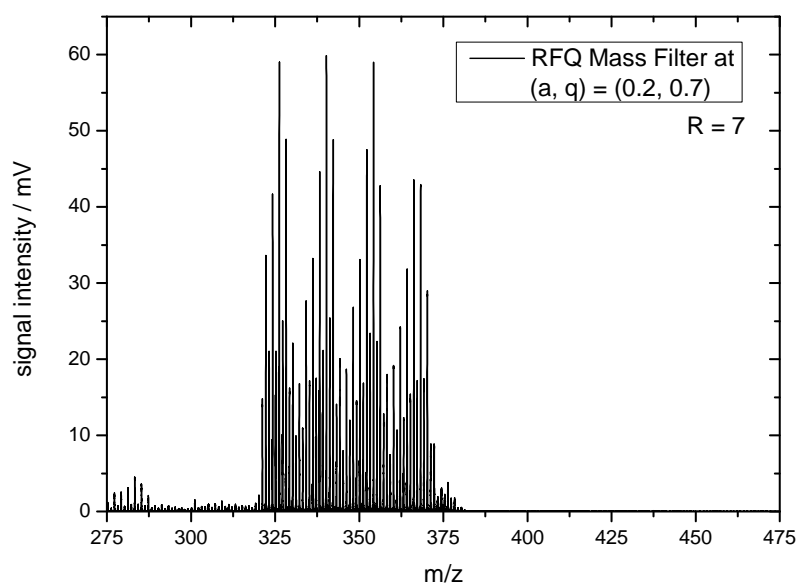
Figure 5.5: Spectrum of a crude oil sample with the RFQ mass filter operated at $(a_u,\, q_u) = (0.2,\, 0.7)$ for mass 337 u. About 50 mass lines between 325 u and 375 u are cut out from the mass spectrum presented above (fig. 5.4). The lower masses are fragments created by dissociation processes during storage in the RF ion trap.

5.3 Analyzer Transmission

On condition that the injection of ions from the RF ion trap into the analyzer is optimized, the transmission efficiency in the analyzer is predominantly determined by losses due to collisions with residual gas. Without additional buffer gas in the trap region, the pressure in the analyzer amounts to $6 \cdot 10^{-8}$ mbar. The analyzer pressure rises to about $3 \cdot 10^{-7}$ mbar, if the pressure of N_2 in the beam preparation system is regulated to $1.25 \cdot 10^{-4}$ mbar, which was the typical pressure value that was used during the measurements of this work. Nitrogen is used as buffer gas for the operation of the MR-TOF-MS, since it provides shorter cooling times and higher collision energies in dissociation processes than helium, for example.

The transmission efficiency $\mathcal{E}_{Analyzer}$ for a pressure of $3 \cdot 10^{-7}$ mbar in the analyzer has been measured with caffeine in dependence of the turn number, and is depicted in figure 5.6. This measurement was used to correct for collisional losses in the space charge as well as in the re-trapping efficiency measurements. For a certain amount of detected ions $N_{detected}$, the total (i.e. the initial) ion number N_{total} could then be estimated with the following calculation:

$$N_{total} = \frac{N_{detected}}{\mathcal{E}_{Analyzer}} \qquad (5.1)$$
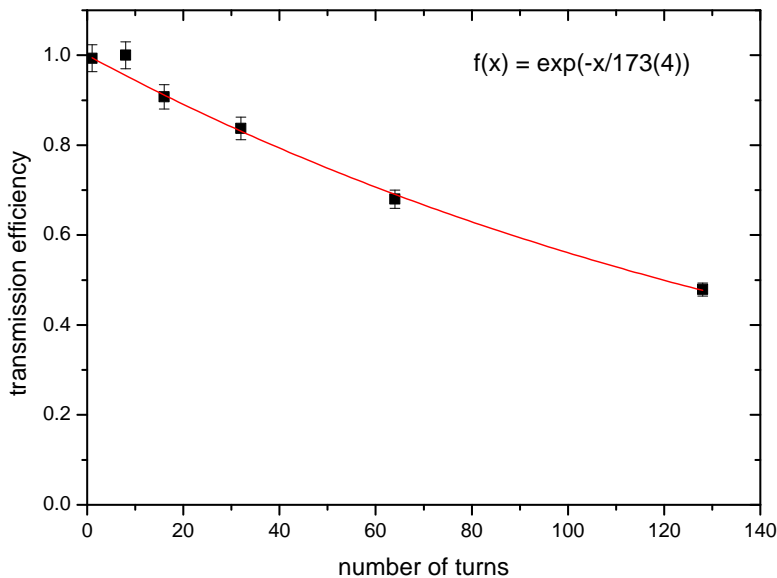
Figure 5.6: Transmission efficiency in dependence of turn number for a pressure of $3 \cdot 10^{-7}$ mbar in the analyzer. This measurement was used to correct the number of ions for collisional losses in the analyzer.

5.4 Linear Dynamic Range

The linear dynamic range of the MR-TOF-MS was measured with different concentrations of the amino acid arginine in a H_2O/MeOH (1/1) solution with 0.1% formic acid. The concentrations that were used range from 10^{-4} mol/l down to 10^{-9} mol/l.

The response of the instrument was measured by determining the signal-to-noise ratio in the mass window from 174 u to 200 u (1 turn in TFS and 8 turns in NT mode for the ions of interest). The total area of protonated arginine and its isotopes was divided by the area of all mass lines that were created in addition to those of arginine. A typical mass spectrum can be seen in figure 5.7. Each spectrum was recorded with an ADC and summed up over a time period of 2.5 minutes.

In figure 5.8 the measured linear dynamic range of the instrument is shown. The MR-TOF-MS shows a linear response to the analyte concentration over a range of 5 orders of magnitude, allowing for the quantitation of samples with concentrations ranging from 10^{-4} mol/l to 10^{-9} mol/l. The upper concentration limit was imposed by the ADC's restriction regarding the amplitude of the input signal, the lower limit by the analyte's intensity relative to the chemical noise of the particular spectrum.
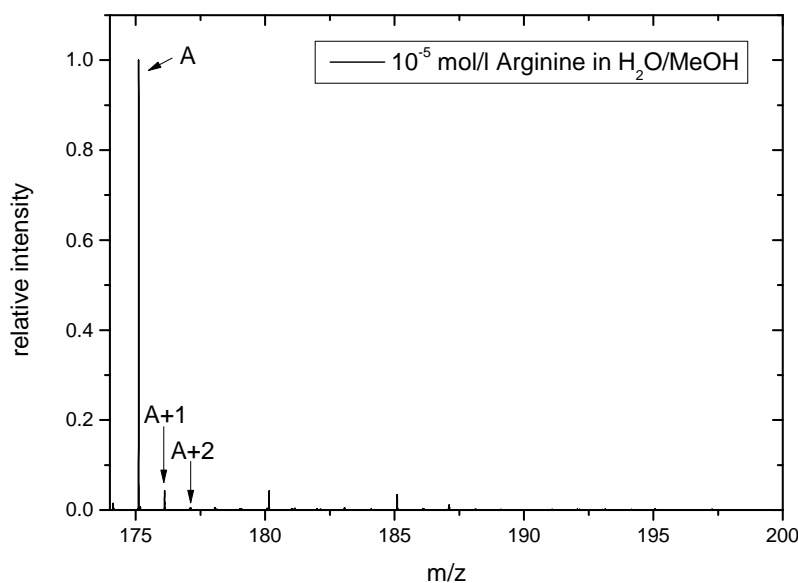
Figure 5.7: Mass spectrum of a sample containing 10^{-5} mol/l arginine. The mass window from 174 u to 200 u was used to determine the signal-to-noise ratio for each concentration. Isotopes of protonated arginine at mass 175 u, 176 u and 177 u are indicated.

$f(x) = 1.1(3)E4 * x + 0.0011(5)$
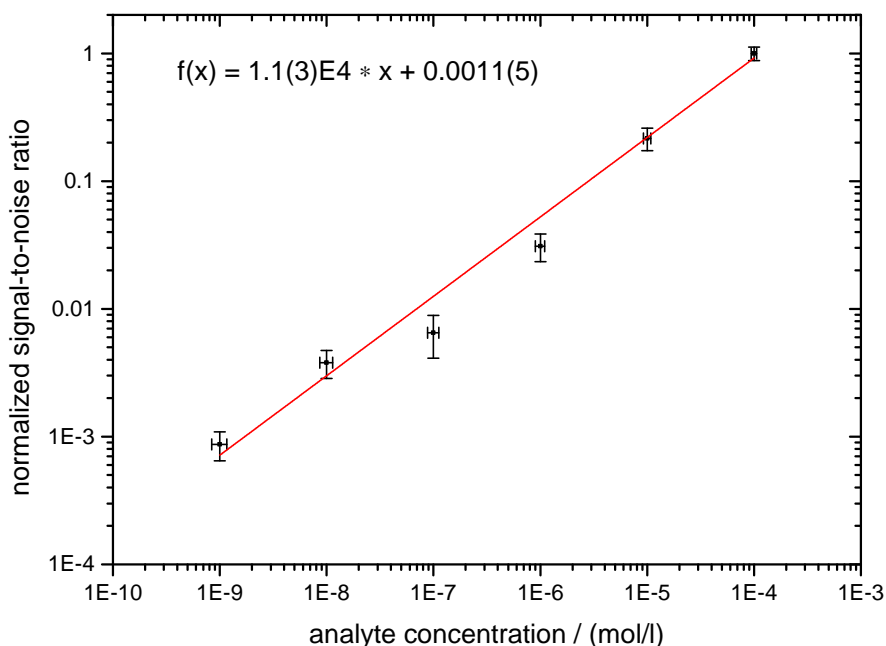
Figure 5.8: The investigated dynamic range of the MR-TOF-MS is shown. The instrument responds linearly to over 5 orders of magnitudes of arginine concentration. The signal-to-noise ratio of each measurement is normalized relative to the ratio that was measured with an analyte concentration of 10^{-4} mol/l. Since the parameters of the PID controller of the capillary heating had not been optimized, the temperature of the API capillary was not constant during the experiment. Thus, the measurements with a concentration of 10^{-6} mol/l and 10^{-7} mol/l yielded comparatively low statistics and may have been affected by temperature-dependent changes in signal-to-noise ratio.

Additionally, an analysis of the dynamic range of the analyzer and detector system has been performed by utilizing the isotope ratios of caffeine. In figure 5.9 a mass spectrum of caffeine with 10^{-3} mol/l concentration in solution is shown. This spectrum was recorded after a total number of 49 turns in the time-of-flight analyzer, resulting in a mass resolving power of about 45,000. As one can see, the first four isotopic mass lines can be clearly identified in the spectrum, whereas the mass line of the isotope at mass 199 u is covered by chemical noise. The experimentally determined isotope ratios as well as the theoretical values can be found in table 5.2, and are in general agreement with each other.

The results of this measurement illustrate the possibility to identify and quantify signals that differ almost 4 orders of magnitude in intensity within the same mass spectrum (compare with fig. 5.9).
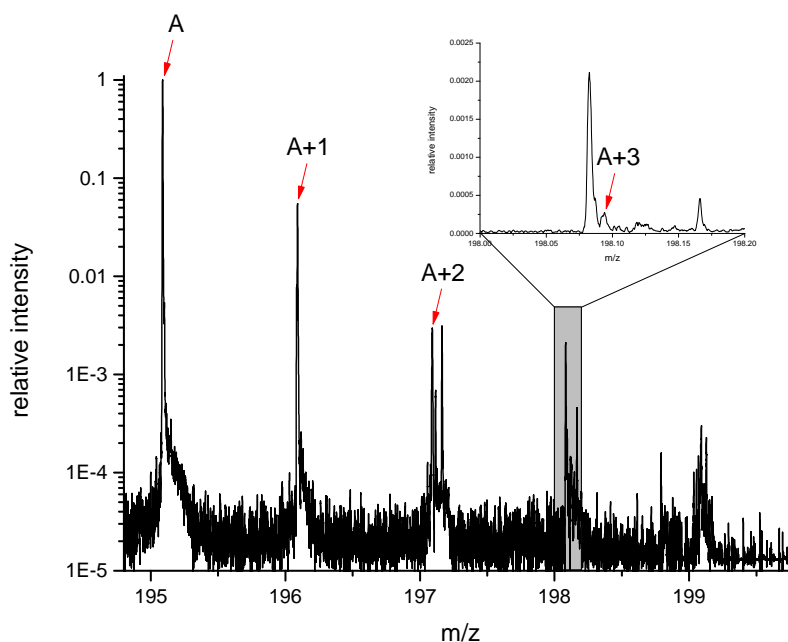
Figure 5.9: Mass spectrum containing the first five isotopes of protonated caffeine. The isotopes in the mass range from 195 u up to 198 u can be clearly identified and have been used to determine the relative abundances of caffeine isotopes.

A	Experiment	Theory	Relative Deviation
195	0.93(3)	0.90	0.03
196	0.060(5)	0.095	-0.37
197	0.005(1)	0.008	-0.38
198	0.0003(3)	0.0004	-0.25

Table 5.2: Experimental and theoretical values for the relative abundances of caffeine isotopes. The theoretical values have been calculated with the spectral isotopic distribution simulator IsoPro [Senko, 2009]. The errors comprise statistical uncertainties, but do not take into account systematic effects such as isobaric contaminations, for instance.

5.5 Detection Limit

The term "limit of detection" is not consistently defined in literature and strongly depends on the interpretation of data. To illustrate the detection limit of the MR-TOF-MS, two of the arginine spectra obtained by the measurements discussed in the previous section are presented in figure 5.10.
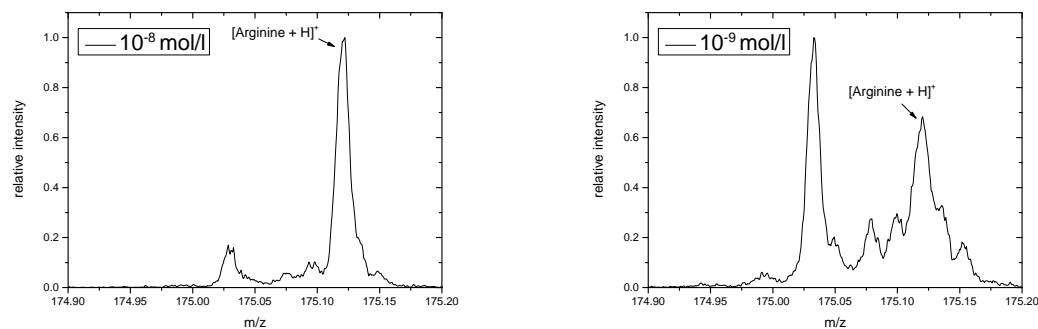
Figure 5.10: These two spectra illustrate the limit of detection of the instrument. Whereas protonated arginine is the dominant mass line in the spectrum on the left (10^{-8} mol/l), the analyte is only about three times the chemical noise (with respect to signal intensity) in the spectrum on the right (10^{-9} mol/l).

In both spectra, the amino acid can be clearly identified and quantified. The arginine peak in the spectrum recorded with a concentration of 10^{-9} mol/l is about three times the intensity of the chemical noise appearing in direct vicinity of the analyte. This provides a rough estimate for the instrument's limit of detection, which is then reached at a concentration of 10^{-9} mol/l (corresponds to about 0.2 ng/ml) for this particular measurement.

The detection limit of the instrument specifically depends on the sample, the cleanliness of the instrument (capillary, beam preparation system) and even on the mass range that is used to determine the level of chemical noise. Further measurements have to be performed and elaborate steps of data analysis have to be introduced to allow for a more general statement about the detection limit of the MR-TOF-MS.

With the novel technique of ion re-trapping (see section 7.2) much lower detection limits can be reached by separating the ion of interest before mass analysis. Due to the high selectivity of this method, the intensity of chemical contaminants can be practically reduced to zero.

5.6 Mass Resolving Power

Mass resolving power is one of the key performance parameters of any mass spectrometer. So far, resolving powers of 300,000 have been achieved for ions from an internal ion source [Lang, 2016]. The corresponding measurements have been performed with $^{133}Cs^{+}$ ions with a flight time of about 18 ms and 769 turns.

In this work, the mass resolving power was investigated after the improvements described in section 4.1 with samples that were ionized by nanoelectrospray ionization and then guided into the MR-TOF-MS via its atmospheric pressure interface. For this, the two molecules hexamethoxyphosphazene and caffeine have been used as test cases. The turn numbers have been chosen such that high mass resolving powers as well as the simultaneous measurement of the molecules' isotopes for mass accuracy determination (see section 5.7) were possible.

In figure 5.11 a mass spectrum of protonated hexamethoxyphosphazene is presented. The molecule is part of an ESI tuning mix (for ion trap) from Agilent that was used for this experiment. The analyzer was set to a total of 171 turns (1 turn in TFS + 170 turns in NT mode), which resulted in a time-of-flight of about 6 ms for mass 322 u. The peak shape has a slight asymmetry on the right side of the peak. In this measurement, a mass resolving power of 170,000 was achieved.
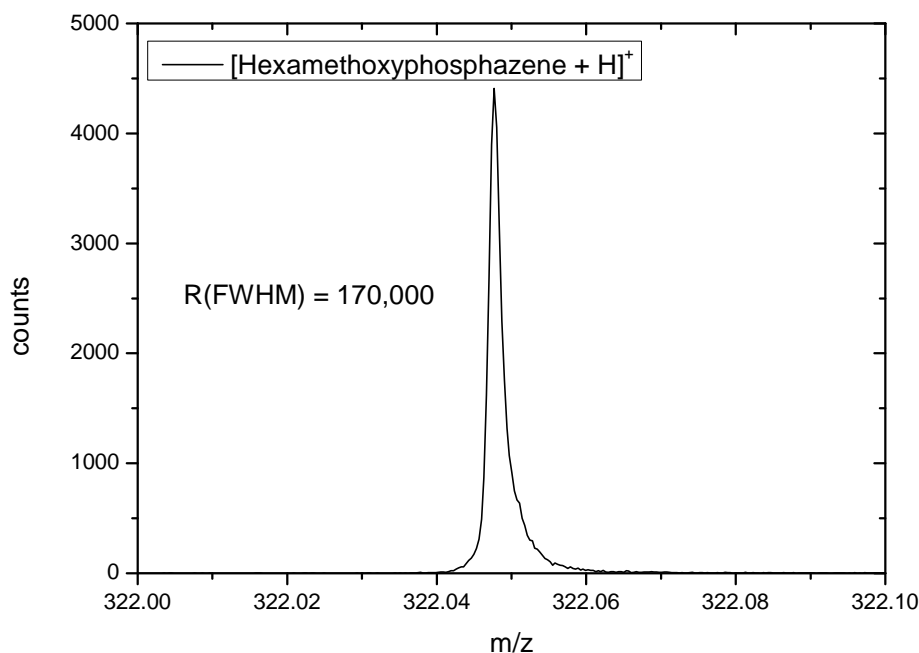
Figure 5.11: A mass resolving power of 170,000 was achieved for mass measurements with hexamethoxyphosphazene (171 turns). The full peak width at half of the peak height amounts to 1.9 mu.

As shown in figure 5.12, a mass resolving power of 215,000 was measured for protonated caffeine. The caffeine ions' flight time was about 5.5 ms, corresponding to 201 turns in the analyzer (1 turn in TFS + 200 turns NT mode).

These mass resolving powers have been reached within very short flight times, allowing to maximize the unambiguous mass range of the analyzer and to reduce

possible space charge effects. Under these conditions, the mass accuracy of the MR-TOF-MS has been investigated in detail.
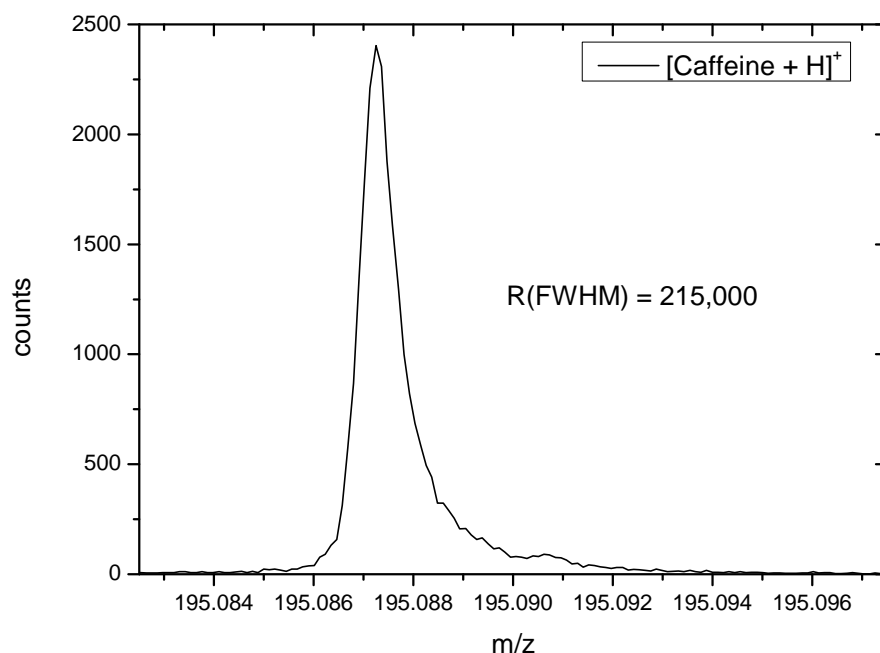
Figure 5.12: A mass resolving power of 215,000 was achieved for mass measurements with caffeine (201 turns). The peak width at half of the peak height amounts to 0.9 mu. The asymmetry on the right side of the peak indicates a non-perfect tuning of the analyzer.

5.7 Mass Accuracy

The mass accuracy of the MR-TOF-MS has been determined utilizing the isotopic patterns of hexamethoxyphosphazene and caffeine. The corresponding spectra have been recorded with the same settings as stated in the previous section. During these measurements, an ion rate of a few ions per cycle for the most abundant isotopes was set up, and the Fast ComTec MC6SA TDC was used for data acquisition.

In the following, the general steps of data analysis for the mass measurements will be briefly introduced. A more detailed description of the data analysis procedure can be found in [Ebert, 2016].

The mass calibration was performed on the basis of equation (2.22):

$$m(t) = a \frac{(t - t_0)^2}{(1 + N_a b)^2} \qquad (5.2)$$

After the constants a and t_0 had been determined by a 1 TFS turn only measurement with arginine and caffeine as calibrants, a time-resolved calibration was done within the MAc software on the basis of the calibrant masses of the isotope spectra of hexamethoxyphosphazene and caffeine.

In order to take into account the exact peak shape of the mass lines, the prominent mass of each spectrum was least-square fitted with an exponentially modified Gaussian (EMG) [S. Purushothaman et al., 2016] with the data analysis software Igor Pro [Wave Metrics, 2016].

The peak parameters of these EMG fits were then used to execute maximum likelihood fits to all mass lines with "R", a software environment for statistical computing.

Finally, a linear re-calibration was done to correct for the difference in peak position determined with MAc's time-resolved calibration (median) and the EMG fits (mean of the normal distribution), respectively. The fitted value for the mass of the isotope of interest m_{fit} was multiplied with the ratio of the calibrant's calculated to fitted (i.e. measured) mass value:

$$m_{exp} = m_{fit} \cdot \frac{m_{calib,theo}}{m_{calib,fit}} \qquad (5.3)$$

In figures 5.13 and 5.14, the mass spectra of hexamethoxyphosphazene and caffeine are shown, and the molecular formulas of the evaluated isotopes are denoted.
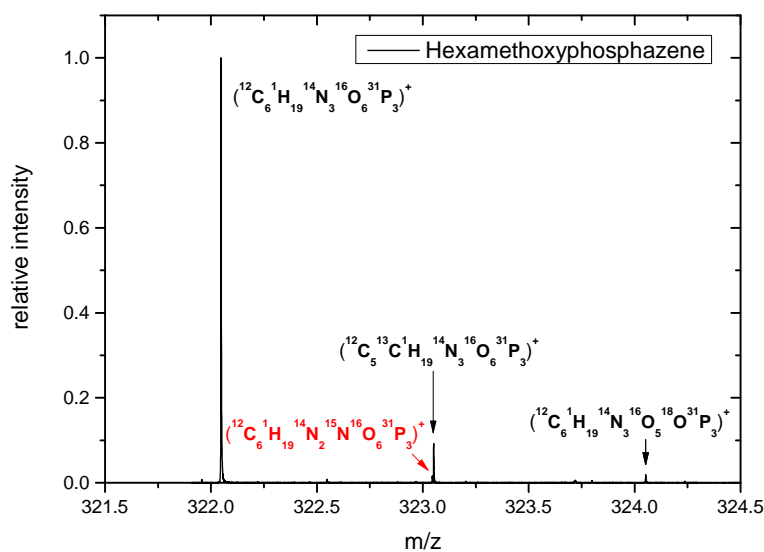
Figure 5.13: High-resolution hexamethoxyphosphazene mass spectrum. The molecular formulas of the experimentally determined masses are added to their respective mass lines (red: calibrant). The mass resolving power of this measurement amounts to 170,000 (FWHM).
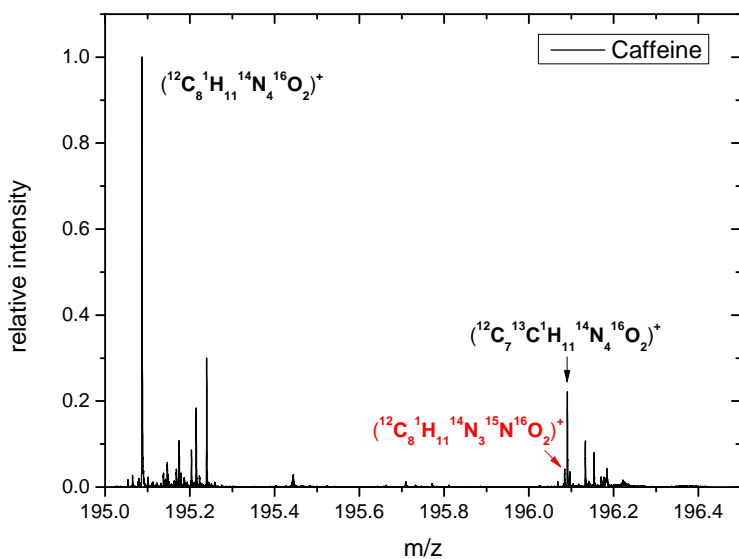
Figure 5.14: High-resolution mass spectrum of a sample containing caffeine. The molecular formulas of the experimentally determined masses are added to their respective mass lines (red: calibrant). The mass resolving power of this measurement is 215,000 (FWHM).

In tables 5.3 and 5.4 the corresponding results of the data analysis are presented. Theoretical values are the ions' calculated masses m_{theo} based on the NUBASE2012 atomic mass values [Audi et al., 2012] (neglecting molecular binding energies). The mass accuracy is listed in the last column of each table, and is defined as:

$$\frac{\delta m}{m} = \frac{m_{exp} - m_{theo}}{m_{theo}} \qquad (5.4)$$

Figures 5.15 and 5.16 depict the relative deviation of experimental from theoretical mass values graphically. The uncertainty σ_{mass} of the measurement was calculated as

$$\sigma_{mass} = \sqrt{\sigma_{fit}^2 + \sigma_{syst}^2}, \qquad (5.5)$$

where σ_{fit} is the uncertainty of the fit, and σ_{syst} the systematic uncertainty. The fit error was calculated as stated in [Ebert, 2016] and comprises the statistical, parametric and bias uncertainties involved in the process of performing EMG fits to the respective data sets.

Due to low ion rate (on average, 7 ions per cycle were simultaneously traversing the analyzer for the most abundant isotope), space charge effects do not contribute to the systematic uncertainty of the measurement. This was checked with simulations, where no significant deviation in time-of-flight was observed for simulations with and without space charge effects. Also, errors caused by switching of the analyzer's mirror electrodes can be excluded, since the pulsing of these electrodes was timed such that the ion trajectories were not affected. The remaining unknown systematic uncertainty was determined according to [Chen, 2008]. The corresponding calculation was done for two different sets of masses, one including ($\sigma_{syst,5} = 0.55$ ppm) and one omitting ($\sigma_{syst,4} = 0.18$ ppm) the hexamethoxyphosphazene isotope at mass 322 u, since the mass measurement of this isotope may be influenced by additional effects, like dead-time effects introduced by the TDC, for instance. As can be seen in figures 5.15 and 5.16, the total uncertainty σ_{mass} is mostly dominated by the unknown systematic uncertainty σ_{syst}.

Nevertheless, an excellent mass accuracy smaller than 1 ppm was achieved for each individual isotopic mass in both measurements. With flight times of about 6 ms for both molecules, an average absolute mass accuracy of 0.3 ppm was reached.

Isotope	m_{exp} / u	m_{theo} / u	$(\delta m/m)$ / ppm
$(^{12}C_6\,^1H_{19}\,^{14}N_3\,^{16}O_6\,^{31}P_3)^+$	322.047842(57)	322.048123	-0.87
$(^{12}C_6\,^1H_{19}\,^{14}N_2\,^{15}N\,^{16}O_6\,^{31}P_3)^+$	calibrant	323.045158	-
$(^{12}C_5\,^{13}C\,^1H_{19}\,^{14}N_3\,^{16}O_6\,^{31}P_3)^+$	323.05148(61)	323.051478	0.01
$(^{12}C_6\,^1H_{19}\,^{14}N_3\,^{16}O_5\,^{18}O\,^{31}P_3)^+$	324.052363(71)	324.052368	-0.02

Table 5.3: Experimental and theoretical mass values of evaluated hexam-
ethoxyphosphazene isotopes. The mass accuracy is stated in units
of ppm. The uncertainty of the experimental mass value determined
with $\sigma_{syst,4}$ is given.
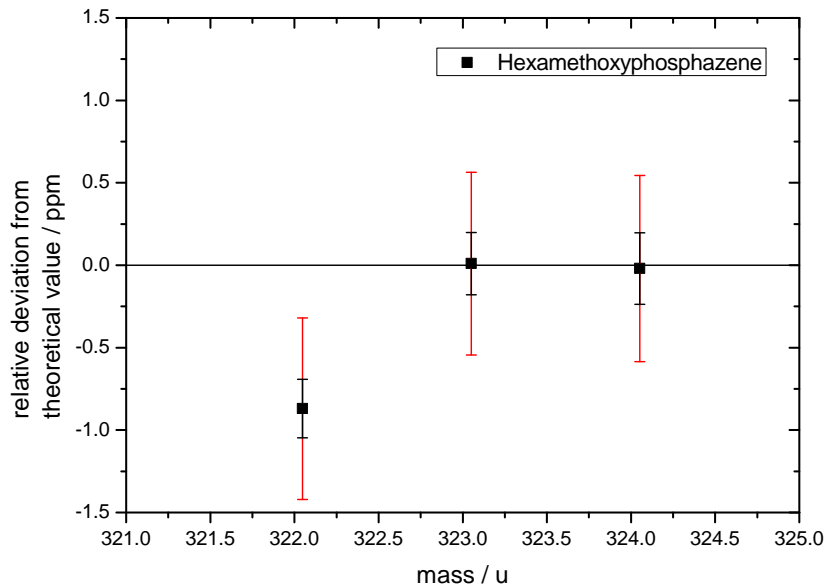
Figure 5.15: Relative deviation of the experimental from the theoretical mass
values for the hexamethoxyphosphazene isotopes. The isotopes at
mass 323 u and 324 u are in excellent agreement with the theoretical
mass values. For the calculation of the uncertainties of the mea-
surement, the unknown systematic uncertainty was determined with
(red) and without (black) the isotope of hexamethoxyphosphazene
at mass 322 u.

Isotope	m_{exp} / u	m_{theo} / u	$(\delta m/m)$ / ppm
$(^{12}C_8\ ^1H_{11}\ ^{14}N_4\ ^{16}O_2)^+$	195.087619(35)	195.087652	-0.17
$(^{12}C_8\ ^1H_{11}\ ^{14}N_3\ ^{15}N\ ^{16}O_2)^+$	calibrant	196.084687	-
$(^{12}C_7\ ^{13}C\ ^1H_{11}\ ^{14}N_4\ ^{16}O_2)^+$	196.091061(35)	196.091007	0.28

Table 5.4: Experimental and theoretical mass values of evaluated caffeine isotopes. The mass accuracy is stated in units of ppm. The uncertainty of the experimental mass value determined with $\sigma_{syst,4}$ is given.
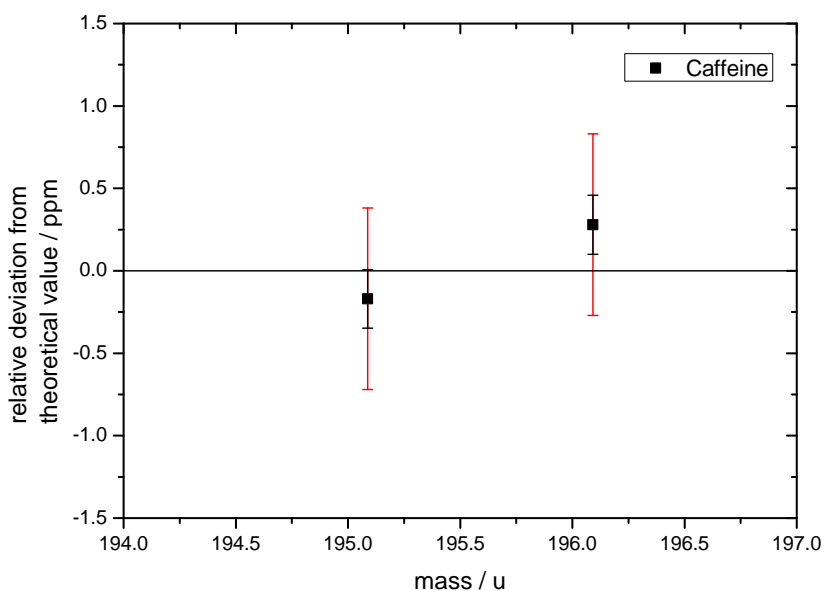
Figure 5.16: Relative deviation of the experimental from the theoretical mass values for the caffeine isotopes. As for hexamethoxyphosphazene, the caffeine isotopes at mass 195 u and 196 u are very well in agreement with the theoretical mass values. For the calculation of the uncertainties of the measurement, the unknown systematic uncertainty was determined with (red) and without (black) the isotope of hexamethoxyphosphazene at mass 322 u.

6 Investigation of Space Charge Effects

Previous studies have indicated an influence of signal intensity on the width of peaks in the time-of-flight spectrum [Lang, 2016]. This behavior is attributed to ion-ion interactions and present in all ion trap devices [Zajfman et al., 1997, Herlert et al., 2011, Grinfeld et al., 2014]. The mutual repulsion of ions imposes a limit on the maximum number of isobaric ions that can simultaneously fly in the analyzer without affecting the mass accuracy and mass resolving power of the MR-TOF-MS.

The spectrum in figure 6.1 illustrates the occurring effects. Two caffeine isotopes of different intensity exhibit different mass resolving powers, although they were measured within the exact same mass spectrum. The intense peak is much broader than expected due to the high ion rate.

In this chapter, these so-called space charge (SC) effects are investigated in detail with simulations and corresponding measurements, and methods to improve the space charge behavior of the instrument are presented.
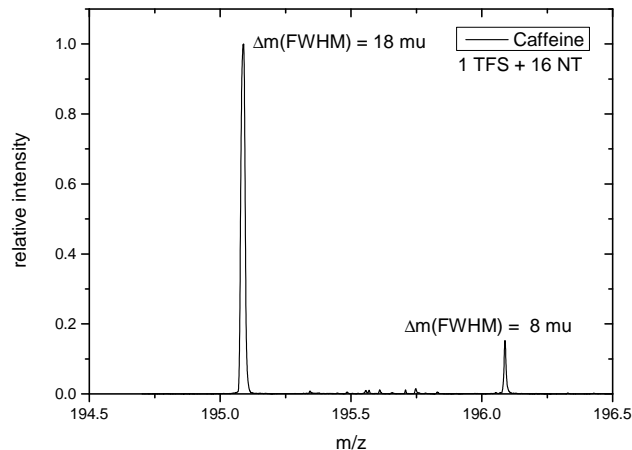
Figure 6.1: A measured caffeine spectrum containing two isotope peaks. The prominent isotope peak at mass 195 u has a FWHM of 18 mu, whereas for the much less intensive isotope at mass 196 u a FWHM of 8 mu is determined. The ion rates were 280 ± 40 respectively 24 ± 4 ions per cycle.

6.1 Simulation Setup

The simulations have been conducted with the ion and electron optics simulator SIMION [Scientific Instrument Services, Inc., 2012]. In SIMION, the ion trajectories are numerically calculated with the fourth-order Runge-Kutta method. The ions are assumed to travel in stationary electric potentials, which are generated by the surrounding electrodes. For the generation of these potentials, the Laplace equation is numerically solved with respect to the given boundary conditions. In figure 6.2 the SIMION model of the relevant part of the MR-TOF-MS is depicted.
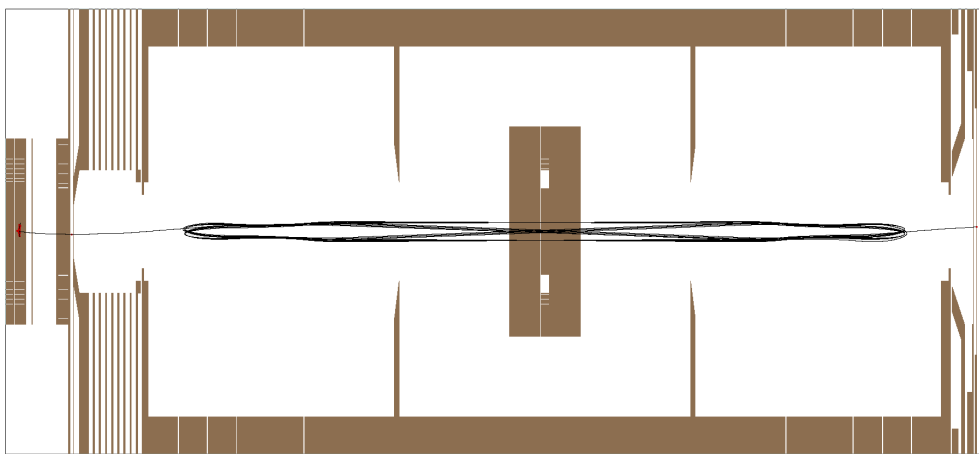
Figure 6.2: SIMION model of the instrument's ion trap and time-of-flight analyzer. The black lines illustrate a typical ion trajectory from the trap (left side) to the ion detector (right side). The aspect ratio is not preserved in this picture.

The size of time-steps is internally determined by the so-called trajectory quality (TQ) factor. Especially when simulating space charge effects, an adequate compromise between calculation accuracy and calculation time has to be found. The mutual interaction of N ions in an ion cloud leads to additional N^2 calculations per time-step. Hence, the right choice of the number of ions and TQ factor is crucial, since both parameters have a huge impact on the time frame of the simulation.

Obviously, a TQ factor can only be valid within a certain regime of combinations of turn numbers and total charge. If this regime is exceeded, a better TQ factor (i.e. smaller time-steps) has to be used to compensate for accumulating errors in the numerical calculations. This will result in more accurate space charge calculations, but also be more demanding in terms of simulation time.

Since charges do not only interact with each other, but also exert an influence on the electric field they propagate in, the Poisson equation would have to be solved with every time-step of the simulation. On the contrary, for the number of simulated charges and the spatial distribution of these charges inside the analyzer, this effect was assumed to be negligible for the purpose of saving simulation time.

As shown by extensive evaluations, the ions' time-of-flight and energy were indeed found to be conserved for the settings chosen for the simulations presented in this work [Otto et al., 2016]. In addition, an identical simulation setup (two ion species with a relative mass difference of 10^{-5}, 64 turns, analyzer of the MR-TOF-MS operated in nuclear physics experiments) has been simulated with SIMION as well as with a direct ion-to-ion Coulomb interaction algorithm [Yavor, 2016]. As one can see in figure 6.3, the two phase spaces agree very well with each other. These findings indicate the reliability and validity of the SIMION simulation results for the present study.

In every simulation, the ion ensembles were first brought to a state of equilibrium by collisions with a nitrogen buffer gas at a temperature of 300 K in the ion trap. Afterwards they were injected into the analyzer and the electrode voltages were switched in accordance to the timings used in experiment. In the end, the ions' parameters were recorded in a plane coinciding with the position of the ion detector.

The ion trap region was implemented with a resolution of 10 grid units per millimeter, whereas a higher resolution of 40 grid units per millimeter was realized for the time-of-flight analyzer. For each simulation, the ion cloud contained a total of $N = 250$ particles, holding a total charge Q which was always less or equal to the number of particles (250 particles with a total charge of 25 e corresponds to 25 ions, for example). Thereby, phase space distributions with the same statistics were produced for each individual run regardless of simulated charge.

The nominal mass of protonated caffeine (195 u) was used throughout all simulations, since many measurements with caffeine as ion of interest were performed during commissioning and characterization of the instrument.

As a figure of merit for the effects of space charge on the time-of-flight behavior of the ions, either the peak widths or the final time-energy phase space distributions are shown and discussed. The peak widths were always manually determined as full width at half maximum, since the peak shape changes from an ideal Gaussian shape to an almost rectangular shape for high signal intensities. In the time-energy plots, the final ion distribution as recorded on the detector is presented.
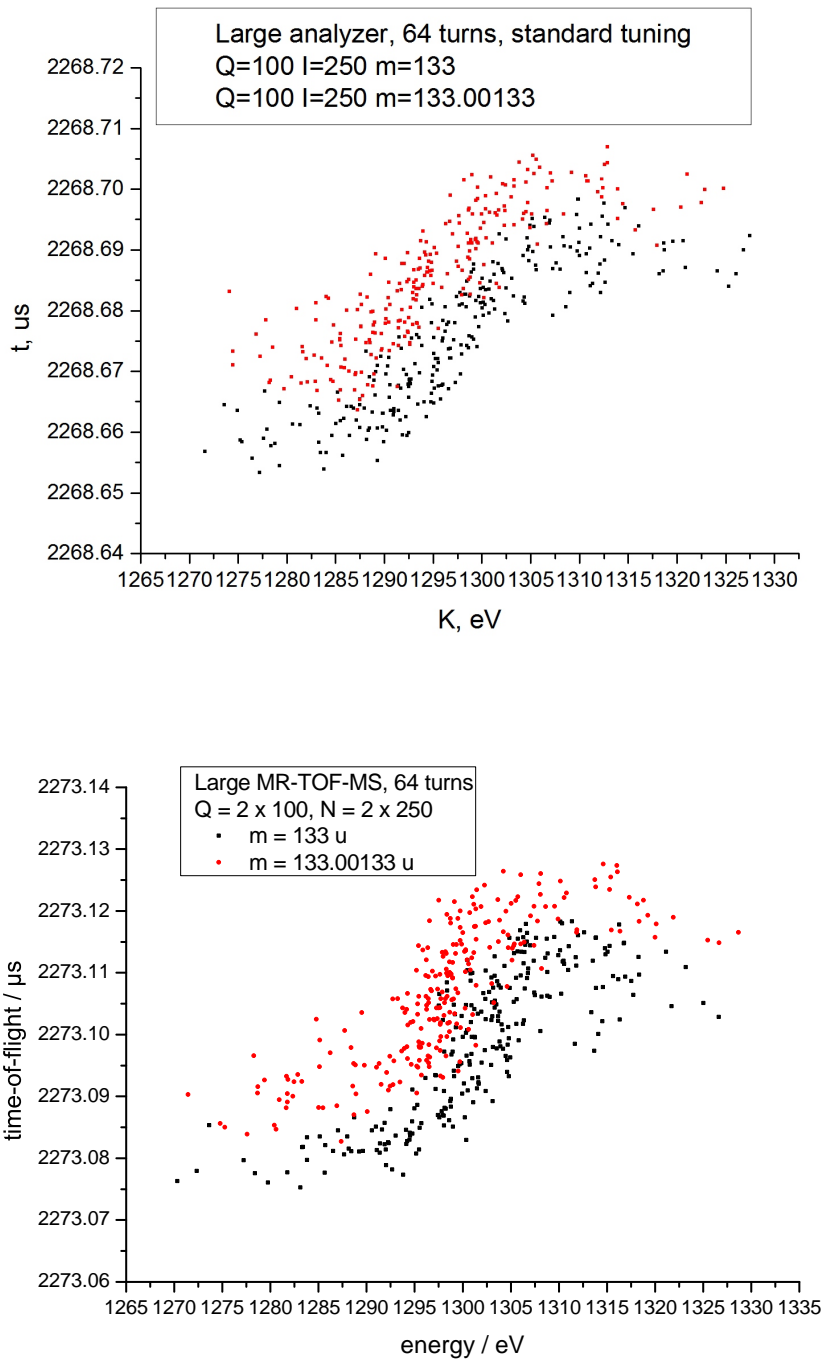
Figure 6.3: Comparison of phase spaces of two ion clouds which were simulated with a direct ion-to-ion Coulomb interaction algorithm (upper part, [Yavor, 2016]) and SIMION (lower part). The ions' flight time is plotted in dependence of their kinetic energy distribution. As one can see, the two simulations are in good agreement with each other, as both plots exhibit the same tilted time-energy phase spaces ($(T|\delta) \neq 0$) due to space charge effects. The difference in the ions' time-of-flight is caused by slightly different positions of ion detection.

6.2 Comparison of Simulation and Measurement Results

Various simulations and measurements have been carried out to investigate the effect of ion-ion interaction in the time-of-flight analyzer of the MR-TOF-MS. The analyzer was always operated in a 1 TFS turn + N_a normal turns mode. The number of normal turns was varied between 16, 32, 64 and 128 turns. For the highest turn number, flight times of about 3.6 ms and simulations times of a few days per data point were obtained. The number of ions per cycle was set to 0, 10, 25, 50, 100 and 250 in simulations, and up to approximately 375 in measurements. The ion number in measurements was calculated by dividing the total area of the peak by the mean area of a single ion signal (23 ± 3 pVs), which was determined by measuring the MagneTOF's pulse height distribution. Additionally, corrections with respect to transmission and detection efficiencies ($\mathcal{E}_{Grid} = 88\%$, $\mathcal{E}_{MagneTOF} = 80\%$), and ion losses due to collisions with residual gas in the analyzer (compare with 5.3) have been taken into account.

In figures 6.4, 6.5, 6.6 and 6.7 the measured peak widths are compared to simulation results. Since the number of ions was fixed in the simulations, only the FWHM values are assigned with error bars. In measurements, the FWHM could be determined very well because of high statistics. Here, the ion number calculations yield the largest uncertainties. Despite a minor divergence at highest ion numbers and 128 normal turns, measurements and simulations are in excellent agreement with each other.
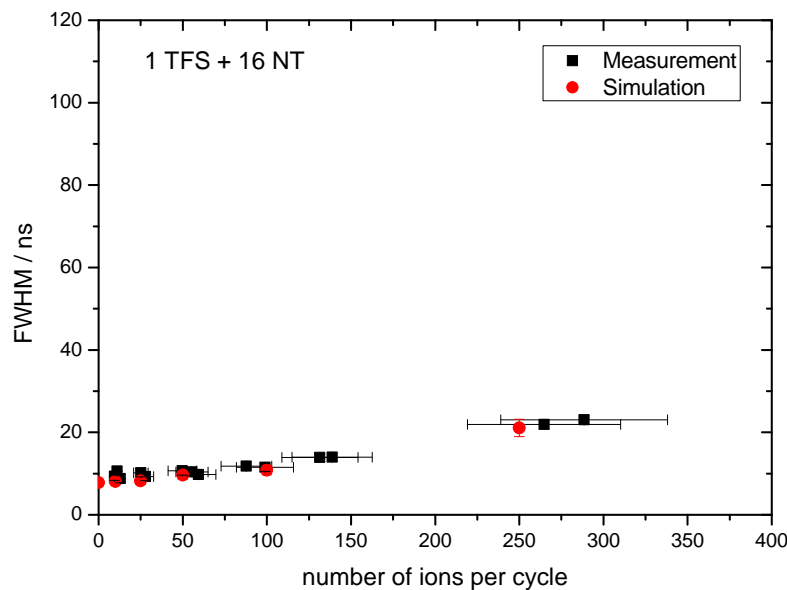
Figure 6.4: Results of space charge measurements and simulations for 16 normal turns. Simulation and measurement agree very well with each other.
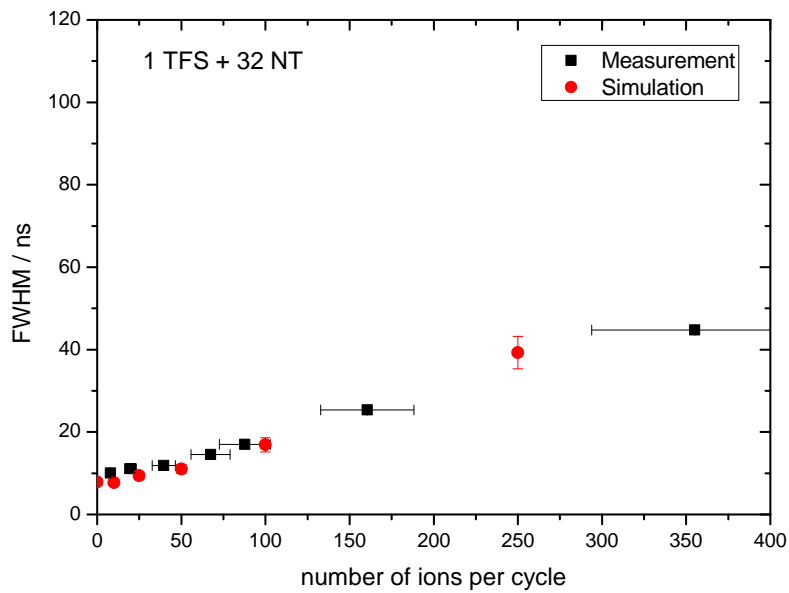
Figure 6.5: Results of space charge measurements and simulations for 32 normal turns. Here, the peak width increases twice as fast with the number of ions per cycle as for 16 NT.
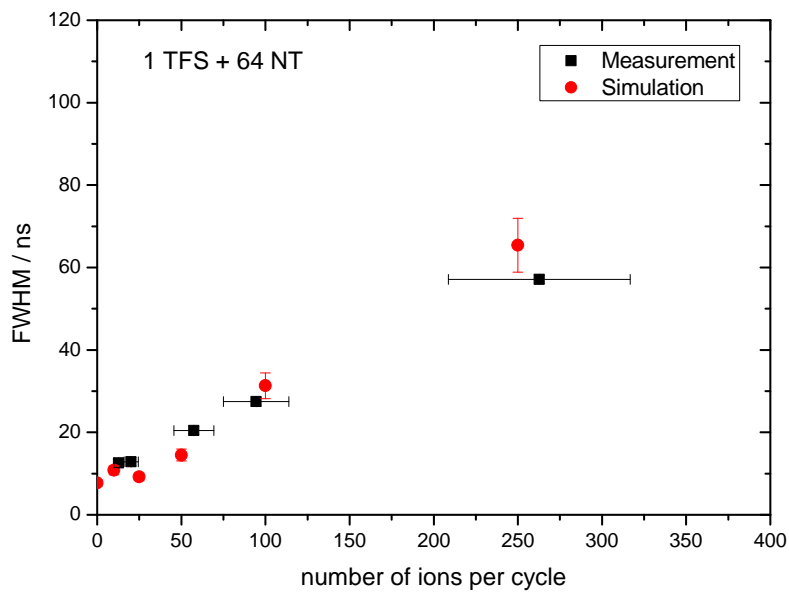
Figure 6.6: Results of space charge measurements and simulations for 64 normal turns.
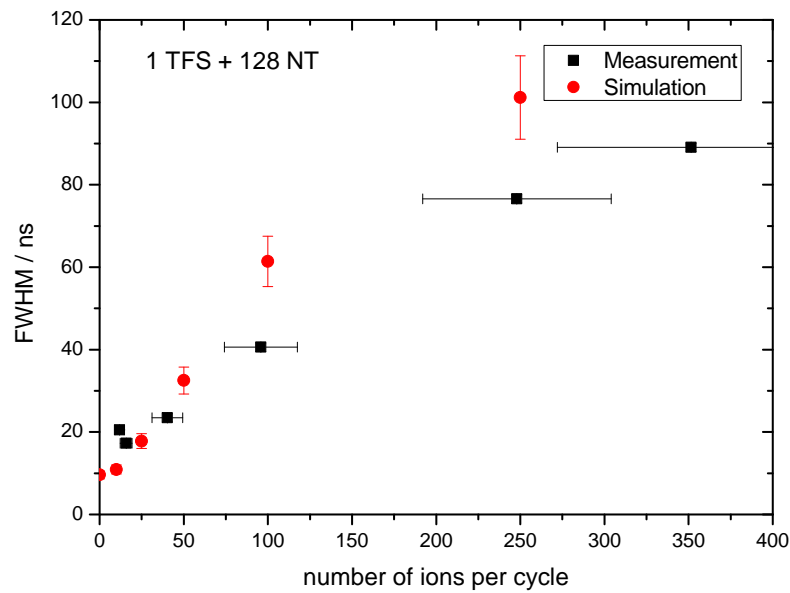
Figure 6.7: Results of space charge measurements and simulations for 128 normal turns. The peak widths start to diverge for high ion numbers. This may be attributed to numerical errors in simulation or to an overestimation of ion number in the measurement (collisional losses were fully compensated to match the initial number of ions in the RF ion trap). Additionally, the experimental tuning of the analyzer was not perfect during this measurement, as can be seen by the peak width in the case of low ion count.

Both, simulations and measurements, exhibit a nearly linear dependence of peak width on the number of ions and turn number. Whereas the initial peak width (≈ 8 ns) is more than doubled in the range from 0 to 250 ions for 16 normal turns, the peak width increases much faster for 128 NT, where it is doubled for 25 ions already.

6.3 Different Modes of Operation

For the measurements of this work, the analyzer was operated such that the time-focus shifting occurred at the beginning of the ions' flight path. This way, the (virtual) time-focus is placed on the ion detector position during all subsequent normal turns. Since peak-broadening is caused by ion-ion repulsion, long interaction times and dense ion distributions amplify space charge effects the most. With the time-focus being placed on the detector, the ion clouds will be very dense with long interaction times in the region of the second mirror of the analyzer. Therefore, it was of peculiar interest to investigate the occurrence of

space charge effects for different orders of TFS and NT mode, as this changes the position of time-focus during all normal turns and thus possibly the ions' space charge behavior.

Four different operation mode configurations have been simulated:

- TFS at the beginning of the ions' flight path (TFS | NT); this is referred to as "operational mode"

- TFS at the end of the ions' flight path (NT | TFS)

- Split TFS mode: half of TFS is performed at the beginning, the other half at the end of the ions' flight path (0.5 TFS | NT | 0.5 TFS)

- Omitting TFS by using different NT voltages in dependence of the number of turns to shift the position of time-focus gradually to the detector (NT only)

The same ion and turn numbers as in section 6.2 have been used for the simulations. Also, each run contained a total of 250 particles. For the NT only simulations, the voltages of the electrodes E1 and E9 had to be tuned such that the position of time-focus was placed on the detector (for simulations without space charge effects). This was done for each number of turns individually.

6.3.1 Peak Width

The graphs in figures 6.8 and 6.9 show exactly the same dependency of peak width on the simulated number of ions per cycle. It does not seem to matter whether the virtual time-focus is placed near the first (NT | TFS) or second mirror (TFS | NT) of the analyzer while operated in NT mode.

A completely different picture is drawn for the results of the 0.5 TFS | NT | 0.5 TFS mode calculations (see fig. 6.10). In this mode, the intermediate time-focus is placed in the middle of the analyzer. Space charge effects are present, but result in much smaller peak widths when compared to all other modes. Also, the general trend of the graphs is different. For 16 and 32 normal turns the peak widths get larger with an increasing number of ions. Up to a certain amount, the same is true for the simulations with 64 and 128 normal turns. But for more than 100 ions per cycle, the peak widths start to get smaller again. This process can only be sufficiently explained by looking at the corresponding phase space plots, which are discussed in section 6.3.2.
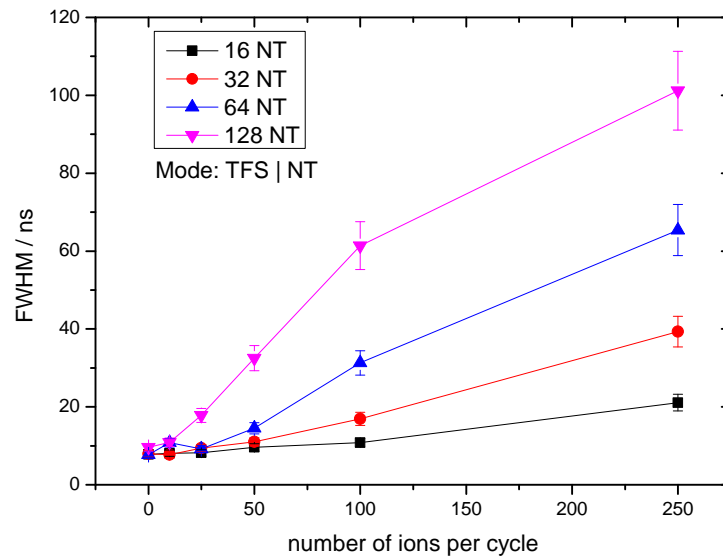
Figure 6.8: Space charge simulations for TFS │ NT mode; the peak width is plotted as a function of the number of ions per cycle. This is the mode the MR-TOF-MS was operated in for the measurements of this work. The simulation results are the same as in the previous section, where they have been compared to measurements.
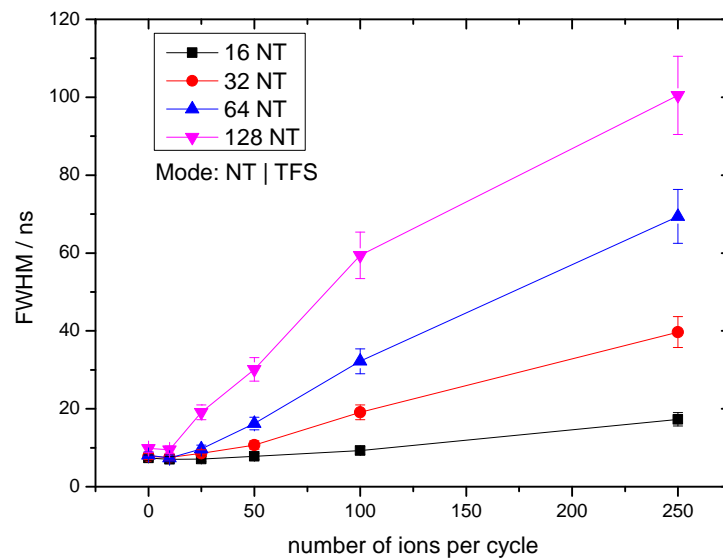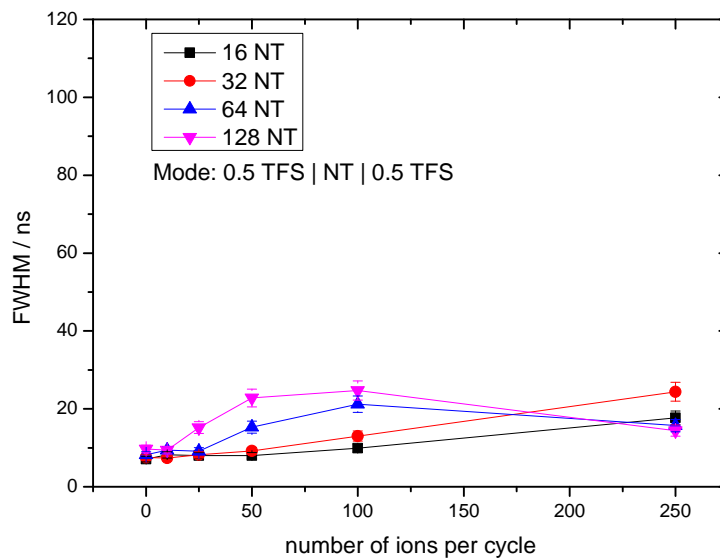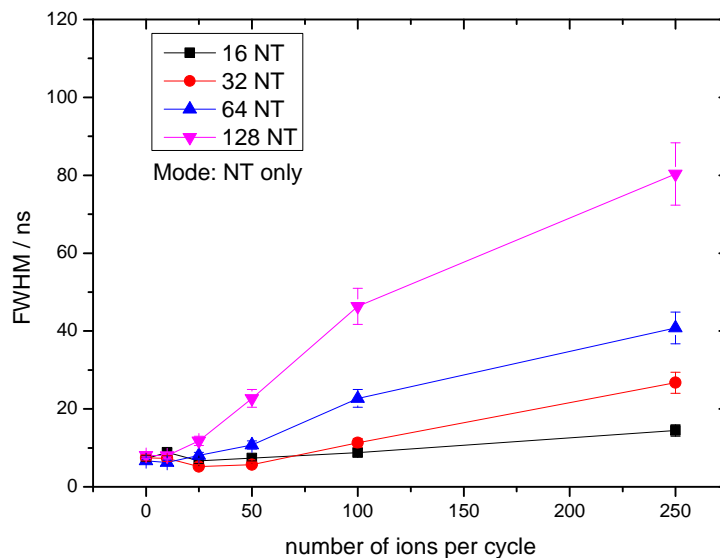

Figure 6.9: Space charge simulations for NT │ TFS mode; the peak width is plotted as a function of the number of ions per cycle. Here, the orders of time-focus shifting and normal turns have been interchanged. The graphs look almost completely identical to the ones presented in fig. 6.8.

Figure 6.10: Space charge simulations for 0.5 TFS │ NT │ 0.5 TFS mode; the peak width is plotted as a function of the number of ions per cycle. Splitting up the TFS puts the position of time-focus in the middle of the analyzer. The peak widths seem to be capped at about 25 ns, regardless of turn and ion number.

Figure 6.11: Space charge simulations for NT only mode; the peak width is plotted as a function of the number of ions per cycle. With only one set of voltages that is used during all turns, the space charges effects seem to be less prominent compared to TFS │ NT and NT │ TFS mode.

Other closed path multiple-reflection time-of-flight mass spectrometers are operated with a single set of voltages after ion injection (see [Wolf et al., 2012], for instance). This operational mode was mimicked during the simulations depicted in figure 6.11. Here, the time-focus is gradually shifted through the analyzer with every turn and finally placed on the detector. The general space charge behavior coincides with the one for TFS $|$ NT and NT $|$ TFS mode, although it seems to be $20\% - 30\%$ less prominent.

6.3.2 Time-Energy Phase Space

Ideally, and without the presence of any space charge effects, the analyzer is tuned to provide an optimal time-focus on the detector. In that case, the ion's time-of-flight is independent of its initial energy in good approximation, i.e. the dependence of flight time on energy vanishes $((T|\delta) = 0 \quad \wedge \quad (T|\delta\delta) = 0)$. Hence, the ion distribution is aligned in parallel to the energy-axis in a time-energy phase space plot.

Under the influence of space charge, a totally different behavior is observed. For the operational mode of the analyzer (see fig. 6.12), the time-energy phase space distribution of ions starts to tilt and rotate with an increasing number of ions or turns. Additionally, some sort of cluster effect can be seen. This effect is referred to as self-bunching when the time-of-flight distribution of ions is discussed, as it suppresses deviations from the isochronous motion of ions in the analyzer [Grinfeld et al., 2014].
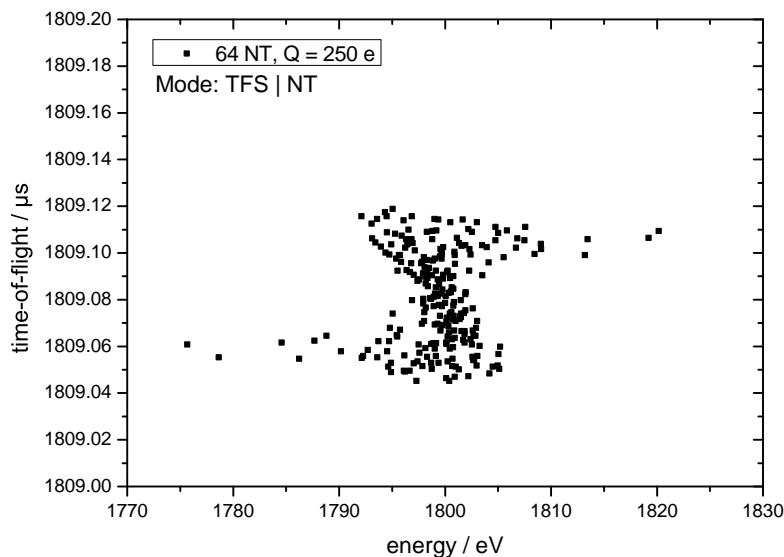
Figure 6.12: Phase space distribution of ions in the operational (TFS $|$ NT) mode with 250 ions after 64 normal turns. The ion distribution is rotated and starts to clump together in the center of the 2D plot.

Although the peak widths of the operational mode and the NT │ TFS mode were simulated to be almost identical, the NT │ TFS mode reveals a completely different phase space distribution (as can be seen in figure 6.13). Instead of being clumped together, the ion distribution is spread out and slightly inclined. By projecting this distribution onto the time axis of the plot, the agreement of both modes in terms of peak widths can be understood.
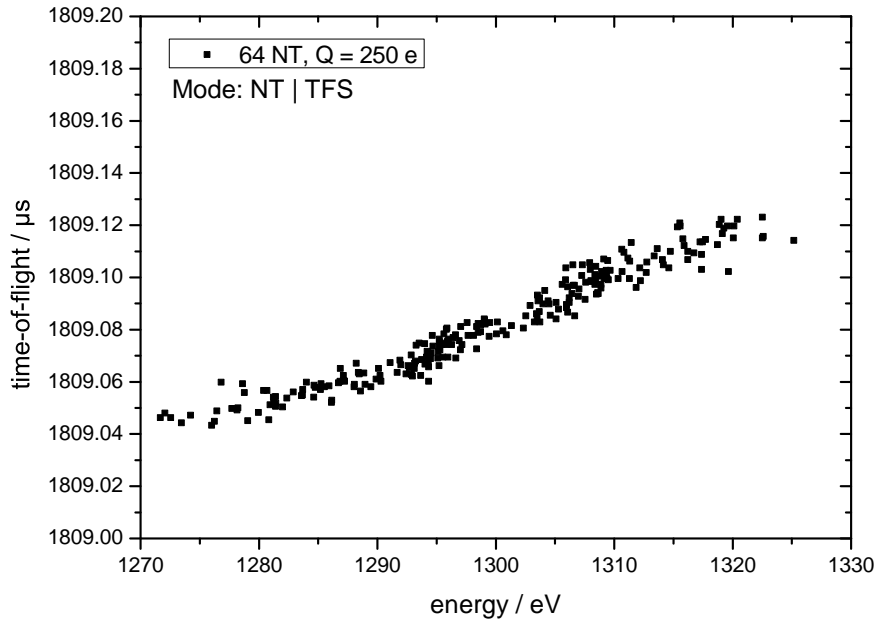

Figure 6.13: Phase space in the NT │ TFS mode with 250 ions after 64 normal turns. The distribution is spread out with a slight inclination. Nevertheless, its projection onto the time axis leads to peak widths identical to the ones observed in the operational mode (fig. 6.12).

In contrast to the two previous modes, the peak widths were found to be very small regardless of ion and turn number in the mode with an intermediate time-focus in the middle of the analyzer. This is explained by a very dominant self-bunching effect, which is exemplarily depicted in figure 6.14. The ions form a dense cluster in the center of the phase space plot, resulting in a compact peak width. This effect seems to get even stronger with an increasing number of ions or turns, as can be seen by the decreasing peak width for 64 and 128 turns, and ion numbers above 100 (fig. 6.10).

The phase space of the NT only mode is a bit of a mixture between the operational and the 0.5 TFS │ NT │ 0.5 mode. The ion distribution is rotated and clustered in the center of the plot (fig. 6.15).
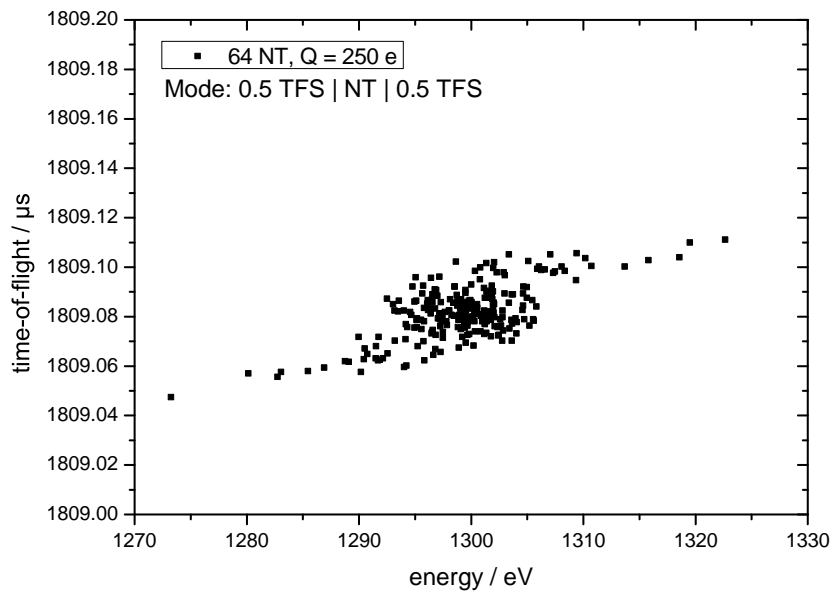
Figure 6.14: Phase space in the 0.5 TFS │ NT │ 0.5 TFS mode with 250 ions after 64 normal turns. Self-bunching is very prominent and explains the small peak widths which are presented for this mode of operation in the last section.
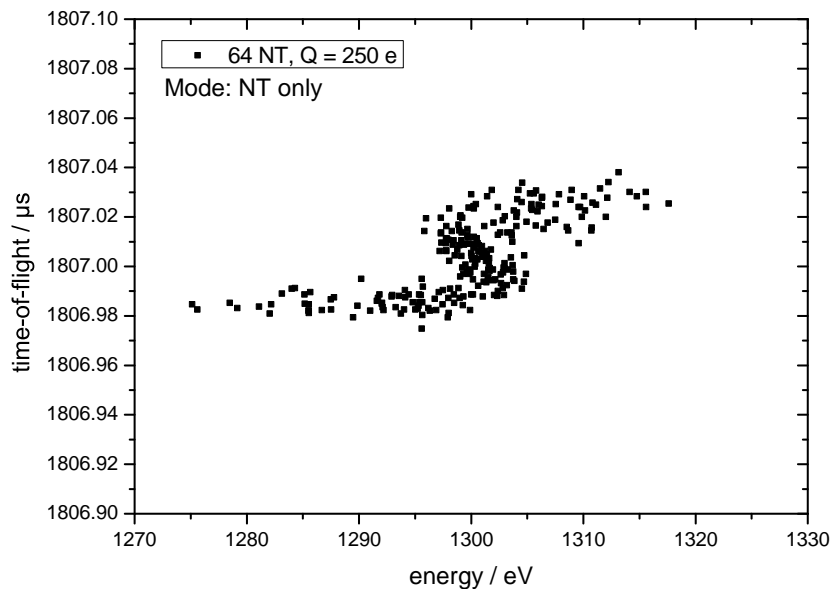

Figure 6.15: Phase space in the NT only mode with 250 ions after 65 normal turns. The phase space is very similar to the one depicted in figure 6.12. Due to the lack of a TFS turn, the total flight time is slightly different.

The simulation results are similar to the results of the work of [Grinfeld et al., 2014]. There it was found that the occurrence of self-bunching effects depends on whether the analyzer is operated in a so-called soft or hard regime.

In the hard regime, more energetic ions will always travel ahead of less energetic ones and will thus arrive at the detector first. In this regime, the acting Coulomb forces will spread the ion distribution.
In the soft regime, the positions of slow and fast ions are reversed. Thereby, the electric forces will lead to an equalization of kinetic energies and promote self-bunching effects.

In the NT │ TFS mode, the time-focus is placed shortly behind the ion trap. Although the analyzer is not operated in the hard regime per se, fast ions will travel ahead of slow ions for all subsequent turns, until the time-focus is finally shifted to the detector with the TFS turn. For all other modes, the time-focus is either in or behind the analyzer, which then acts as being in an isochronous or soft regime. In those regimes, self-bunching effects were found to be present in [Grinfeld et al., 2014], and consequently in this work. In this context, the "softness" of the analyzer increases from 0.5 TFS │ NT │ 0.5 TFS over the NT only to the operational mode, where the position of time-focus is placed on the detector during all normal turns.

Therefore, despite yielding compact peak widths over a large range of ion and turn numbers, the 0.5 TFS │ NT │ 0.5 TFS mode should not be used as mode of operation. The distributions of two ions species with close-by masses will start to overlap in the time-energy phase space (peak coalescence), and the actual mass resolving power will be much lower than calculated on the basis of the peak width. This can be seen in figure 6.16, where two nearby species (relative mass difference of $2 \cdot 10^{-5}$) with 100 ions each have been simulated for 128 normal turns.

On the other hand, the NT │ TFS mode seems to be a promising operation mode due to the absence of self-bunching. Here, peak coalescence effects are not found to be present (compare with figure 6.17), and the inclined phase space distribution can be easily corrected by adjusting TFS voltages to provide a first-order time-focus despite space charge (see the following section 6.4).
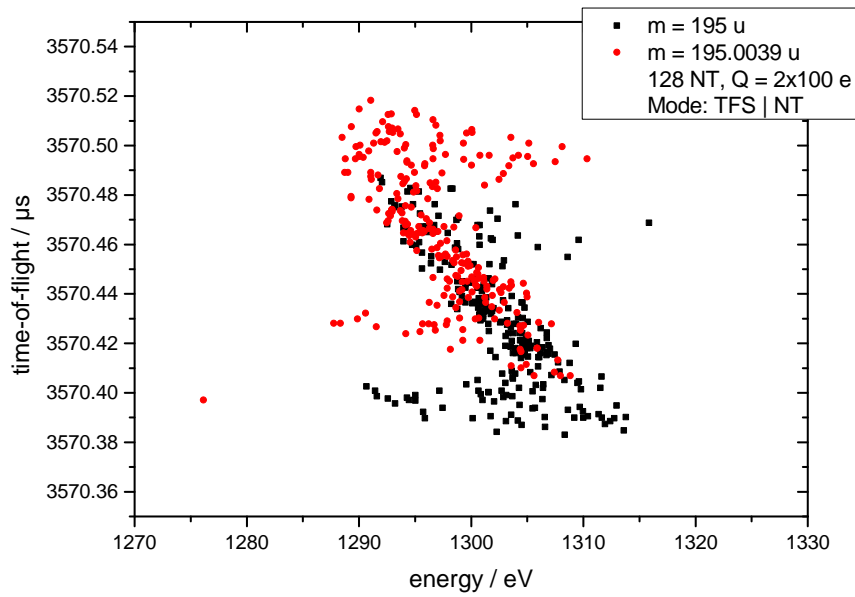
Figure 6.16: Investigation of peak coalescence in the operational (TFS │ NT) mode. After 128 normal turns, the phase space distributions of the two ions species ($Q = 100$ e each) overlap, and the masses remain unresolved in the time-of-flight spectrum ($R \geq 50,000$ needed).
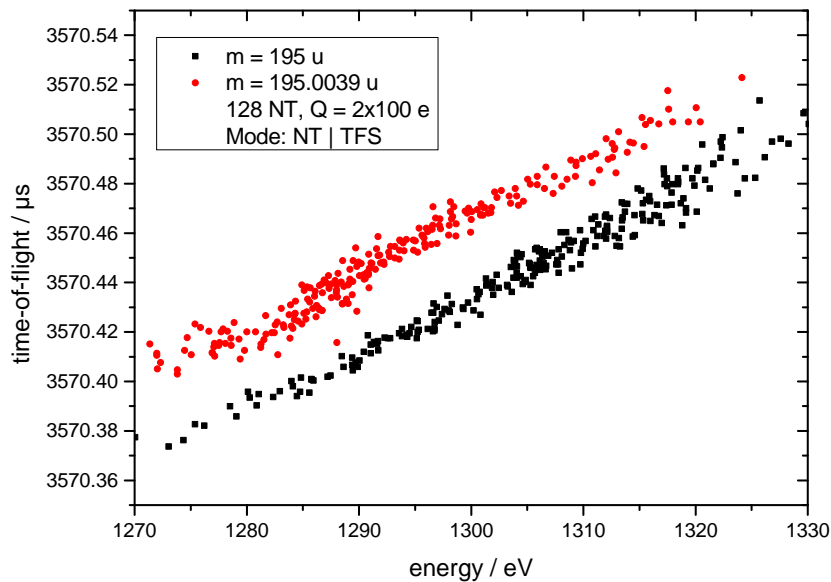

Figure 6.17: Investigation of peak coalescence in the NT │ TFS mode. In contrast to the TFS │ NT mode, the ions' phase space distributions remain separated and can be adjusted to achieve a first-order time-focus by tuning TFS voltages accordingly.

6.4 First-Order Time-Focus Correction

As mentioned in the previous section, it is in principle possible to decrease the peak width or to reduce peak coalescence of an ion time-of-flight distribution under space charge effects by correcting for the first-order time-focus. In experiment, this is quite easily accomplished by tuning the outer electrodes of the analyzer in TFS mode by a few volts. Of course, each specific voltage setting would only be valid for a certain range of ion numbers, since the amount of inclination clearly depends on the ion count per cycle.

The effect of first-order correction on the ions' time-of-flight distribution is exemplarily depicted in the figures 6.18 and 6.19. Figure 6.18 shows the time-of-flight distribution corresponding to the time-energy phase space presented in figure 6.17. The distributions are separated in the time-energy phase space, but can not be distinguished in the time-of-flight spectrum. In contrast, two seperate peaks are created if a first-order correction is applied, which is shown in figure 6.19. Here, the ions' flight times t were linearly corrected according to their energies K:

$$t_{new}\,(\mu\text{s}) = t_{old}\,(\mu\text{s}) + (1300\,\text{eV} - K\,(\text{eV})) \cdot 0.0025\,\frac{\mu\,\text{s}}{\text{eV}} \qquad (6.1)$$

As can be seen in figure 6.17, with this correction both peaks are now clearly resolved, even under the presence of space charge effects.
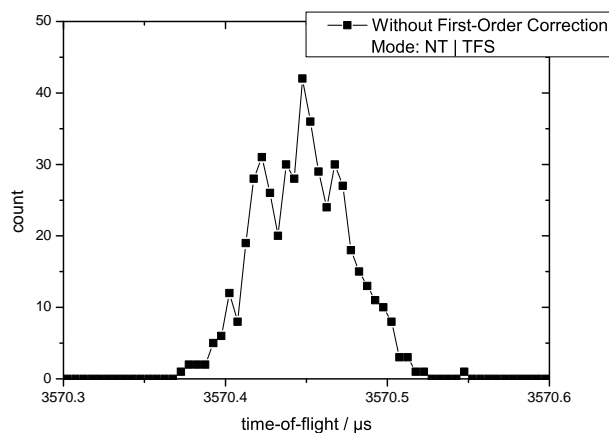

Figure 6.18: Time-of-flight spectrum of the two ion species shown in figure 6.17 (relative mass difference of $2 \cdot 10^{-5}$) without first-order correction.
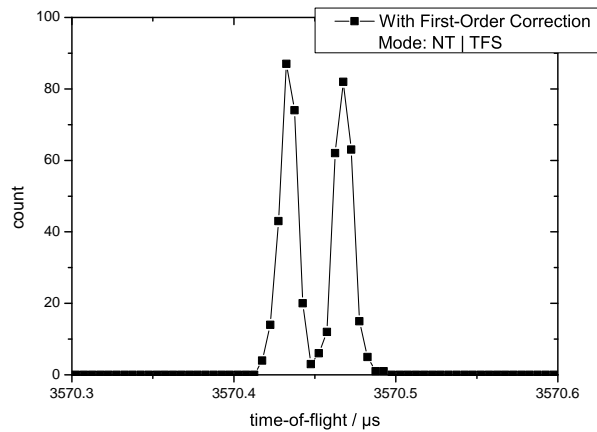
Figure 6.19: Time-of-flight spectrum of the two ion species shown in figure 6.17 after applying the first-order correction specified in equation (6.1). Due to this correction, both peaks are now clearly resolved.

Even though the NT $|$ TFS mode seems to be especially suited for this procedure due to the absence of self-bunching for the simulated ion numbers, first-order corrections can in general also be applied when the analyzer is operated in a different mode. This is shown in figure 6.20, where a peak has been measured in 1 TFS and 128 NT operational mode for two different sets of TFS voltages on E1 and E9. Once again, this procedure is only reasonable for a certain number of turns and ions per cycle, but can be very helpful to separate two close-by peaks of similar intensity or to improve the peak width of the ion of interest.
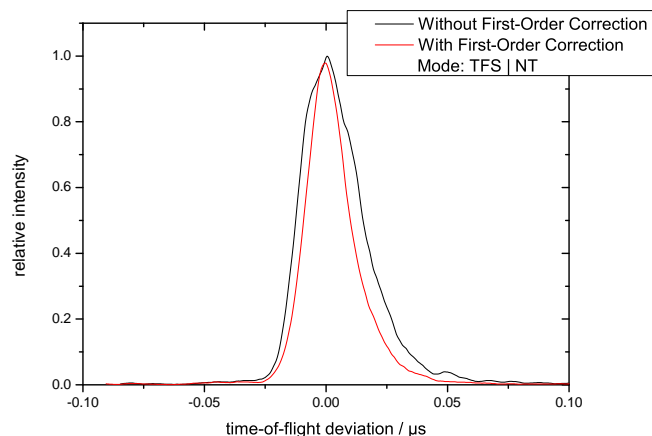
Figure 6.20: Measurement of a caffeine peak with and without additional first-order time-focus correction that accounts for space charge effects. Both peaks comprise the same amount of ions per cycle (≈ 60) and have been recorded in 1 TFS and 128 NT mode. First-order correction results in a 30% smaller peak width. Before this measurement, the analyzer had been optimized for the operation with low ion rates.

6.5 Extraction Field Strength

Another way to avoid space charge effects is to increase the strength of the ion trap's extraction field. This reduces the ions' turn-around time and thus the flight time that is required to achieve a certain mass resolving power. As a consequence, the instrument can be operated with a higher repetition rate. Additionally, it increases the initial energy spread of the ions, which significantly weakens space charge effects. In figure 6.21 results of simulations with half and double the normal extraction field strength (EFS) are shown. The plots display the expected strong dependence of self-bunching effects on the initial energy spread. Therefore, high extractions field strengths should be preferably used as long as the energy acceptance of the analyzer is not exceeded.
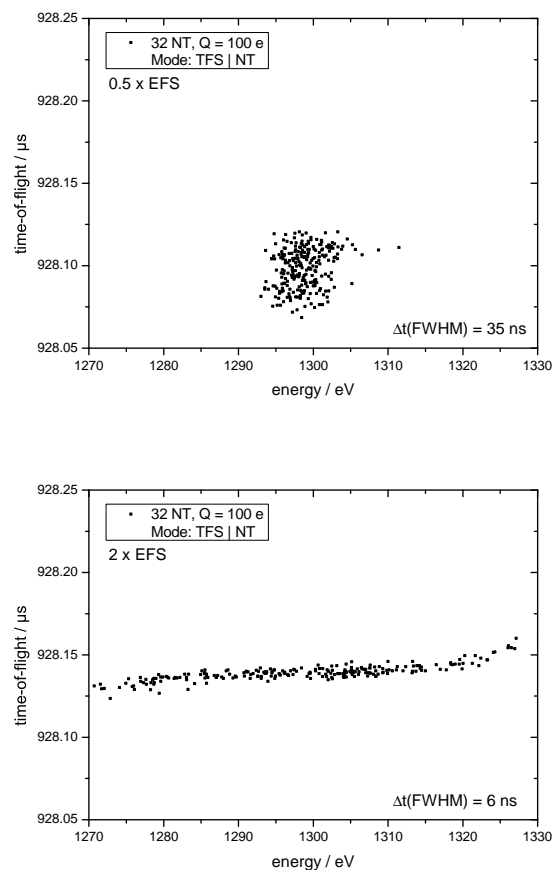
Figure 6.21: Space charge simulations with different extraction field strengths. The resulting peak widths differ significantly. Self-bunching (and consequently peak coalescence) is strongly suppressed in the lower plot with $\pm$ 734 V trap potential during extraction. In both cases, the phase space of 100 ions was recorded after 32 normal turns. For $\pm$ 367 V (corresponds to standard EFS), the peak width is 17 ns.

6.6 Overall Improvement of Rate Capability

With the current operational mode of the MR-TOF-MS, a mass resolving power of 100,000 can be reached for 25 ions per cycle in 128 turns (see figure 6.7). For this setting, space charge effects such as the increase of peak width and the occurrence of peak coalescence are almost negligible. The corresponding flight time amounts to 3.6 ms for caffeine and thereby limits the ion rate to about 5000 ions per second. However, this (space charge imposed) rate limit is only valid for ions of one specific mass-to-charge ratio, whereas the overall ion rate capability for the total mass range can be a lot higher than that.

Simulations show that placing the time-focus shifting at the end of the ions' flight path (NT │ TFS mode) and utilizing the correction of first-order time-focus via tuning of the mirror electrodes results in a strong reduction of space charge effects for 100 ions and 128 normal turns. Peak coalescence between two ion species with a relative mass difference of $2 \cdot 10^{-5}$ can be completely avoided under these conditions (compare with the time-energy phase space plots in figures 6.16 and 6.17, and with the method of first-order time-focus correction presented in section 6.4). In this way, a resolving power of 100,000 can also be achieved for 100 ions per cycle, thus increasing the maximum ion rate by factor of 4.

The ion rate capability of the MR-TOF-MS can be further increased, if the ion trap is operated with an electric potential of $\pm$ 734 V during extraction. This extraction voltage is technically feasible and also compatible with the energy acceptance of the analyzer. Simulations with 100 ions and 32 turns in NT mode show that for this case the peak width can be decreased by a factor of 3 compared to the operation of the MR-TOF-MS with its current extraction voltage of $\pm$ 367 V. The small peak width of $\Delta t = 6$ ns is caused by shorter turn-around times, and by weaker ion-ion interactions due to an increase of the initial energy spread. Resolving powers of 75,000 are already achieved after a flight time of about 900 μs for caffeine, hence enabling a factor 4 higher repetition rate.

Consequently, with a combination of these measures, the maximum rate for one single ion species can be improved by more than one order of magnitude. For masses that are separated by a relative mass difference of $2 \cdot 10^{-5}$, rates of more than 10^5 ions per second become achievable. The exact value depends, of course, on experimental conditions like the desired resolving power and the mass-to-charge ratio of the ion of interest.

7 Tandem Mass Spectrometry

It was a prime goal of this work to implement collision-induced dissociation as well as to improve ion re-trapping as method for high-resolution precursor selection in the mobile MR-TOF-MS. In tandem MS measurements, the ions of interest are re-trapped and dissociated in the ion trap, and their product ions are injected into the analyzer for a subsequent mass measurement afterwards. The turn numbers for re-trapping and mass measurement can be independently adjusted in accordance to the requirements of the particular experiment, e.g. in terms of measurement duration and mass resolving power. In this chapter, measurements demonstrating the tandem MS capabilities and performance of the MR-TOF-MS are presented.

7.1 Collision-Induced Dissociation

In the MR-TOF-MS CID is realized by means of excitation of the ions' macromotion in the RF ion trap (see section 4.1.3). In figure 7.1 the relative abundance of protonated caffeine and its product ion at mass 138 u is depicted in dependence of the applied excitation voltage. This fragment is created by a retro-Diels-Alder reaction [Williams et al., 2006]:

$$C_8H_{11}N_4O_2 \xrightarrow{\text{$-$CH$_3$NCO}} C_6H_8N_3O$$

Here, caffeine was excited for a duration of 2 ms with a resonance frequency of 113 kHz. The nominal excitation voltage was ramped in 100 mV steps from 0 V up to 2 V during the measurement. At about 1.2 V equal amounts of precursor and product ions were detected (compare with the CID spectrum attached to the corresponding data point in fig. 7.1). The pressure of N_2 was regulated to be $1.25 \cdot 10^{-4}$ mbar in the beam preparation system and hence about $8 \cdot 10^{-3}$ mbar in the ion trap (calculated value, see [Lang, 2016]). The graphs clearly illustrate the strong and well-defined impact of the excitation voltage on the percentage of ion dissociation. In addition to the excitation voltage, the excitation time and the resonance frequency can be adjusted to meet the desired level of fragmentation. Further examples of CID spectra can be found in the following sections. In

addition to caffeine, the two amino acids glutamine and lysine as well as a crude oil sample have been successfully fragmented in the scope of this work.
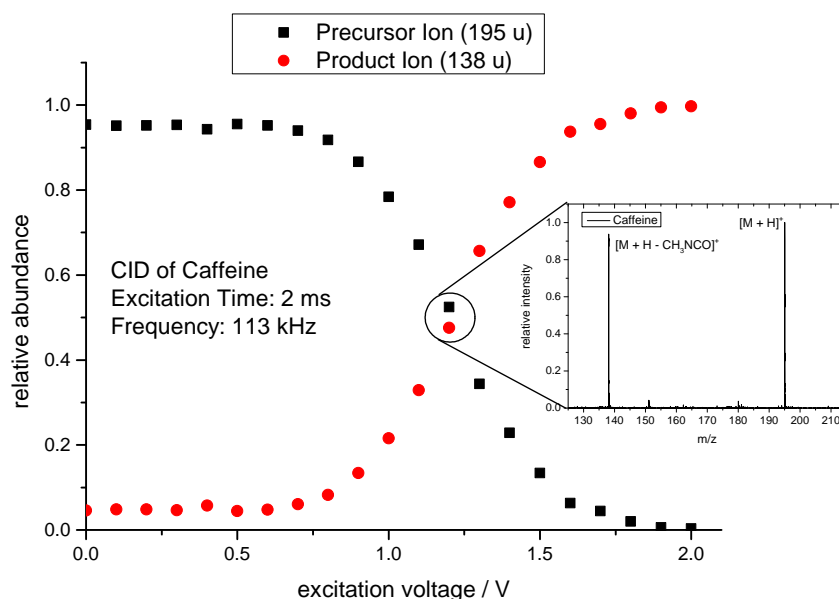

Figure 7.1: Relative abundance of caffeine's precursor and product ion at mass 138 u in dependence of the excitation voltage. The total abundance has been normalized separately for each spectrum. Pressure, excitation time and resonance frequency remained fixed during this measurement. With an excitation voltage of 2 V, a dissociation efficiency of 100% is reached.

7.2 Re-Trapping: Separation Power and Efficiency

Since ion re-trapping is an essential prerequisite for tandem MS in the MR-TOF-MS, its performance in terms of separation power and efficiency has been investigated in detail.

The separation power and the efficiency of ion re-trapping (see section 2.4.6) have thus been determined for different turn numbers and re-trapping potentials. The number of normal turns was set to 1, 8, 16, 32, 64 and 128, amounting to a re-trapping time-of-flight of up to 3.6 ms for caffeine, which was chosen as analyte for these measurements. The re-trapping potential (i.e. the axial well depth) was varied between 2 V, 3 V, 5 V and 10 V. Since the ions' time-dispersion is converted into an energy-dispersion in the ion trap, the trap depth determines the maximum mass separation power that can be achieved.

For each individual measurement, the time (referred to as re-trapping time-of-flight) after which the trap potential was switched from retarding to re-trapping

voltages was scanned. The corresponding ion abundance was measured in a mass spectrum that was recorded in succession to the re-trapping process. Thereby, a plot as shown in figure 7.2 is obtained. With that, the separation power is determined by dividing the ions' re-trapping time-of-flight by the full width at half maximum of the distribution.

For convenience, the 1 TFS turn that is always performed at the very beginning of *the ions' flight path is not denoted in the figures of this chapter 7.* However, the number of normal turns in re-trapping and mass measurement mode is shown (e.g. 128 NT RT │ 1 NT MS). If collision-induced dissociation is utilized in between both modes, it will be indicated with a CID tag.
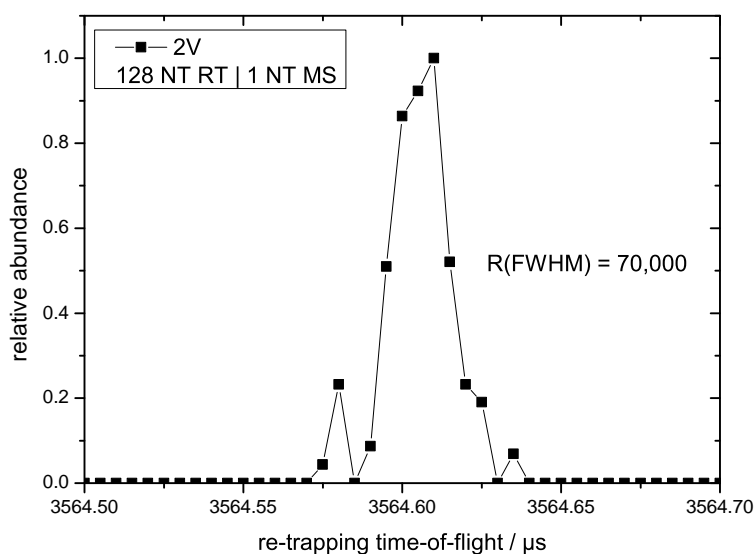
Figure 7.2: Determination of separation power for a 2 V re-trapping potential after 128 normal turns (in addition to 1 TFS turn) in re-trapping mode. The analyzer was operated in 1 TFS and 1 NT turn mode for the subsequent ion abundance measurements.

Figure 7.3 illustrates the separation power of the MR-TOF-MS over a large range of turns and re-trapping potentials. As one would expect, the separation power increases linearly with the time-of-flight. For the most sensitive RT potential of 2 V, a separation power of 10,000 is reached after 500 μs flight time only. For the same potential and with a time-of-flight of about 3.6 ms a separation power of 70,000 was measured (see figure 7.2).

If only two ion species have to be separated, the separation power of ion re-trapping is not necessarily determined by the full width, but rather by the rising or falling edge of the ion distribution (compare with fig. 7.2). The re-trapping time can be adjusted such that one of the isobars is recaptured (i.e. is placed inside the acceptance window), whereas the other one is placed outside the rising

or falling edge of the distribution. Thereby, even higher separation powers than shown in figure 7.3 can be obtained.
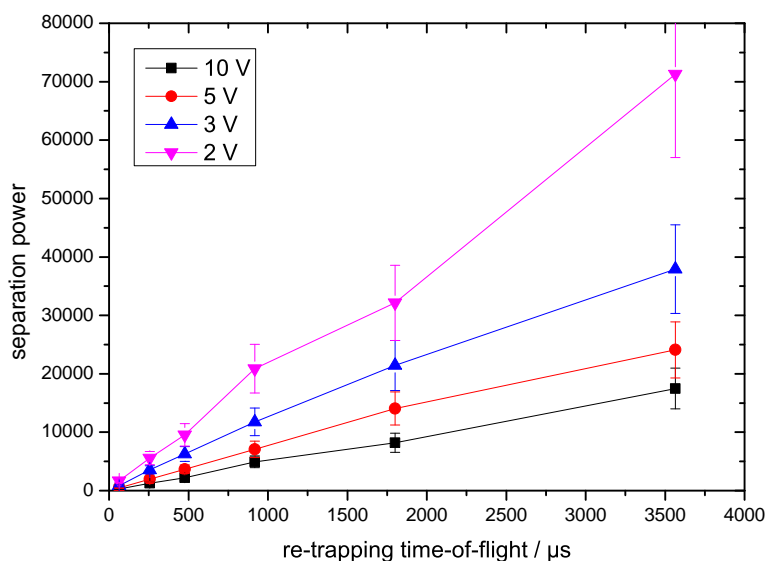

Figure 7.3: The separation power of the MR-TOF-MS in dependence of the re-trapping time for various re-trapping potentials. For a re-trapping potential of 2 V and a time-of-flight of 3.6 ms (which corresponds to 128 NT), a separation power of about 70,000 is achieved.
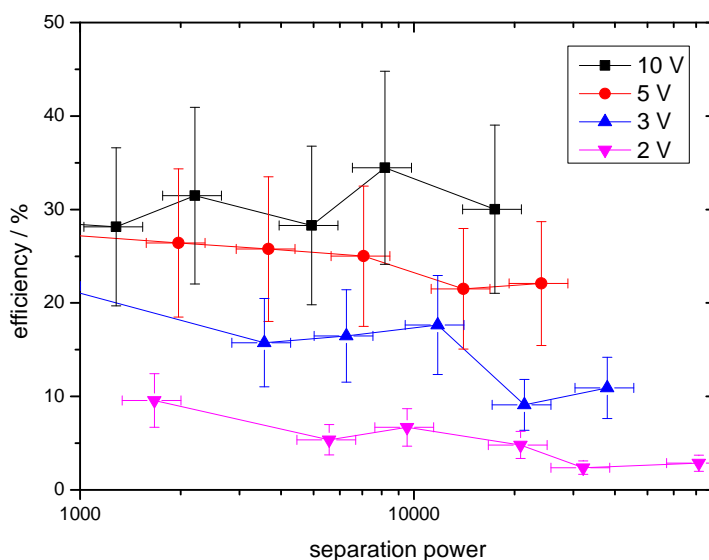

Figure 7.4: The MR-TOF-MS' re-trapping efficiency in dependence of separation power. The efficiency has been corrected for ion losses that occur due to collisions with residual gas in the analyzer (see section 5.3).

The re-trapping efficiency in dependence of separation power is presented in figure 7.4. To determine the efficiency, the ratio of ion abundance with and without preceding ion re-trapping was measured, and this value was then corrected for collisional losses in the analyzer. The efficiency measurements were performed with a high number of ions (several tens to a few hundred per cycle) to yield high statistics, and are thus influenced by space charge effects. Simulations indicate negative effects of space charge on the re-trapping efficiency, with the result that the actual efficiency (for fewer ions per cycle) may be higher than stated.

The measurements of this work are in general agreement with the first re-trapping characterization measurements which are presented in the work of [Lang, 2016], where a separation power of 60,000 was obtained for ^{133}Cs ions after 129 revolutions with 1 V RT potential.

However, with the implementation of a shielding aperture for the RF ion trap (see section 4.1.4) the re-trapping procedure could be strongly improved. A higher separation power has been achieved with a re-trapping potential half as sensitive, and the efficiency was increased by factor of 3.

7.3 MS/MS

The two isobars glutamine and lysine (146 u) have been chosen to demonstrate the instrument's tandem MS mode. Glutamine and lysine are two of the 20 essential amino acids and have a mass difference of 36.4 mu only. To separate these two molecules, a resolving power greater than 4000 is needed.

For this measurement the amino acids were dissolved in a H_2O/MeOH (1/1) solution with 0.1% formic acid with a concentration of approximately 10^{-4} mol/l. The sample was prepared to yield about the same intensity for both analytes.

Figure 7.5 contains three mass spectra which were obtained after 7 normal turns in re-trapping and 8 normal turns in mass measurement mode. Between these spectra, the RT time was adjusted such that either both amino acids (upper spectrum) were recaptured - i.e. placed inside the window of acceptance - or just one of them (middle and lower spectrum). As can be seen, it was possible to successfully isolate glutamine as well as lysine from their respective isobaric contaminants.

The fragmentation patterns of protonated glutamine and lysine look quite similar [Choi et al., 2012]. Both lose an ammonia (NH_3), which leads to a prominent mass line at 130 u. The loss of H_2O is another major fragment ion in the dissociation spectrum of lysine, which results in a peak at mass 129 u. On the contrary, glutamine loses both H_2O and CO, which can be seen by a peak at mass 101 u.
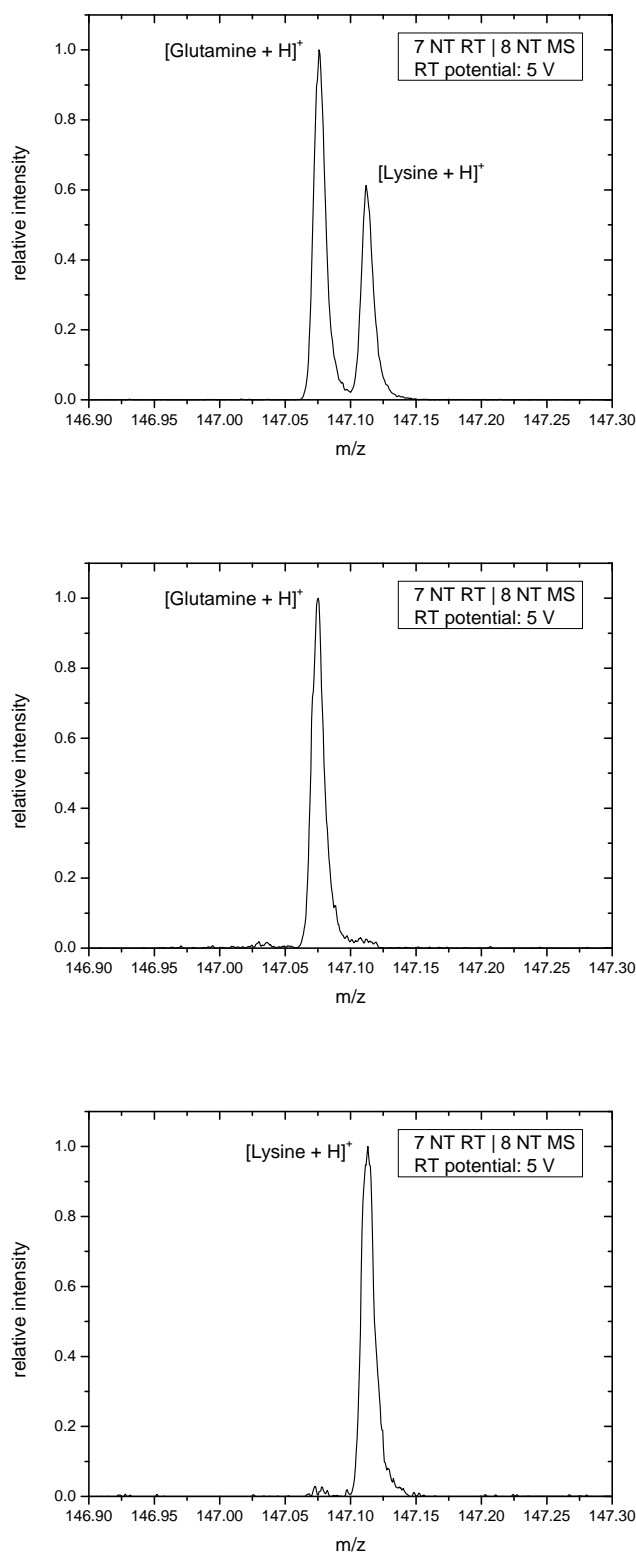
Figure 7.5: Isolation of the amino acids glutamine and lysine ($\Delta m = 36.4$ mu). In the upper spectrum the re-trapping time was chosen such that both analytes were simultaneously re-trapped in the ion trap. In the middle and bottom spectrum either glutamine or lysine were isolated from their isobaric counterparts.
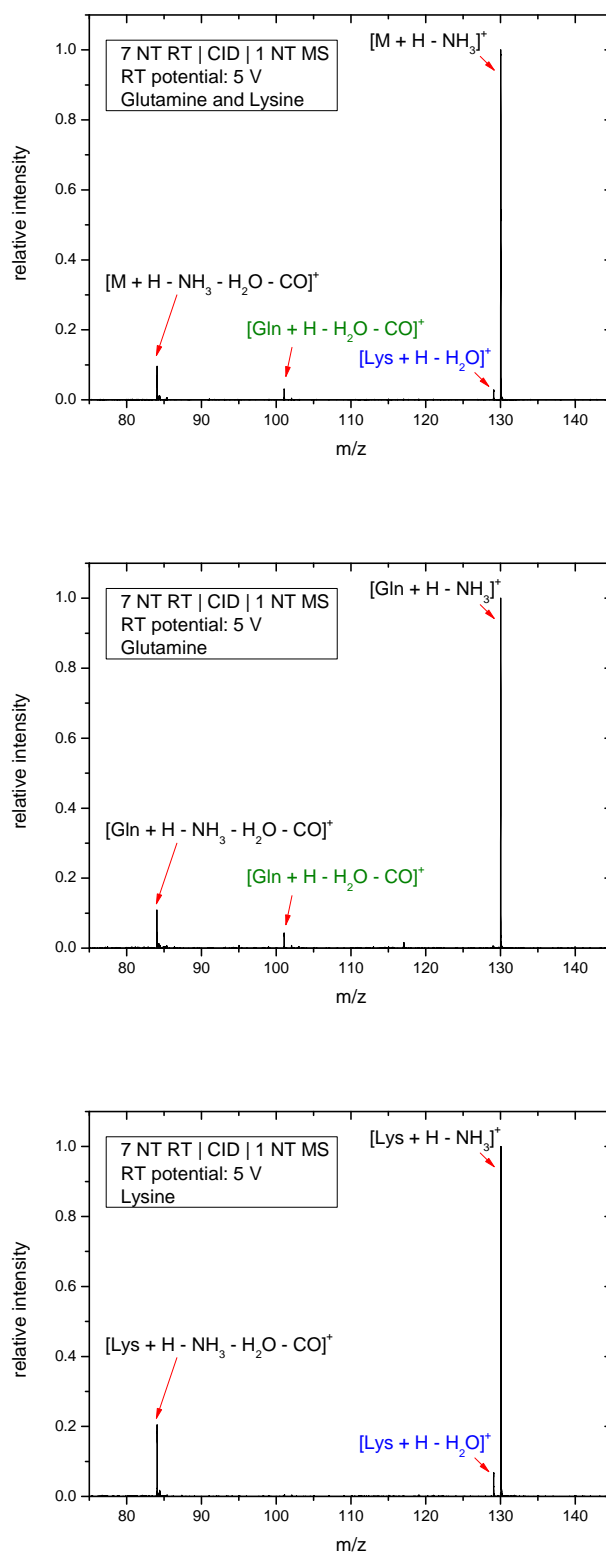
Figure 7.6: MS/MS spectra of glutamine and lysine. In the upper spectrum, both amino acids are re-trapped and fragmented together. The middle and bottom plot show MS/MS spectra of the amino acids after their isolation. Their respective fingerprint fragments are indicated in green (Gln) and blue (Lys) color.

The MS/MS spectra corresponding to the measurements of figure 7.5 are shown in figure 7.6. The dissociation spectra can be easily distinguished with the help of the fragmentation patterns discussed before. The spectrum at the top comprises fragments of both amino acids, whereas the one in the middle only contains glutamine product ions. The bottom spectrum can be assigned to lysine, with its fragment at mass 129 u and a missing mass line at 101 u.

This measurement clearly demonstrates the importance of having high-resolution mass separation in the first stage of an MS/MS measurement. Unambiguous dissociation spectra of both amino acids (with a relative mass difference of $2.5 \cdot 10^{-4}$) have been successfully generated, although their respective isobaric counterpart was simultaneously present in the sample. Since the MR-TOF-MS provides even higher separation powers of up to 70,000, a rich field of possible tandem MS applications becomes available.

7.4 MS^n Capability

The MR-TOF-MS allows for tandem-in-time. All stages of mass separation can be performed consecutively in the same time-of-flight analyzer. This is done by re-trapping the ions in the RF ion trap they are initially injected from. Therefore, no general limit is imposed with respect to the number of separation steps that can be realized, which renders the conduction of MS^n ($n \geq 2$) experiments possible.

To illustrate the MS^n capability of the instrument, lysine and its fragments were measured in an MS^3 experiment. The fragmentation pathway that has been utilized in this measurement reads as follows:

$$C_6H_{15}N_2O_2 \xrightarrow{\ -NH_3\ } C_6H_{12}NO_2 \xrightarrow{\ -H_2O-CO\ } C_5H_{10}N$$

Two distinct resonance frequencies were used to excite the macromotion of the different masses. For resonant excitation of protonated lysine (147 u), a frequency of 112 kHz and an amplitude of 1 V was used over a time span of 3 ms. Its fragment at mass 130 u was excited by a 140 kHz signal at an amplitude of 3 V. In this case, the signal was applied for 2 ms. The analyzer was operated in 1 TFS and 1 NT mode during all stages of mass isolation and measurement.
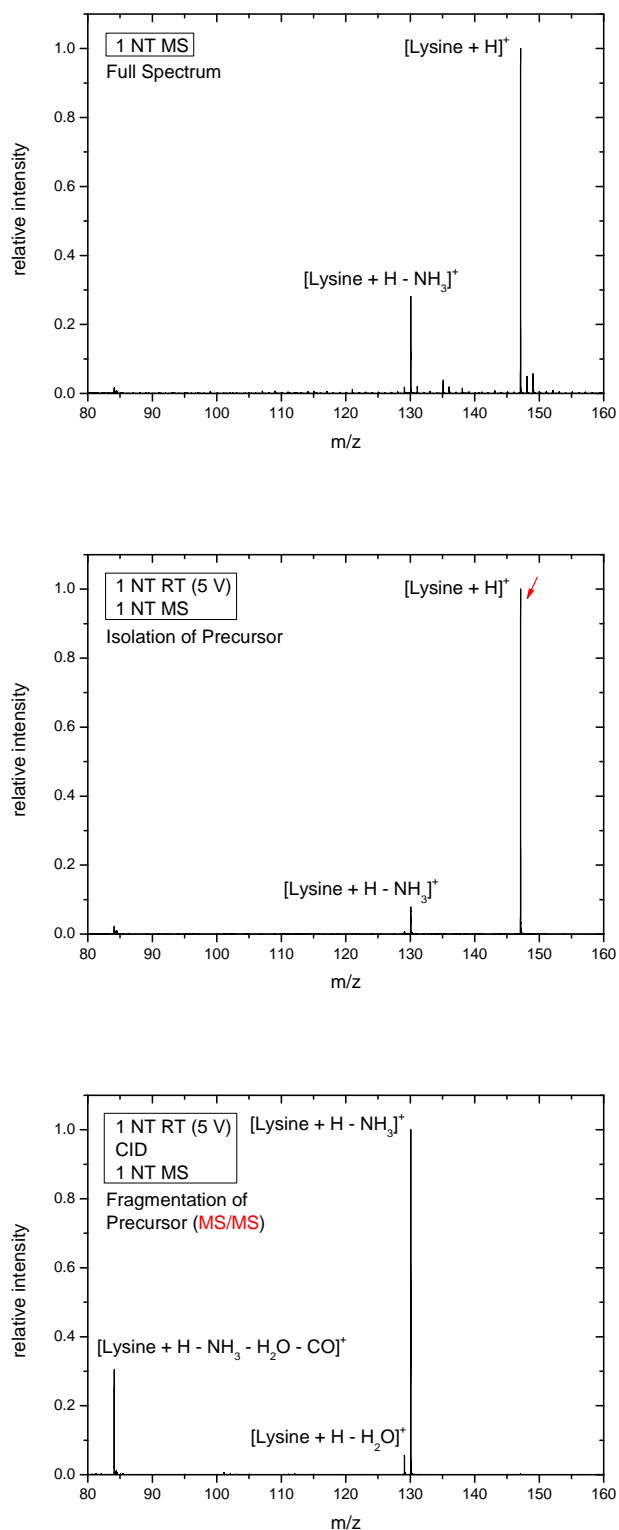
Figure 7.7: The first few steps of the MS^3 process up to MS/MS of lysine are illustrated. Protonated lysine is isolated (middle) and then fragmented by CID (bottom). Fragments that appear without the application of CID originate from dissociation processes caused by the RF potential of the ion trap.
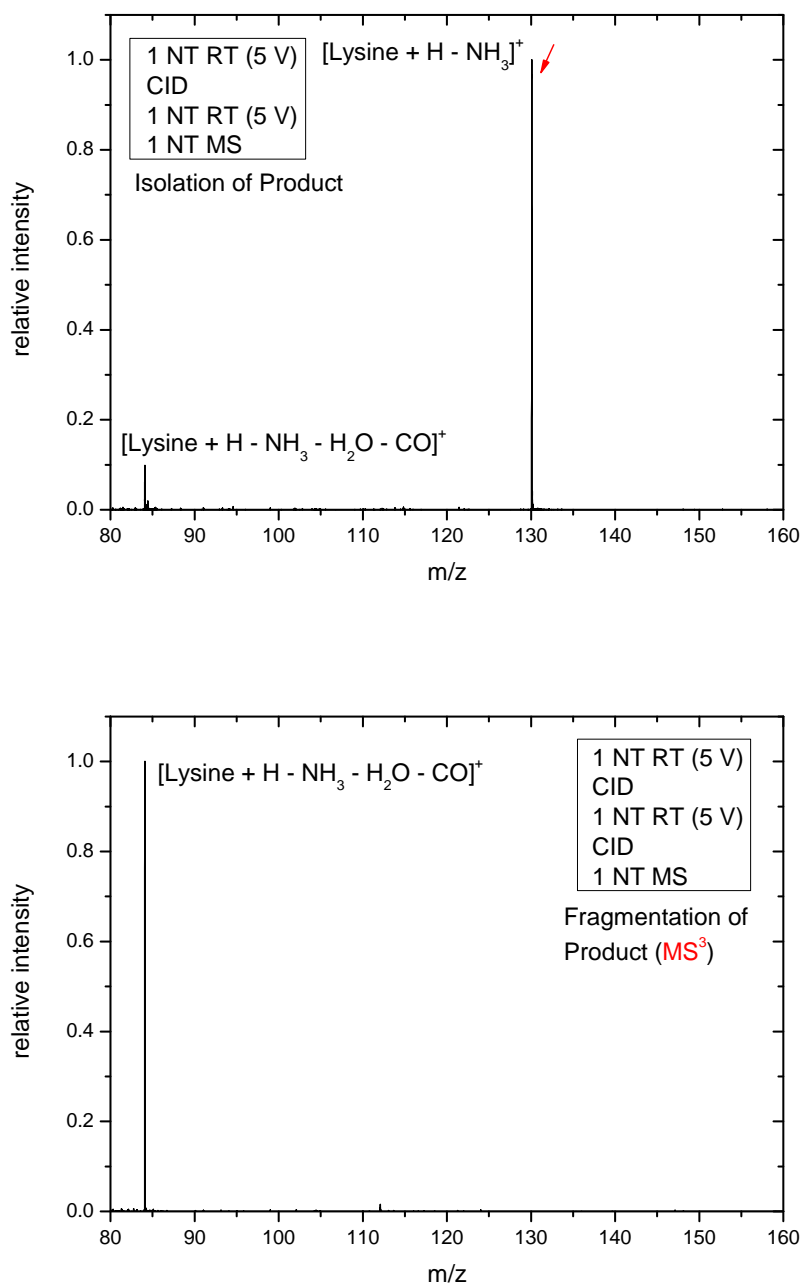
Figure 7.8: Top: the product ion of lysine at mass 130 u is isolated in a second re-trapping step. The small amount of its fragment at mass 84 u is present due to dissociation induced by the ion trap's regular RF field. The product ion of lysine at mass 129 u is rejected in the separation process.

Bottom: the peak at 130 u completely vanishes with the application of CID and a very prominent product ion peak is created at 84 u.

As a first step, lysine was isolated and dissociated. This can be seen in figure 7.7, where each individual step up to MS^2 is depicted. In the middle spectrum, protonated lysine is isolated from any chemical contaminants that were present in the sample. Since the ions are confined by a quadrupole RF field in the ion trap, a small amount of lysine is already fragmented (130 u), even with the absence of auxiliary excitation fields. Note, that due to the separation process neither lysine nor its product are accompanied by isotopic mass lines. In the bottom spectrum CID was applied, and the typical fragmentation pattern was produced as a result.

In succession to CID, the prominent product ion at mass 130 u was re-trapped (compare with fig. 7.8). Again, a small amount of its fragment at mass 84 u is already present due to fragmentation that is induced by the regular RF potential of the ion trap. It is important to note that the mass line at 129 u is missing in this spectrum, since it is a direct product ion of protonated lysine and not obtained by the fragmentation of mass 130 u. In the last plot, CID was applied for the second time. The precursor ion was completely dissociated and the mass line of its fragment at 84 u was generated.

7.5 Application: Crude Oil Analysis

The results of the previous sections have shown that the MR-TOF-MS is well suited for tandem mass spectrometry experiments - especially for those which require high separation powers to isolate the ion of interest from its contaminants.

The mass spectrometric analysis of complex volatile and nonvolatile crude oil components falls into the category of such experiments and is one of the most challenging fields in mass spectrometry [Panda et al., 2007]. Crude oil samples are extremely complex and can contain several ten thousand different components. Mass measurements yield dense mass spectra and tens of isobaric constituents at each mass unit. Thus, it is difficult to determine the exact chemical composition of the sample and the use of highly accurate mass spectrometers is vital. If one is interested in the chemical structure of a certain ion species the task becomes even more difficult, since conventional tandem mass spectrometers do not allow for the isolation of molecules from their nearby isobaric contaminants. Hence, fragment spectra always contain product ions of many ion species, which makes the determination of chemical structures very challenging or even impossible.

In the following, results of a crude oil measurement with the MR-TOF-MS are presented. The sample was provided by the Max Planck Institute for Coal Research located in Mülheim an der Ruhr and contained 250 ppm crude oil in a toluene/MeOH (1/1) solution [Schrader, 2015]. In figure 7.9 an overview of the sample spectrum over a range of 175 masses is shown. The mass resolving power for this 1 TFS turn only mode is about 3,500. From this spectrum, a single mass line at 337 u was isolated with ion re-trapping (see fig. 7.10).
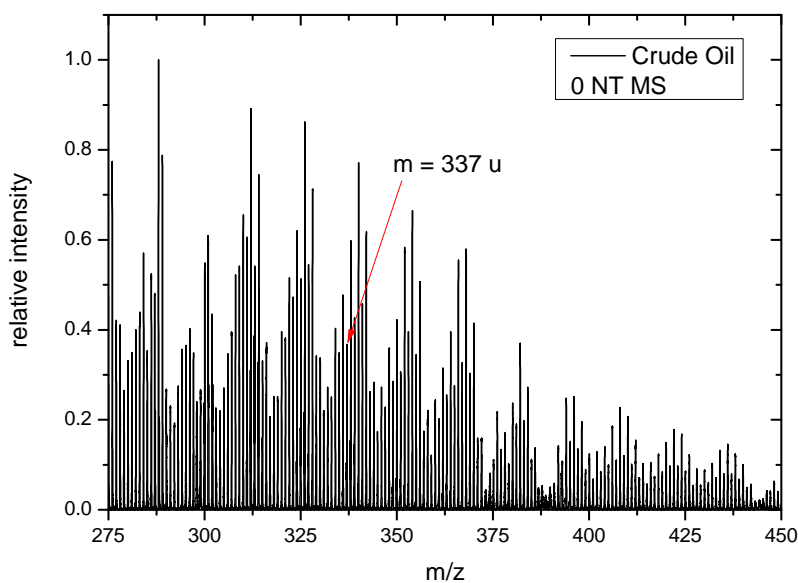
Figure 7.9: An overview mass spectrum of the crude oil sample. The mass line at 337 u is highlighted, since it was further investigated in measurements presented in the following figures.
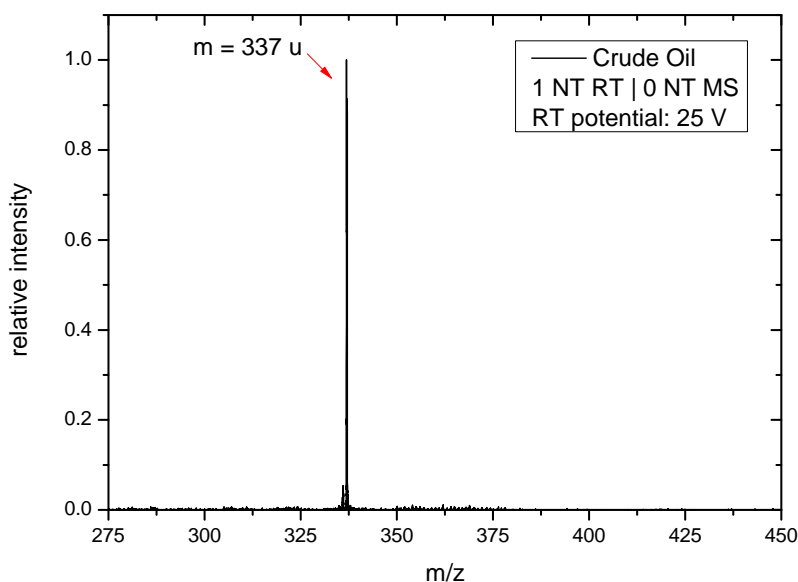
Figure 7.10: Isolation of mass 337 u from the crude oil spectrum with 1 normal turn in ion re-trapping mode. This resolution is already close to the limits of what a typical high-resolution quadrupole mass filter can achieve in terms of precursor selection. The mass spectrum still contains many masses, as can be seen in figure 7.11.

A high-resolution mass spectrum of mass 337 u is depicted in figure 7.11. This spectrum has been recorded after 1 turn in TFS and 64 turns in normal mode. The mass range is restricted to 0.25 u by ion re-trapping prior to the mass measurement. As one can see, even in this small mass window many isobaric ions can be found. For calibration of the mass spectrum, hexamethoxyphosphazene (322 u) was recorded with the same settings in a different measurement and used as external calibrant.
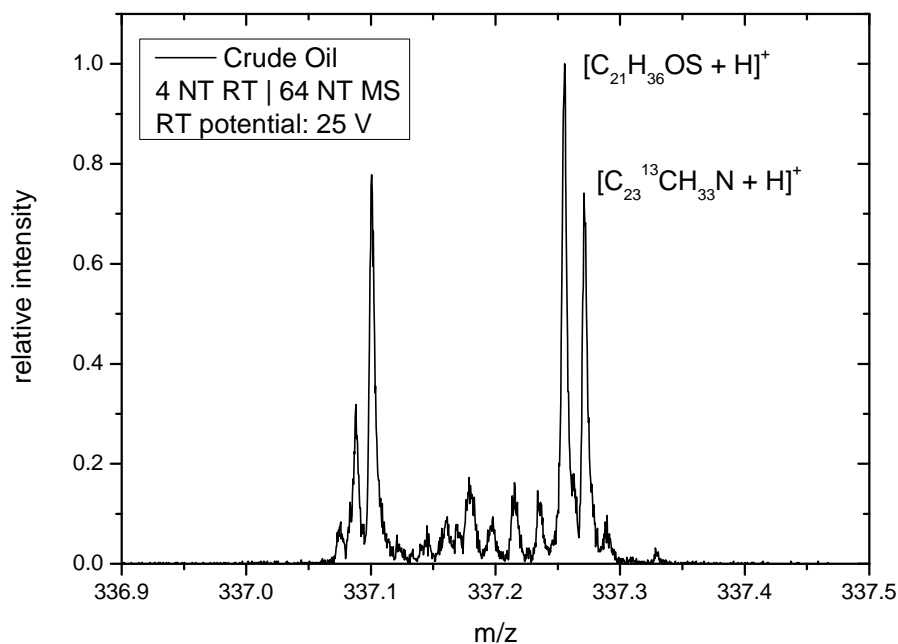
Figure 7.11: High-resolution spectrum of mass 337 u. Many isobaric mass lines can be found in the measured range from 337.05 u to 337.3 u. Evidently, the isolation of a single mass line in the overview spectrum would still not be enough to yield an unambiguous fragmentation pattern of a single ion species. The peaks on the right side of the mass spectrum are assigned to protonated $C_{21}H_{36}OS$ and $C_{23}{}^{13}CH_{33}N$, and could also be identified in a different measurement of the same sample [Vetere, 2016].

To obtain a fragmentation pattern that corresponds to a single specific compound, the separation power that precedes the CID process has to be increased. This has been done for the spectrum shown in figure 7.12. Here, protonated $C_{21}H_{36}OS$ has been successfully isolated with a mass window of less than 50 mu, which corresponds to a separation power of more than 7000.

With these setting, CID has been performed almost exclusively on protonated $C_{21}H_{36}OS$. The excitation was done by a 91 kHz signal with 3 V amplitude over a time span of 4 ms. The corresponding spectrum is presented in figure 7.13.

Dissociation of this molecule yields a typical fragment spectrum containing accumulations of product ions around masses that indicate a loss of one or several hydrocarbons.
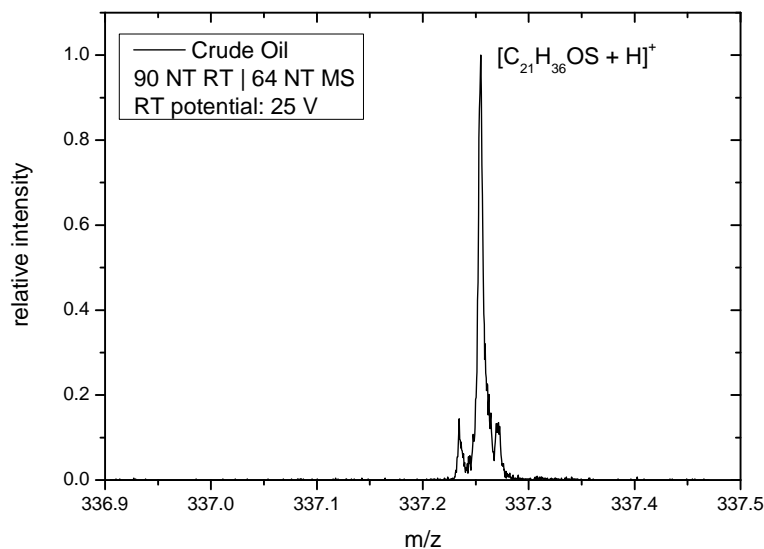

Figure 7.12: Isolation of protonated $C_{21}H_{36}OS$, which has a mass of 337.256 u. Re-trapping was performed with a separation power of about 7000, isolating the relevant peak in a mass window of 50 mu.
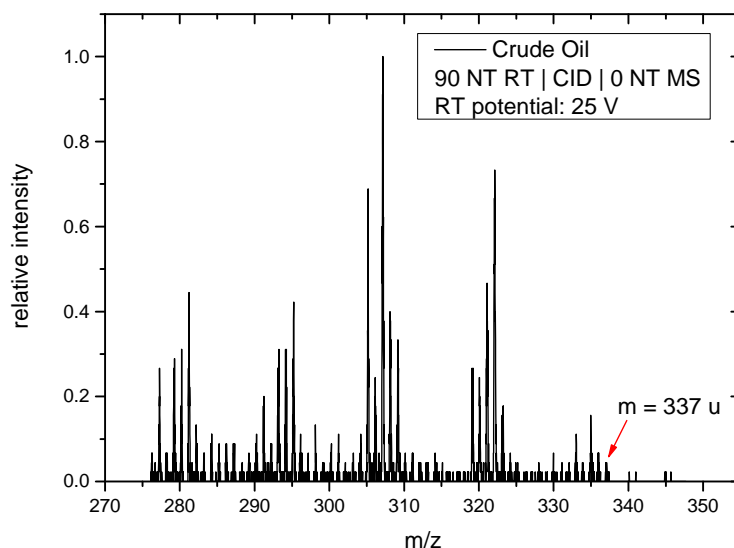

Figure 7.13: CID spectrum of isolated $C_{21}H_{36}OS$. As expected, the fragments are mainly located around masses that indicate a loss of one or several hydrocarbons.

7.6 Summary

With the MR-TOF-MS, tandem mass spectrometry experiments can be conducted with high-resolution in every stage of mass separation. The instrument provides separation powers of up to 70,000, and thereby exceeds the resolving power of conventional hybrid tandem mass spectrometers that use a quadrupole mass filter for precursor ion isolation by about two orders of magnitude.

Tandem mass measurements have been successfully conducted with the two amino acids glutamine and lysine, which are separated by a mass difference of 36.4 mu ($R > 4000$) only. High-resolution MS^n measurements can be performed in-time and with no additional instrumental stages required, as it has been shown on the example of an MS^3 experiment with lysine. Furthermore, a complex crude oil sample has been analyzed in a first proof-of-principle application and a dissociation spectrum for a mass window of 50 mu has been obtained.

These results clearly illustrate the advantage of having high separation powers in the first stage of MS/MS measurements. The mobile MR-TOF-MS produces clean and unambiguous dissociation spectra, even for the most challenging samples. This is of great benefit for the investigation of molecular structures and fragmentation pathways, and for the application of MS/MS to samples that provide complex spectra, such as crude oil or proteins, for instance.

8 Conclusion and Outlook

The mobile MR-TOF-MS for analytical mass spectrometry has met its designated performance parameters. High-resolution mass measurements with resolving powers greater than 200,000 have been performed with samples that were introduced into the instrument via its atmospheric pressure interface. Moreover, sub-ppm mass accuracies have been achieved for isotopes of caffeine and hexamethoxyphosphazene. The device is able to measure samples that cover a dynamic range of 5 orders of magnitude in analyte concentration, and can be operated in broad band and high-resolution mode, respectively.

Space charge effects that occur under high ion rates are well understood. Various approaches to increase the rate capability of the MR-TOF-MS, such as the use of higher extraction field strengths and the change of the operational mode, are already available and will be implemented to further enhance the rate capability of the MR-TOF-MS in the future.

The results of the tandem mass spectrometry measurements illustrate the importance of having high-resolution in every stage of mass analysis. With the novel technique of mass-selective ion re-trapping, separation powers of up to 70,000 have been reached. The MR-TOF-MS' potential has been shown in MS/MS and MS^3 measurements with the isobaric amino acids glutamine and lysine. In addition, a first proof-of-principle MS/MS experiment with a crude oil sample has been successfully performed.

Since the MR-TOF-MS offers a unique combination of features like short measurement times, high ion rate capability and high resolving power in both steps of tandem mass measurements, it will enable new types of experiments in the field of analytical mass spectrometry. Applications like wastewater monitoring and the analysis of contaminants in food benefit from the instrument's ability to perform high-resolution mass spectrometry in the field. Furthermore, the application of the MR-TOF-MS for the structural elucidation of molecules contained in crude oil samples looks particularly promising and is envisaged for future measurements.

Acronyms

ADC	Analog-to-Digital Converter
API	Atmospheric Pressure Interface
CID	Collision-Induced Dissociation
DAQ	Data AcQuisition
EFS	Extraction Field Strength
EMG	Exponentially Modified Gaussian
EMI	ElectroMagnetic Interference
ESI	ElectroSpray Ionization
FPGA	Field-Programmable Gate Array
FTICR	Fourier Transform Ion Cyclotron Resonance
FWHM	Full Width at Half Maximum
GC/MS	Gas Chromatography/Mass Spectrometry
GLN	Glutamine
IRMPD	InfraRed Multi-photon PhotoDissociation
LC/MS	Liquid Chromatography/Mass Spectrometry
LTQ	Linear Trap Quadrupole
LYS	Lysine
MCP	MicroChannel Plate
MeOH	Methanol
MRS	Mass Range Selector
MR-TOF-MS	Multiple-Reflection Time-of-Flight Mass Spectrometer
MS	Mass Spectrometry
Nano-ESI	Nano-ElectroSpray Ionization
NT	Normal Turn
PEEK	PolyEther Ether Ketone
PID	Proportional-Integral-Derivate
RFQ	Radio Frequency Quadrupole
RT	Re-Trapping
SC	Space Charge
SHV	Save High Voltage
SID	Surface-Induced Dissociation
TDC	Time-to-Digital Converter
TFS	Time-Focus Shifting
TOF	Time-of-Flight
TQ	Trajectory Quality
TRC	Time-Resolved Calibration
TTL	Transistor-Transistor Logic

List of Figures

List of Tables

Bibliography

[908 Devices, 2016] 908 Devices (2016). Spec Sheet M908.

[Audi et al., 2012] Audi, G., Kondev, F., Wang, M., Pfeiffer, B., Sun, X., Blachot, J., and MacCormic, M. (2012). The NUBASE 2012 evaluation of nuclear properties. *Chinese Physics C*, 36(12):1157–1286.

[Ayet San Andrés, 2014] Ayet San Andrés, S. (2012-2014). Passive voltage stabilization for an MR-TOF-MS. Private communication.

[Ayet San Andrés, 2015] Ayet San Andrés, S. (2012-2015). Fast high voltages switches. Private communication.

[Banerjee and Mazumdar, 2012] Banerjee, S. and Mazumdar, S. (2012). Electrospray Ionization Mass Spectrometry: A Technique to Access the Information beyond the Molecular Weight of the Analyte. *International Journal of Analytical Chemistry*, 2012:1–40.

[Becker et al., 2009] Becker, A., Dickel, T., Geissel, H., Petrick, M., Plaß, W., Scheidenberger, C., and Simon, A. (2009). Simplified radio frequency quadrupoles with a linear axial field based on highly resistive electrodes. DPG Frühjahrstagung, Bochum.

[Bergmann, 2015] Bergmann, J. (2015). Entwicklung und Anwendung einer integrierten Systemsteuerung und Datenaufnahme für Flugzeitmassenspektrometer. Master's thesis, Justus-Liebig-Universität Gießen.

[Bergmann, 2016] Bergmann, J. (2016). MAc: Documentation of Application for IONAS Giessen experiments. Manual.

[Brenton and Godfrey, 2010] Brenton, A. G. and Godfrey, A. R. (2010). Accurate Mass Measurement: Terminology and Treatment of Data. *Journal of the American Society of Mass Spectrometry*, 21:1821–1835.

[Brubaker, 1968] Brubaker, W. M. (1968). An improved quadrupole mass analyser. *Advances in mass spectrometry*, 4:293–299.

[Bruins, 1998] Bruins, A. P. (1998). Mechanistic aspects of electrospray ionization. *Journal of Chromatography A*, 794(1-2):345–357.

[Cameron and D. F. Eggers, 1948] Cameron, A. E. and D. F. Eggers, J. (1948). An Ion "Velocitron". *The Review of Scientific Instruments*, 19(9):605–607.

[Chen, 2008] Chen, L. (2008). *Investigation of stored neutron-rich nuclides in the element range of Pt-U with the FRS-ESR facility at 360-400 MeV/u.* PhD thesis, Justus-Liebig-Universität Gießen.

[Chen et al., 1995] Chen, R., Cheng, X., Mitchell, D. W., Hofstadler, S. A., Wu, Q., Rockwood, A. L., Sherman, M. G., and Smith, R. D. (1995). Trapping, Detection, and Mass Determination of Coliphage T4 DNA Ions by Electrospray Ionization Fourier Transform Ion Cyclotron Resonance Mass Spectrometry. *Analytical Chemistry*, 67(7):1159–1163.

[Choi et al., 2012] Choi, S.-S., Song, M. J., Kim, O.-B., and Kim, Y. (2012). Fragmentation patterns of protonated amino acids formed by atmospheric pressure chemical ionization. *Rapid Communications in Mass Spectrometry*, 27:143–151.

[Davis, 2003] Davis, R. (2003). The SI unit of mass. *Metrologia*, 40(6):299–305.

[de la Convention du Mètre, 2014] de la Convention du Mètre, O. I. (2006 (updated in 2014)). *The International System of Units (SI)*. Bureau International des Poids et Mesures.

[de Leenheer and Thienpont, 1992] de Leenheer, A. P. and Thienpont, L. M. (1992). Applications of isotope dilution-mass spectrometry in clinical chemistry, pharmacokinetics, and toxicology. *Mass Spectrometry Reviews*, 11(4):249–307.

[Dempster, 1918] Dempster, A. J. (1918). A new Method of Positive Ray Analysis. *Physical Review*, 11(4):316–325.

[DesignSoft, 2012] DesignSoft (1993-2012). TINA-TI V9: The Complete Electronics Lab. Software.

[Dickel, 2010] Dickel, T. (2010). *Design and Commissioning of an Ultra-High-Resolution Time-of-Flight Based Isobar Seperator and Mass Spectrometer*. PhD thesis, Justus-Liebig-Universität Gießen.

[Dickel et al., 2015] Dickel, T., Plaß, W., Andres, S. A. S., Ebert, J., Geissel, H., Haettner, E., Hornung, C., Miskun, I., Pietri, S., Purushothaman, S., Reiter, M., Rink, A.-K., Scheidenberger, C., Weick, H., Dendooven, P., Diwisch, M., Greiner, F., Heiße, F., Knöbel, R., Lippert, W., Moore, I., Pohjalainen, I., Prochazka, A., Ranjan, M., Takechi, M., Winfield, J., and Xu, X. (2015). First spatial separation of a heavy ion isomeric beam with a multiple-reflection time-of-flight mass spectrometer. *Physics Letters B*, 744:137–141.

[Dickel et al., 2016] Dickel et al. (2016). Time-Focus Shifting. Manuscript in preparation.

[Dodonov et al., 1997] Dodonov, A., Kozlovsky, V., Loboda, A., Raznikov, V., Sulimenkov, I., Tolmachev, A., Kraft, A., and Wollnik, H. (1997). A new technique for decomposition of selected ions in molecule ion reactor coupled with ortho-time-of-flight mass spectrometry. *Rapid Communications in Mass Spectrometry*, 11(15):1649–1656.

[Dole et al., 1968] Dole, M., Mack, L. L., Hines, R. L., Mobley, R. C., Ferguson, L. D., and Alice, M. B. (1968). Molecular Beams of Macroions. *The Journal of Chemical Physics*, 49(5):2240–2249.

[Ebert, 2011] Ebert, J. (2011). Konstruktion eines atmosphärischen Probeneinlasssystems für den Einsatz in der In-situ-Massenspektrometrie. Vertiefungsmodul.

[Ebert, 2016] Ebert, J. (2016). *Mass Measurements of ^{238}U-Projectile Fragments for the First Time with a Multiple-Reflection Time-Of-Flight Mass Spectrometer*. PhD thesis, Justus-Liebig-Universität Gießen.

[Fenn et al., 1989] Fenn, J. B., Mann, M., Meng, C. K., Wong, S. F., and Whitehouse, C. M. (1989). Electrospray ionization for mass spectrometry of large biomolecules. *Science*, 246(4926):64–71.

[Fenselau, 1992] Fenselau, C. (1992). TANDEM MASS SPECTROMETRY: The Competitive Edge for Pharmacology. *Annual Review of Pharmacology and Toxicology*, 32:555–578.

[F.W. Aston M.A. D.Sc., 1919] F.W. Aston M.A. D.Sc. (1919). LXXIV. A positive ray spectrograph. *Philosophical Magazine Series 6*, 38(228):707–714.

[Glish and Burinsky, 2008] Glish, G. L. and Burinsky, D. J. (2008). Hybrid Mass Spectrometers for Tandem Mass Spectrometry. *Journal of the American Society for Mass Spectrometry*, 19(2):161–172.

[Glish and Vachet, 2003] Glish, G. L. and Vachet, R. W. (2003). The basics of mass spectrometry in the twenty-first century. *Nature Reviews Drug Discovery*, 2:140–150.

[Goldstein, 1886] Goldstein, E. (1886). Canalstrahlen. *Sitzungsbericht der Preussischen Akademie der Wissenschaften*, 691(691-699).

[Grinfeld et al., 2014] Grinfeld, D., Giannakopulos, A. E., Kopaev, I., Makarov, A., Monastyrskiy, M., and Skoblin, M. (2014). Space-charge effects in an electrostatic multireflection ion trap. *European Journal of Mass Spectrometry*, 20:131–142.

[Guan and Marshall, 1996] Guan, S. and Marshall, A. G. (1996). Stored wave-form inverse Fourier transform (SWIFT) ion excitation in trapped-ion mass spectometry: theory and applications. *International Journal of Mass Spectrometry and Ion Processes*, 157-158:5–37.

[Hamamatsu Photonics K.K., 2013] Hamamatsu Photonics K.K., E. T. D. (2013). *MCP & MCP Assembly - Selection Guide*. Hamamatsu Photonics K.K.

[Heck and Derrick, 1997] Heck, A. J. R. and Derrick, P. J. (1997). Ultrahigh Mass Accuracy in Isotope-Selective Collision-Induced Dissociation Using Correlated Sweep Excitation and Sustained Off-Resonance Irradiation: A Fourier Transform Ion Cyclotron Resonance Mass Spectrometry Case Study on the [M + 2H]$^{2+}$ Ion of Bradykinin. *Analytical Chem*, 69:3603–3607.

[Hendricks et al., 2014] Hendricks, P. I., Dalgleish, J. K., Shelley, J. T., Kirleis, M. A., McNicholas, M. T., Li, L., Chen, T.-C., Chen, C.-H., Duncan, J. S., Boudreau, F., Noll, R. J., Denton, J. P., Roach, T. A., Ouyang, Z., and Cooks, R. G. (2014). Autonomous in Situ Analysis and Real-Time Chemical Detection Using a Backpack Miniature Mass Spectrometer: Concept, Instrumentation Development, and Performance. *Analytical Chemistry*, 86(6):2900–2908.

[Herlert et al., 2011] Herlert, A., Borgmann, C., Fink, D., Christensen, C. H., Kowalska, M., and Naimi, S. (2011). Effects of space charge on the mass purification in Penning traps. *Hyperfine Interactions*, 199:211–220.

[Hilger et al., 2013] Hilger, R. T., Santini, R. E., and McLuckey, S. A. (2013). Nondestructive Tandem Mass Spectrometry Using a Linear Quadrupole Ion Trap Coupled to a Linear Electrostatic Ion Trap. *Analytical Chemistry*, 85:5226–5232.

[Ho et al., 2003] Ho, C. S., Lam, C. W. K., Chan, M. H. M., Cheung, R. C. K., Law, L. K., Lit, L. C. W., Ng, K. F., Suen, M. W. M., and Tai, H. L. (2003). Electrospray Ionisation Mass Spectrometry: Principles and Clinical Applications. *Clinical Biochemist Reviews*, 24(1):3–12.

[Javahery and Thomson, 1997] Javahery, G. and Thomson, B. (1997). A segmented radiofrequency-only quadrupole collision cell for measurements of ion collision cross section on a triple quadrupole mass spectrometer. *Journal of the American Society for Mass Spectrometry*, 8(7):697–702.

[Jeol Ltd., 2016] Jeol Ltd. (2016). JMS-MT3010HRGA INFITOF. Scientific / Metrology Instruments: Multi-Turn Time-of-Flight Mass Spectrometer.

[Jesch, 2016] Jesch, C. (2016). *The Multiple-Reflection Time-of-Flight Isobar Separator for TITAN and Direct Mass Measurements at the FRS Ion Catcher*. PhD thesis, Justus-Liebig-Universität Gießen.

[Jesch et al., 2015] Jesch, C., Dickel, T., Plaß, W. R., Short, D., Ayet San Andres, S., Dilling, J., Geissel, H., Greiner, F., Lang, J., Leach, K. G., Lippert, W., Scheidenberger, C., and Yavor, M. I. (2015). The MR-TOF-MS isobar separator for the TITAN facility at TRIUMF. *Hyperfine Interactions*, 235(21):97–106.

[Karas et al., 2000] Karas, M., Bahr, U., and Dülcks, T. (2000). Nano-electrospray ionization mass spectrometry: addressing analytical problems beyond routine. *Fresenius' Journal of Analytical Chemistry*, 366(6):669–676.

[Kondradi and Ayet San Andrés, 2015] Kondradi, M. and Ayet San Andrés, S. (2012-2015). Generation of radiofrequency signals. Private communication.

[Lang, 2016] Lang, J. (2016). Phd thesis, submitted, Justus-Liebig-Universität Gießen.

[Lippert, 2012a] Lippert, W. (2012a). Aufbau, Inbetriebnahme und Charakterisierung eines Fallensystems für ein mobiles Multireflexions-Flugzeitmassenspektrometer. Master's thesis, Justus-Liebig-Universität Gießen.

[Lippert, 2012b] Lippert, W. (2012b). Bearbeitung aktueller Fragestellungen und technischer Entwicklungen in der subatomaren Physik. Spezialisierungsmodul.

[Lord Rayleigh F.R.S., 1882] Lord Rayleigh F.R.S. (1882). On the equilibrium of liquid conducting masses charged with electricity. *Philosophical Magazine Series 5*, 14(87):184–186.

[Lotze, 2014] Lotze, C. (2012-2014). Voltage control software for MR-TOF-MS. Private communication.

[Major and Dehmelt, 1968] Major, F. G. and Dehmelt, H. G. (1968). Exchange-Collision Technique for the rf Spectroscopy of Stored Ions. *Physical Review*, 170(1):91–107.

[Mansoori et al., 1998] Mansoori, B. A., Dyer, E. W., Lock, C. M., Bateman, K., Boyd, R. K., and Thomson, B. A. (1998). Analytical performance of a high-pressure radio frequency-only quadrupole collision cell with an axial field applied by using conical rods. *Journal of the American Society for Mass Spectrometry*, 9(8):775–788.

[March and Todd, 2005] March, R. E. and Todd, J. F. J. (2005). *Quadrupole Ion Trap Mass Spectrometry*. John Wiley & Sons, Inc.

[Mathieu, 1868] Mathieu, E. (1868). Mémoire sur Le Mouvement Vibratoire d'une Membrane de forme Elliptique. *Journal de Mathématiques Pures et Appliquées*, pages 137–203.

[Murray et al., 2013] Murray, K. K., Boyd, R. K., Eberlin, M. N., Langley, G. J., Li, L., and Naito, Y. (2013). Definitions of terms relating to mass spectrometry (IUPAC Recommendations 2013). *Pure and Applied Chemistry*, 85(7):1515–1609.

[Nelder and Mead, 1965] Nelder, J. A. and Mead, R. (1965). A Simplex Method for Function Minimization. *The Computer Journal*, 7(4):308–313.

[Otto et al., 2016] Otto, J.-H., Lippert, W., and Dickel, T. (2016). Investigation of space charge effcts using the simulation tool SIMION. Internal report.

[Panda et al., 2007] Panda, S. K., Andersson, J. T., and Schrader, W. (2007). Mass-spectrometric analysis of complex volatile and nonvolatile crude oil components: a challenge. *Analytical and Bioanalytical Chemistry*, 389:1329–1339.

[Paul and Steinwedel, 1956] Paul, W. and Steinwedel, H. (1956). Verfahren zur Trennung bzw. zum getrennten Nachweis von Ionen verschiedener spezifischer Ladung.

[Petrick, 2010] Petrick, M. (2006-2010). Fast high voltages switches. Private communication.

[Pikhtelev, 2014] Pikhtelev, A. (2010-2014). Mac software. Private communication.

[Plaß et al., 2013a] Plaß, W., Dickel, T., Ebert, J., Lang, J., Ayet, S., Geissel, H., Haettner, E., Jesch, C., Lippert, W., Petrick, M., Scheidenberger, C., and Yavor, M. (2013a). Multiple-Reflection Time-of-Flight Mass Spectrometers for the Research With Exotic Nuclei and for Analytical Mass Spectrometry. *Proceedings of the 61st ASMS Conference on Mass Spectrometry and Allied Topics*.

[Plaß, 1997] Plaß, W. R. (1997). Aufbau eines Flugzeitmassenspektrometers zur Analyse von flüchtigen organischen Verbindungen bei geringem Partialdruck. Diplomarbeit, Justus-Liebig-Universität Gießen.

[Plaß et al., 2015] Plaß, W. R., Dickel, T., Andres, S. A. S., Ebert, J., Greiner, F., Hornung, C., Jesch, C., Lang, J., Lippert, W., Majoros, T., Short, D., Geissel, H., Haettner, E., Reiter, M. P., Rink, A.-K., Scheidenberger, C., and Yavor, M. I. (2015). High-performance multiple-reflection time-of-flight mass spectrometers for research with exotic nuclei and for analytical mass spectrometry. *Physica Scripta*, 2015(T166):014069.

[Plaß et al., 2008] Plaß, W. R., Dickel, T., Czok, U., Geissel, H., Petrick, M., Reinheimer, K., Scheidenberger, C., and I.Yavor, M. (2008). Isobar separation by time-of-flight mass spectrometry for low-energy radioactive ion beam facil-

ities. *Nuclear Instruments and Methods in Physics Research Section B: Beam Interactions with Materials and Atoms*, 266(19-20):4560–4564.

[Plaß et al., 2013b] Plaß, W. R., Dickel, T., and Scheidenberger, C. (2013b). Multiple-reflection time-of-flight mass spectrometry. *International Journal of Mass Spectrometry*, 349-350:134–144.

[Reuben et al., 1996] Reuben, A. J., Smith, G. B., Moses, P., Vagov, A. V., Woods, M. D., Gordon, D. B., and Munn, R. W. (1996). Ion trajectories in exactly determined quadrupole fields. *International Journal of Mass Spectrometry and Ion Processes*, 154(1-2):43–59.

[S. Purushothaman et al., 2016] S. Purushothaman et al. (2016). Fits of Gaussian with multiple exponential tails on leading and trailing edge. Manuscript in preparation.

[Schrader, 2015] Schrader, W. (2015). An asphaltene crude oil sample. Private communication. Max-Planck-Institut für Kohleforschung.

[Schury et al., 2009] Schury, P., Okada, K., Shchepunov, S., Sonoda, T., Takamine, A., Wada, M., Wollnik, H., and Yamazaki, Y. (2009). Multi-reflection time-of-flight mass spectrograph for short-lived radioactive ions. *The European Physical Journal A*, 42(3):343–349.

[Schury et al., 2014] Schury, P., Wada, M., Ito, Y., Arai, F., Naimi, S., Sonoda, T., Wollnik, H., Shchepunov, V., Smorra, C., and Yuan, C. (2014). A high-resolution multi-reflection time-of-flight mass spectrograph for precision mass measurements at RIKEN/SLOWRI. *Nuclear Instruments and Methods in Physics Research Section B: Beam Interactions with Materials and Atoms*, 335:39–53.

[Scientific Instrument Services, Inc., 2012] Scientific Instrument Services, Inc. (2003-2012). SIMION 8.1.1.14. Software. Primary authors: David J. Manura, SIS (version 8.1/8.0/SL); David A. Dahl, INL (version 7 and below).

[Senko, 2009] Senko, M. (2009). Isopro 3.1. Software.

[Simon, 2008] Simon, A. (2008). Entwicklung und Test eines CFK-basierten RF-Quadrupols für ein Multireflektions-Flugzeitmassenspektrometer. Justus-Liebig-Universität Gießen. Bachelor's thesis.

[Snyder et al., 2016] Snyder, D. T., Pulliam, C. J., Ouyang, Z., and Cooks, R. G. (2016). Miniature and Fieldable Mass Spectrometers: Recent Advances. *Analytical Chemistry*, 88:2–29.

[Stephens, 1946] Stephens, W. E. (1946). Proceedings of the American Physical Society. *Physical Review*, 69(11-12):691.

[Stresau et al., 2006] Stresau, D., Hunter, K., Sheils, W., Raffin, P., and Benari, Y. (2006). A New Class of Robust Sub-nanosecond TOF Detectors with High Dynamic Range. *Presented at the 54th ASMS Conference on Mass Spectroscopy.* ETP Electron Multipliers.

[Takamine et al., 2007] Takamine, A., Wada, M., Nakamura, T., Okada, K., Yamazaki, Y., Kanai, Y., Kojima, T. M., Yoshida, A., Kubo, T., Noda, K., Katayama, I., Lioubimov, V., and Schuessler, H. (2007). Improvement ofslow RI beam transport using carbon-OPIG. *RIKEN Accel. Prog. Rep.*, 40.

[Taylor, 1964] Taylor, G. (1964). Disintegration of Water Drops in an Electric Field. *Proceedings of the Royal Society of London, Series A, Mathematical and Physical Sciences*, 280(1382):383–397.

[Taylor and Johnson, 1997] Taylor, J. A. and Johnson, R. S. (1997). Sequence database searches via de novo peptide sequencing by tandem mass spectrometry. *Rapid Communications in Mass Spectrometry*, 11(9):1067–1075.

[Thermo Scientific, 2016] Thermo Scientific (2016). Product Specifications Thermo Scientific TSQ Quantum Ultra/Ultra AM/Ultra EMR.

[Thomson, 1913] Thomson, J. J. (1913). Bakerian Lecture: Rays of Positive Electricity. *Proceedings of the Royal Society A*, 89(607):1–20.

[Vetere, 2016] Vetere, A. (2016). Peak identification at mass 337 u. Private communication.

[Wave Metrics, 2016] Wave Metrics (1989-2016). Igor pro. Software.

[Wells and McLuckey, 2005] Wells, J. M. and McLuckey, S. A. (2005). Collision-Induced Dissociation (CID) of Peptides and Proteins. *Methods in Enzymology*, 402:148–185.

[Whitehouse et al., 1985] Whitehouse, C. M., Dreyer, R. N., Yamashita, M., and Fenn, J. B. (1985). Electrospray interface for liquid chromatographs and mass spectrometers. *Analytical Chemistry*, 57(3):675–679.

[Wien, 1898] Wien, W. (1898). Untersuchungen über die electrische Entladung in verdünnten Gasen. *Annalen der Physik*, 301(6):440–452.

[Williams et al., 2006] Williams, J. P., Nibbering, N. M. M., Green, B. N., Patel, V. J., and Scrivens, J. H. (2006). Collision-induced fragmentation pathways including odd-electron ion formation from desorption electrospray ionisation generated protonated and deprotonated drugs derived from tandem accurate mass spectrometry. *Journal of Mass Spectrometry*, 41:1277–1286.

[Wilm and Mann, 1994] Wilm, M. S. and Mann, M. (1994). Electrospray and

taylor-cone theory, dole's beam of macromolecules at last? *International Journal of Mass Spectrometry and Ion Processes*, 136(2):167–180.

[Wiza, 1979] Wiza, J. L. (1979). Microchannel plate detectors . *Nuclear Instruments and Methods*, 162(1-3):587–601.

[Wohlfahrt, 2011] Wohlfahrt, B. (2011). Simulation of a Beam Preparation System for a mobile Multiple-Reflection Time-of-Flight Mass Spectrometer. Bachelor's thesis, Justus-Liebig-Universität Gießen.

[Wolf et al., 2011] Wolf, R. N., Eritt, M., Marx, G., and Schweikhard, L. (2011). A multi-reflection time-of-flight mass separator for isobaric purification of radioactive ion beams. *Hyperfine Interactions*, 199(1):115–122.

[Wolf et al., 2012] Wolf, R. N., Marx, G., Rosenbusch, M., and Schweikhard, L. (2012). Static-mirror ion capture and time focusing for electrostatic ion-beam traps and multi-reflection time-of-flight mass analyzers by use of an in-trap potential lift. *International Journal of Mass Spectrometry*, 313:8–14.

[Wollnik, 1987] Wollnik, H. (1987). *Optics of charged particles.* Elsevier.

[Wysocki et al., 2008] Wysocki, V. H., Joyce, K. E., Jones, C. M., and Beardsley, R. L. (2008). Surface-Induced Dissociation of Small Molecules, Peptides, and Non-covalent Protein Complexes. *Journal of the American Society of Mass Spectrometry*, 19(2):190–208.

[Yavor, 2009] Yavor, M. I. (2009). *Optic of charged particle analyzers.* Academic Press.

[Yavor, 2014a] Yavor, M. I. (2014a). Theoretical concept of the re-trapping mode. Internal report.

[Yavor, 2014b] Yavor, M. I. (2014b). Theoretical concept of the time focus shifting mode. Internal report.

[Yavor, 2016] Yavor, M. I. (2016). Private communication.

[Yavor and Lippert, 2014] Yavor, M. I. and Lippert, W. (2014). Conclusions concerning SIMION simulation of retrapping with the existing small MR-TOF analyzer. Internal report.

[Yavor et al., 2015] Yavor, M. I., Plaß, W. R., Dickel, T., Geissel, H., and Scheidenberger, C. (2015). Ion-optical design of a high-performance multiple-reflection time-of-flight mass spectrometer and isobar separator. *International Journal of Mass Spectrometry*, 381-382:1–9.

[Zajfman et al., 1997] Zajfman, D., Heber, O., Vejby-Christensen, L., Ben-

Itzhak, I., Rappaport, M., Fishman, R., and Dahan, M. (1997). Electrostatic bottle for long-time storage of fast ion beams. *Physical Review A*, 55(3):1577–1580.

[Zhurov et al., 2013] Zhurov, K. O., Fornelli, L., Wodrich, M. D., Ünige A. Laskay, and Tsybin, Y. O. (2013). Principles of electron capture and transfer dissociation mass spectrometry applied to peptide and protein structure analysis. *Chemical Society Reviews*, 42:5014–5030.

Acknowledgements

I would like to thank all people who contributed to this thesis either by scientfic or personal support. At first I want to thank Prof. Christoph Scheidenberger and Prof. Hans Geissel for giving me the opportunity to be part of the IONAS group and to work on such interesting topics and technologies.

In particular I want to thank Dr. Timo Dickel for his guidance and supervision throughout my PhD work. He supported me during my work with many scientific advice and fruitful discussions whenever possible. I am also grateful for the guidance of Dr. Wolfgang Plaß, whose ideas and discussions were always very welcome.

I want to thank Johannes Lang and Julian Bergmann, with whom I worked closest on the MR-TOF-MS for analytical mass spectrometry. Thank you for the time we spent together in the lab and for all the great bits of software you wrote.

Many thanks to Prof. Mikhail Yavor, who contributed to the progress of my thesis with plentiful ion-optics and simulation discussions.

I want to thank all the people who helped me with respect to chemistry related questions: Prof. Wolfgang Schrader, Lilla Guricza, and Alessandro Vetere. I would also like to thank Dr. Dhaka Bhandari and especially Anna Schultheis for their help.

Of course my work would not have been possible without all the other former and present members of the IONAS group: Ann-Kathrin, Christian, Christine, Emma, Florian, Ivan, Jens, Marcel, Matti, Natalia, Pascal, Ronja, Samuel, Sivaj, Sophie, Xiaodong and in particular Evelin - thank you all!

"There is nothing on this earth more to be prized than true friendship." Thanks to my best friends for all the great times we have together: Marcel Diwisch, Christian Drucker, Johannes Krombach, Sebastian Petry, Sebastian Reimann, Marian Stahl, and Robert Zeise.

I want to thank my dear family for their endless support: Uwe, Sibylle, Sara, Jennifer and Emily. I am very grateful to have you as my family.

Last, but not least, I would like to thank my girlfriend Therese. Thank you for all your support, patience and love.

Versicherung

Ich erkläre: Ich habe die vorgelegte Dissertation selbstständig und ohne unerlaubte fremde Hilfe und nur mit den Hilfen angefertigt, die ich in der Dissertation angegeben habe. Alle Textstellen, die wörtlich oder sinngemäß aus veröffentlichten Schriften entnommen sind, und alle Angaben, die auf mündlichen Auskünften beruhen, sind als solche kenntlich gemacht. Ich stimme einer evtl. Überprüfung meiner Dissertation durch eine Antiplagiat-Software zu. Bei den von mir durchgeführten und in der Dissertation erwähnten Untersuchungen habe ich die Grundsätze guter wissenschaftlicher Praxis, wie sie in der „Satzung der Justus-Liebig-Universität Gießen zur Sicherung guter wissenschaftlicher Praxis" niedergelegt sind, eingehalten.

_____   _____
Datum   Wayne Lippert